

Vibration- and Impedance-based Structural Health Monitoring Applications and Thermal Effects

Mana Afshari

Dissertation submitted to the faculty of the Virginia Polytechnic Institute and State University in partial fulfillment of the requirements for the degree of

Doctor of Philosophy
In
Mechanical Engineering

Daniel J. Inman, Chair
Mehdi Ahmadian
Mary E. Kasarda
Gary D. Seidel
Pablo A. Tarazaga

May 25, 2012
Blacksburg, VA

Keywords: Structural Health Monitoring, Vibrations, electrical Impedance, Thermal loading, Environmental factors, Crack modeling, Euler-Bernoulli beams

© 2012 by Mana Afshari

Vibrations- and Impedance-based Structural Health Monitoring Applications and Thermal Effects

Mana Afshari

ABSTRACT

Structural Health Monitoring (SHM) is the implementation of damage detection and characterization algorithms using *in vitro* sensing and actuation for rapidly determining faults in structural systems before the damage leads to catastrophic failure. SHM systems provide near real time information on the state of the integrity of civil, mechanical and aerospace structures. A roadblock in implementing SHM systems in practice is the possibility of false positives introduced by environmental changes. In particular, temperature changes can cause many SHM algorithms to indicate damage when no damage exists. While several experimentally based efforts have been attempted to alleviate temperature effects on SHM algorithms, fundamental research on the effects of temperature on SHM has not been investigated.

The work presented in this dissertation composes of two main parts: the first part focuses on the experimental studies of different mechanical structures of aluminum beams, lug samples and railroad switch bolts. The experimental study of the aluminum lug samples and beams is done to propose and examine methods and models for *in situ* interrogation and detection of damage (in the form of a fatigue crack) in these specimen and to quantify the smallest detectable crack size in aluminum structures. This is done by applying the electrical impedance-based SHM method and using piezoceramic sensors and actuators. Moreover, in order to better extract the damage features from the measured electrical impedance, the ARX non-linear feature extraction is employed. This non-linear feature extraction, compared to the linear one, results in detection of damages in the micro-level size and improves the early detection of fatigue cracks in structures. Experimental results also show that the temperature variation is an important factor in the structural health monitoring applications and its effect on the impedance-based

monitoring of the initiation and growth of fatigue cracks in the lug samples is experimentally investigated. The electrical impedance-based SHM technique is also applied in monitoring the loosening of bolted joints in a full-scale railroad switch and the sensitivity of this technique to different levels of loosening of the bolts is investigated.

The second part of the work presented here focuses on the analytical study and better understanding of the effect of temperature on the vibration-based SHM. This is done by analytical modeling of the vibratory response of an Euler-Bernoulli beam with two different support conditions of simply supported and clamped-clamped and with a single, non-breathing fatigue crack at different locations along the length of the beam. The effect of temperature variations on the vibratory response of the beam structure is modeled by considering the two effects of temperature-dependent material properties and thermal stress formations inside the structure. The inclusion of thermal effects from both of these points of view (i.e. material properties variations and generation of thermal stresses) as independent factors is investigated and justified by studying the formulations of Helmholtz free energy and stresses inside a body. The effect of temperature variations on the vibratory response of the cracked beam are then studied by integrating these two temperature-related effects into the analytical modeling. The effect of a growing fatigue crack as well as temperature variations and thermal loadings is then numerically studied on the deflection of the beam and the output voltage of a surface-bonded piezoceramic sensor.

*To my sister, Mehrzad,
and to my parents, Masoumeh (maman) and Mostafa (baba),
for their endless love*

ACKNOWLEDGMENTS

There are so many people to think of and thank for my great academic and social life during my PhD studies at Virginia Tech. First and foremost I would like to express my deepest gratitude to Professor Daniel J. Inman for being a great advisor in every aspect; for his sense of humor, patience, help and guidance throughout my PhD studies. I would like to thank my PhD committee Dr. Mehdi Ahmadian, Dr. Mary Kasarda, Dr. Gary Seidel and Dr. Pablo Tarazaga for their support and recommendations.

Special thanks are due to Ms. Beth Howell, the program manager at CIMSS for keeping everything running at CIMSS, giving helpful advice in every matter and for buying Starbucks coffee and sharing the first cup with me in the mornings!

I have been lucky to be part of CIMSS and enjoy the friendship of many of my fellow CIMSS colleagues: Dr. Benjamin Grisso, Brad Butrym, Thomas Marquié, Justin Farmer, Kahlil Detrich, Dr. Amin Karami, Dr. Onur Bilgen, Dr. Jacob Dodson, Dr. Steve Anton, Dr. Andy Sarles, Bryan Joyce, Dragan Avirovik, Joseph Najem, Preston Pinto, Dr. Jamil Reno, Mohammad Bonakdar, Cassio Fario, Daniel Inman, Dr. Andy Duncan, Dr. Alper Erturk, Dr. Armaghan Salehian, Dr. Austin Creasy, Kim Woon.

Many thanks to Dr. Evrim Dalkiran for being a great friend and roommate during my PhD studies and sharing tasty food and awesome bread with me!

I am deeply indebted to my parents. To my maman and baba for giving me this life, for raising me, for providing me with the best education and for always being there for me to help with all aspects of life. Words are not enough to thank you! I love you with all my heart!

Finally, and most importantly, very special thanks are due to my sister, Mehrzad, for believing in me and being there for me. It is a blessing to have a smart, insightful and caring sister and friend like you! I love you so much and with all my heart! Without you, this wouldn't have been possible!

This work has been partly supported by the Air Force Office of Scientific Research (AFOSR) grant number FA95550-06-1-0309, monitored by Drs. Victor Giurgiutiu and David Stargel and partly supported by the Association of American Railroads and the Railway Technology Laboratory at Virginia Tech.

CONTENTS

Abstract	ii
Dedication	iv
Acknowledgments	v
Contents	vii
List of Figures	xi
List of Tables	xvi
1. Introduction	1
1.1. Overview of the Structural Health Monitoring	1
1.1.1. The Vibration-based Method	3
1.1.2. The Electromechanical Impedance-based Method	8
1.1.3. The Guided Wave-based Method	10
1.2. Thesis Overview	11
1.2.1. Research Objectives	11
1.2.2. Chapter Summaries	12
2. Quantifying the Smallest Detectable Fatigue Crack in the Aerospace Systems ...	15
2.1. Motivations and the Specimen Configuration	16
2.1.1. The Lug Joint	17

2.2. Introduction to the Piezoelectricity	18
2.3. Introduction to the Impedance-based Structural Health Monitoring	20
2.4. Experimental Setup and Results	22
2.4.1. Quantifying the smallest detectable crack in the aluminum lug joints	23
2.4.2. Quantifying the smallest detectable crack in aluminum beam samples	25
2.4.2.a. PZT Self-Diagnosis	26
2.4.2.b. Non-linear feature extraction of frequency-domain ARX model ...	30
2.4.2.b.I. Experimental setup and results	31
2.5. The Effect of Temperature on the Impedance-based Monitoring of the Growth of Damage in Lug Samples	36
2.6. Chapter Summary	39
3. Automated Structural Health Monitoring of Bolted Joints in Railroad Switches	43
3.1. Motivations	43
3.2. Overview of the Railroad Switches and Their Components	44
3.3. Rail Track Experimental Set-up and Results	45
3.3.1. Detection of the Bolts Loosening	47
3.3.1.a. On-Nut Detection	47
3.3.1.b. PZT Sensitivity	49
3.3.1.c. Switch bolt PZT sensor self-diagnostics	49
3.4. Chapter Summary	51
4. Coefficients of Thermal Expansion and the Elastic Constants of a Body	52
4.1. Stress Tensor Formulations	52
4.1.1. The Effect of Temperature on the Material Properties	57
4.2. Fundamental Differential Equations of Thermoelasticity	59

4.2.1. Heat Conduction Happening Very Slowly (Adiabatic Process)	62
4.3. Fundamental Differential Equations of Theory of Thermal Stresses	63
4.4. Chapter Summary	63
5. The Effect of a Single Fatigue Crack on the Vibratory Characteristics of Euler-Bernoulli Beams	65
5.1. Background Review on Modeling the Effect of Crack and Temperature Variations on the Vibration Response of a Structure.....	66
5.2. Theory and Modeling	68
5.2.1. Modeling the Presence of Damage in the Form of a Crack	69
5.2.1.a. Mode shapes of a cracked beam	71
5.2.1.a.I Exact modeling.....	71
5.2.1.a.II Approximate modeling of the cracked beam using Rayleigh-Ritz method	74
5.2.2. Modeling the Effect of Temperature Variations	81
5.2.2.a. The effect of variations in the temperature-dependent material properties on the resonant frequencies of an Euler-Bernoulli beam	82
5.2.2.b. Thermal stresses inside a beam	84
5.2.3. Modeling the Two Effects of Damage Growth and Steady-State Temperature Variations in the Formulations of Mode Shapes and Resonant Frequencies of Free Vibrations of a Cracked Euler-Bernoulli Beam	85
5.2.4. Vibrations of a PZT-actuated Beam with Varying Temperature Distribution and a Growing Crack	91
5.2.4.a. The forcing vector, $R_T(t)$, for different temperature variations scenarios.....	99
5.3. Numerical Results	103

5.3.1. Numerical studies on the effect of presence of a growing crack and verification of the proposed Rayleigh-Ritz approximation of the mode shapes of the cracked Euler-Bernoulli beam	104
5.3.2. The Effect of Temperature-dependent Material Properties on the Resonant Frequencies of the Beam	116
5.3.3. The Effect of a Transient Temperature Distribution on the Vibratory Response of a Cracked Beam	121
5.4. Chapter Summary.....	128
6. Conclusions and Future Work	131
6.1. Research Summary	131
6.2. Contributions of the Research	135
6.3. Recommendations and Future Work	136
Bibliography	137
Appendices.....	144
A Design Details of the Full Scale Prototype of a Switch Track.....	144

LIST OF FIGURES

2.1	Dimensions of the Lug joint	17
2.2	Schematic of the Lug joint with the damage and piezoceramic sensor	18
2.3	Snapshots of the lug joint a) with the surface-bonded PZT, b) assembled in the MTS machine to be fatigued and c) connected to the HP 4194A Impedance Analyzer for the electrical impedance measurements	24
2.4	Schematics of the aluminum beam fatigued and tested	25
2.5	The electrical admittance versus the frequency for beams “D-1”-“D-6” at seven different loading cycles of zero (Baseline), 30k, 50k, 70k, 80k, 82.5k and 85k and the free PZT patch for the frequency range of 10-60 kHz	28
2.6	a) Damage index calculated for beam D-1 over the frequency range of 30-60 kHz and b) the electrical admittance versus the frequency for this beam at different fatigue cycles	29
2.7	Schematics of a) the aluminum beam fatigued and tested, b) the MTS machine used in fatiguing and c) the HP 4194A impedance analyzer	31
2.8	Damage index (1-CC) of the two aluminum beams, B1 and B2, in the frequency range of 50-80 kHz of the electrical impedance measurements	32
2.9	Snapshots of the fatigue cracks in a) beam B1 and b) beam B2	32
2.10	The comparison of linear and non-linear damage indices for beam T1 over the frequency range of 50-80 kHz and the input voltage of 1.0V	33
2.11	The correlation coefficient of the measured electrical-impedance for different input voltages to a fatigued aluminum beam at different fatigue cycles	34
2.12	The correlation coefficient of the measured electrical-impedance for different input voltages to an aluminum beam at different saw cuts	35

2.13	Snapshots of the a) healthy large lug joint, b) cracked large lug joint with the crack length of 0.314", and c) cracked large lug joint with the crack length of 0.684" ...	37
2.14	The environmental chamber	37
2.15	a) Healthy, b) Sample 4, c) Sample 2	38
2.16	RMSD calculated For each lug sample, baseline is the measurement at 25°C of the same lug for the frequency range of a) 12.4-12.8 kHz and b) 13.6-14 kHz	38
2.17	RMSD calculated for frequency range of 12.4-12.8 kHz, For each lug sample, baseline is the measurement at 25°C of the Healthy lug	39
3.1	A snapshot of a railroad switch	44
3.2	Snapshots of a) a switch rod and b) an insulated bolted joint	45
3.3	Snapshots of a) a lock rod and b) its clip	45
3.4	Laboratory prototype of a rail system with bolted joints	46
3.5	Insulated bolted joint in the experimental prototype with the PZT patches glued to the nuts	46
3.6	PZT patches attached to the switch rod surface	46
3.7	a) Impedance signatures of the loosened and retightened bolt A and b) their RMSD Damage metric	47
3.8	a) Impedance signature for different torque levels and b) their RMSD Damage metric	48
3.9	Damage metric investigating the PZT Sensitivity	49
3.10	Snapshots of a) free PZT, b) partly bonded PZT patch, and c) a broken PZT patch	50
3.11	PZT susceptance-frequency line for different integrity conditions of the PZT patch	50
4.1	Variations of the Young's modulus of aluminum with respect to temperature	58
5.1	Beam a) with a single fatigue crack, b) with a single fatigue crack treated as a massless rotational spring	69
5.2	Beam with a single crack under pure bending	69

5.3	Force and moment diagram of the cross section of a beam	86
5.4	Beam with a single fatigue crack under PZT actuation	91
5.5	Schematic and dimensions of the cracked beam used in the numerical studies ...	104
5.6	a), b) Mode shapes, c), d) slope, of a simply supported beam on both edges for the first mode of vibrations with a growing crack at mid-span	105
5.7	a), b) Mode shapes, c), d) slope, of a simply supported beam on both edges for the first mode of vibrations with a growing crack at $0.3L$	105
5.8	a), b) Mode shapes, c), d) slope, of a simply supported beam on both edges for the second mode of vibrations with a growing crack at $0.3L$	106
5.9	a), b) Mode shapes, c), d) slope, of a simply supported beam on both edges for the third mode of vibrations with a growing crack at mid-span	106
5.10	a), b) Mode shapes, c), d) slope, of a simply supported beam on both edges for the third mode of vibrations with a growing crack at $0.2L$	107
5.11	a), b) Mode shapes, c), d) slope, of a simply supported beam on both edges for the fourth mode of vibrations with a growing crack at $0.4L$	107
5.12	a), b) Mode shapes, c), d) slope, of a clamped beam on both edges for the first mode of vibrations with a growing crack at mid-span	108
5.13	a), b) Mode shapes, c), d) slope, of a clamped beam on both edges for the second mode of vibrations with a growing crack at $0.2L$	108
5.14	a), b) Mode shapes, c), d) slope, of a clamped beam on both edges for the third mode of vibrations with a growing crack at mid-span	109
5.15	a), b) Mode shapes, c), d) slope, of a clamped beam on both edges for the fourth mode of vibrations with a growing crack at $0.4L$	109
5.16	Resonant frequency of the 1 st mode of the beam vs crack position along the beam for a) simply supported and b) fixed-fixed boundary conditions. <i>Round dots</i> line and <i>dash</i> line represent reference and proposed modeling for $a_c/h_b = 0.2$, respectively. <i>Solid</i> line and <i>solid-square</i> line represent reference and proposed modeling for $a_c/h_b = 0.4$, respectively	111
5.17	Resonant frequency of the 2 nd mode of the beam vs crack position along the beam for a) simply supported and b) fixed-fixed boundary conditions. <i>Round dots</i> line and <i>dash</i> line represent reference and proposed modeling for $a_c/h_b = 0.2$,	

	respectively. <i>Solid</i> line and <i>solid-square</i> line represent reference and proposed modeling for $a_c/h_b = 0.4$, respectively	112
5.18	Resonant frequency of the 3 rd mode of the beam vs crack position along the beam for a) simply supported and b) fixed-fixed boundary conditions. <i>Round dots</i> line and <i>dash</i> line represent reference and proposed modeling for $a_c/h_b = 0.2$, respectively. <i>Solid</i> line and <i>solid-square</i> line represent reference and proposed modeling for $a_c/h_b = 0.4$, respectively	113
5.19	Schematic of the cracked beam under steady-state temperature distributions	116
5.20	Change in the resonant frequency of the first mode of vibrations of a simply supported beam for different crack depth ratios and positions and for different temperature set points	117
5.21	Change in the resonant frequency of the second mode of vibrations of a simply supported beam for different crack depth ratios and positions and for different temperature set points	117
5.22	Change in the resonant frequency of the first mode of vibrations of a clamped-clamped beam for different crack depth ratios and positions and for different temperature set points	118
5.23	Change in the resonant frequency of the second mode of vibrations of a clamped-clamped beam for different crack depth ratios and positions and for different temperature set points	118
5.24	Schematic of the cracked beam with the surface-bonded PZT layer	122
5.25	The error percentage for a growing crack at different locations along the beam .	124
5.26	The error percentage for a crack at different locations and with different depth ratios	124
5.27	Displacement to thermal moment ratio of the simply supported beam of Figure 5.5 with the growing crack at the mid-span, for different crack depth ratios	125
5.28	Displacement to thermal moment ratio of the simply supported beam with a crack with 0.6 depth ratio at different locations along the length of the beam	126
5.29	Voltage output of the PZT sensor for the simply supported beam under thermal loading with a growing crack at mid-span	127

5.30 Displacement to thermal moment ratio of the simply supported beam with a crack at mid-span of the beam and for two different temperature set points and crack depth ratios128

LIST OF TABLES

2.1	Material properties of the PZT circular patches used in the experiments	23
3.1	Loosening torque levels.....	48
4.1	Change in the material properties of aluminum with respect to temperature variations	58
5.1	Shift in the first natural frequency of an aluminum beam due to the temperature-varying modulus of elasticity for different boundary conditions	83
5.2	Shift in the first natural frequency of an aluminum beam of length, width and thickness of 12", 1" and 0.125", respectively.....	83
5.3	Error percentage of the resonance frequencies of the beam applying the proposed modeling compared to those of the reference modeling for the first three modes, different crack depth ratios and for simply supported (S) and fixed-fixed (F) support conditions	114
5.4	The amount of frequency drop for a the first mode of a cracked beam at 40°C compared to the reference point of 20°C and for two support conditions	120
5.5	The amount of frequency drop for a the first mode of a cracked beam at 60°C compared to the reference point of 20°C and for two support conditions	120
5.6	The amount of frequency drop for a the second mode of a cracked beam at 40°C compared to the reference point of 20°C and for two support conditions	121
5.7	The amount of frequency drop for a the second mode of a cracked beam at 60°C compared to the reference point of 20°C and for two support conditions	121
5.8	Material properties of the PSI-5A4E PZT.....	123

CHAPTER 1

INTRODUCTION

This chapter presents a review of the available literature related to the research projects presented in this manuscript. First, a general overview of the Structural Health Monitoring (SHM) is presented along with an overview of three of the most commonly studied SHM methodologies. The damage detection using the vibration-based SHM is then reviewed in more detail. Different types of vibration-based damage detection approaches are discussed and different types of damage modeling in structures and in particular in beams and plates are explained. Finally, an overview of the research endeavors of modeling the thermal effects on the vibratory behavior of mechanical structures is discussed. With an introduction on the review of the work done in research communities to date, the objectives of the current dissertation along with a summary of the chapter contents are given at the end of this chapter.

1.1. Overview of the Structural Health Monitoring

Structural health monitoring has emerged as a potential high impact technology for reducing risk and costs in the monitoring of civil infrastructure and aerospace systems. The importance of this technology has been highlighted by recent failures including the Potters Bar train derailment in the UK and the I-35 bridge collapse in the US. Both represent failures that could have been detected well in advance by SHM technology. As a result, SHM research has reached a furious pace spawning a new journal, several conferences and lots of interest from both the aerospace industry and owners of civil structures.

Structural health monitoring and non-destructive evaluation (NDE) share a common basis and most of the NDE damage detection techniques are used in the SHM. One of the main factors that makes SHM more practical and different from the NDE is the integration of sensors and actuators (smart materials) into the structure being monitored. Therefore, monitoring the performance of a structure becomes the continuous sensing and inspection of a specific property of the structure, e.g. temperature, strain, acoustic waves or vibration modes. Two of the most attractive sensors in the SHM are the fiber optic sensors (FOS) and the piezoelectric ones [21]. FOS or phase sensors are mainly attractive due to their small size, light weight, passive configurations, low power usage and high sensitivity [113]. They are also capable of monitoring the desired structural parameter without having any physical contact. This makes the FOS an appropriate candidate for the aircraft SHM in high temperature media. However, a large number of components such as laser source and phase modulators accompanying fibers, make the fiber optic approach of sensing complex and expensive [105]. Piezoelectric sensors function according to the converse piezoelectric effect, i.e. the generation of mechanical strain (deformation) due to an applied electrical voltage to these sensors. Piezoelectric materials are widely used in SHM applications. They are mainly favorable in the impedance-based and the wave propagation-based SHM practices, as explained later, due to the fact that they are capable of having the role of the sensor and the actuator at the same time. They may also be individually attached to the surface of the structure at any desired location [21]. Other advantageous specifications of piezoelectric sensors may be listed as high sensitivity, stability over a wide range of temperature, simple design and low cost. These sensors have been successfully applied to the health monitoring and crack detection in the fuselage of large aircrafts [105].

Different SHM techniques are used in practice for the continuous monitoring of the integrity and performance of structures. An overview of three of the most commonly studied SHM methodologies is given in the following, with the emphasis on the vibration-based method which will be applied in the modeling and analysis presented in the rest of this thesis.

1.1.1. The Vibration-based Method

The effect of presence of a defect, in the form of a crack, on the dynamic and vibratory response of a structure was studied in 1950s. In most of these modeling attempts, presence of a crack was simulated as a change in the local flexibility of the structure. The local flexibility was quantified using the stress intensity factor of the crack found experimentally [55; 22]. This modeling approach of cracks was later used in approximating the local rotational and translational compliance of the beam and the plate structures [92; 103].

While modeling the effect of cracks and defects on the dynamic characteristics of mechanical structures goes back to 1950s, the need and interest in the practical monitoring of the presence and extent of cracks in structures dates back to early 1970s. This was mainly due to the fact that the presence of low-cycle fatigue cracks in turbomachinery was considered to be one of the major causes of failure in these aging machines. Moreover, the available damage identification techniques were not efficient or practical and the failure of these machines would come at a high cost [38; 39; 96; 40; 41]. The interest in detecting cracks in rotors and shafts gained a fast pace the 1980s and 1990s and attracted a lot of attention from both industry and researchers [42; 109; 24; 25].

The application of vibration-based damage diagnosis for mechanical and civil structures, in general, attracted industry and research communities in the following years. This was mainly due to the increase in the number of aging aircrafts and civil infrastructures and some catastrophic accidents originating from the growth of fatigue cracks. Fatigue crack initiation and growth is one of the major causes of failure in aircrafts and if detected at an early stage, it can prevent the failure of parts and prevent accidents such as the rupture of the top half of the skin of 1988 Aloha Airlines airplane.

Damage in a structure can generally be classified as the linear or non-linear type. The presence of a linear damage does not affect the nature of the linear elastic structure. A non-linear damage such as an opening and closing crack, however, introduces non-linearities to the initially linear elastic structure [41]. The studies available in literature have mainly looked at the linear type of damage and its effects on the structural behavior.

There exist different vibration-based damage detection approaches in literature, depending on the availability of sensors, frequency of data collection and type of data acquisition. One of the most common damage detection methods is based on monitoring and studying changes in structural modal parameters, such as resonant frequencies, mode shapes and modal damping. Some of the early works in looking at the frequency changes show that the state of damage in a structure may be identified by the reduction in the structure's resonant frequency as the damage grows [5; 23]. A thorough summary of the vibration-based damage detection which considers the frequency drop as a damage indication is provided by Salawu [95].

The focus of the present thesis is to study the effect of damage in the form of a crack on the natural frequency changes of the structure. Beam and plate elements are two of the most common building blocks of complex structures, therefore, they have been chosen as the main structures in the analytical modeling studied in the present thesis. Beams are one of the basic mechanical structures intensively studied in the area of damage detection. One of the first papers on the analytical modeling of the effect of a crack presence on the vibration-based response of a beam used the Rayleigh-Ritz approximation by modifying the stress distribution in the Euler-Bernoulli beam [31]. In this modeling, the stress field near a pair of symmetric cracks was assumed to be maximum at the place of the crack and decay experimentally with distance from the crack. The function of stress distribution in the vicinity of the crack includes a parameter that is found experimentally. Presence and growth of a crack in a vibrating beam was also modeled as the resultant reduction in the stiffness of the beam at the place of the crack. Freund *et al* (1976) formulated this resultant stiffness by applying fracture mechanics formulations, stress intensity factor and the elastic deformation energy [48]. This form of modeling the crack in a beam was later combined with various beam formulations in order to analytically study the vibration-based response and mode shapes of a cracked beam. Chondroset *al* used the resultant stiffness crack modeling and applied the Hu-Washizu-Barr variational formulations in formulating the vibration-based response of a beam with a single-edge crack [29; 30]. Ostachowicz *et al* (1991) applied the resultant crack stiffness formulation and modeled the crack as a massless rotational spring [78]. They were among the first to model the cracked beam as a bi-section, connected at the

crack location with a torsional spring. Compatibility conditions applied at the crack location were used to formulate the mode shapes of the cracked beam. Their studies were limited to the numerical analysis of a cantilever beam with multiple, single-edged cracks. The concept of the crack modeling as a massless rotational spring connecting the two sections of the beam was later used in different references for various support conditions, number of cracks and loading of the beam. These studies were initially done numerically for Euler-Bernoulli and Timoshenko beams with single or multiple cracks. Later, closed-form expressions of the mode shapes and resonant frequencies of vibrating cracked beams were formulated for different boundary conditions and crack specifications [59; 45; 68; 10]. This form of modeling of the vibrations and mode shapes of a cracked beam has also been applied to the identification (i.e. determining the location and size) of a crack in a vibrating beam. Closed-form expressions of the location and severity of the crack were provided for different support conditions of the beam [75; 51; 37]. The early works on the vibration-based response of a cracked beam assume a non-breathing crack in order to avoid non-linear terms and complexity added to the modeling of the structure. In recent years, however, more work has been focused on the effect of the opening and closing of the crack on the vibration response of a cracked beam [28; 91]. Rayleigh-Ritz approximations have also been applied in modeling the vibratory behavior of cracked Euler-Bernoulli beams under torsion [33; 34].

In a similar way, presence of the cracks has been analytically modeled in plate structures, which are the building blocks of modeling and approximating other complex structures. The effect of a surface crack (which is only partly through the thickness of the plate) parallel to one of the edges of the plate has been analytically studied in many references by including the local compliance coefficients of the crack into the equation of vibration of thin plates [57; 58; 66]. The local compliance of the plate at the place of the surface crack has been approximated by that of an edge-cracked strip in plane-strain, which reduces the three dimensional problem of modeling the cracked plate to a two dimensional problem. In this modeling the crack is approximated by the extra rotation and axial displacement it introduced to the plate at the location of the crack. This approximation would be exact if the length of the surface crack is infinite (for an infinite plate) and the crack depth is constant along the line of crack discontinuity [92]. This way

of approximating the discontinuity line of surface crack is known as the line spring model (LSM) and have been studied in many other works, for linear and non-linear surface cracks [36; 110; 115; 32; 70].

Another type of the crack that has been more commonly studied in literature is an all-through the thickness and only partly along the width of the plate (a slit). While the presence of a surface crack introduces additional rotation to the plate, a slit introduces a line of free boundary conditions along the line of crack discontinuity. One of the early works in modeling this type of crack in thin plates studied the presence of a slit parallel to one of the edges of the plate located along one of the symmetry lines of a plate that is simply supported on all four edges [100]. In order to provide an accurate modeling of the presence of the crack, this work defines certain crack-related singularity functions. The boundary conditions of the plate at the line of the crack discontinuity are divided into two subsets, depending on the symmetric or anti-symmetric modes at the line of the crack. By assuming the Voigt solution for the simply supported plate, the resonant frequencies of the free vibrations of the cracked plate are found by solving a homogeneous Fredholm integral equation of the second kind. Due to the complexity of the kernel, the integral is treated numerically and the search for finding the frequency is done by trial and error. The frequencies of the un-cracked plate and that of the completely cracked plate (resulting in two plates simply supported on all edges except for the edge of crack line with free boundary conditions) are considered as the lower and upper bounds in the process of frequency estimation. Applying this method is used in modeling the presence of a side-slit (a slit that originates from one of the edges of the plate) in a plate with the aspect ratio of 2 and for an internal slit along one of the symmetry lines of a plate with the aspect ratio of unity.

Presence of a slit in a thin plate, parallel to one of the edges of the plate, has been mostly studied in literature by applying the Rayleigh-Ritz approximation to the sectioned cracked plate, where the cracked plate is divided into certain number of sub-plates. In one of these modeling approaches, it is assumed that these sub-plates are all connected on their edges through a line of rotational and a line of translational springs. The stiffness of these springs are then adjusted at the edge where the crack exists, for symmetric and anti-symmetric modes, as well at the edges for the un-cracked neighboring plates [114].

Another form of Rayleigh-Ritz approximation available in literature for the free vibrations of a plate with a crack in the form of a slit is to divide the cracked plate into sub-plates and reduce the order of unknown Ritz coefficients by applying the compatibility conditions at the line of crack discontinuity as well as the neighboring edges of the intact sub-plates. The early works applying this approximation use the hierarchical polynomials as the admissible functions [13], while the more recent studies use the hierarchical trigonometric functions introduced by Beslinet.al. [17], as they are shown to be more accurate for the higher order modes of vibration [14; 61].

Despite the detailed analytical modeling considered in these works, the literature lacks experimental studies to support the analytical and numerical results. One of the few experimental studies of the effect of presence of a crack on the frequency changes of a structure looks at a slit (side or internal) present in a thin plate [73]. The plate considered in this study is clamped on all four edges and have different aspect ratios and crack lengths. The experimental results presented, however, do not follow any special trend and more experimental investigations of the effect of presence of the cracks in plate structures are necessary.

Thermoelastic vibrations of beams and plates are known, well studied problems in studying the vibratory characteristics of these structures [20; 56; 54; 27; 72]. Detailed analytical studies are available studying this effect for various boundary conditions and different plate shapes and for linear and non-linear vibrations. These studies look at the coupling between temperature and strain fields. Temperature influence on material properties of these structures, however, has been ignored in modeling temperature-induced variations of dynamic responses. One of the only works studying the variations in vibratory response of a system due to temperature-induced change of material properties of the structure shows, through sensitivity analysis, that the natural frequencies of a vibrating plate are most dominantly affected by temperature-induced variations in material's Young's modulus [112; 111]. However, through comparison between analytical and experimental results, it is shown that the effect of material properties variation only accounts for part of natural frequency shift when boundaries of a structure are completely restrained. It is similarly shown that temperature-induced shift in natural frequency becomes larger in beams as the structure becomes more constrained [7]. Thus

boundary conditions are another important factor in modeling and considerations of thermal effects on dynamic characteristics of different material structures. It is important to note that research considering both effects of temperature-induced material properties and thermoelastic coupling has not yet been addressed in the open literature.

Despite the fact that both problems of thermoelastic vibrations and vibration-based crack detection are analytically well studied in literature, analytical consideration of temperature variation effects on the accuracy of monitoring the presence and growth of a crack have been left out in these studies, except for experimental work, especially on civil structures. There is an extensive study of thermal effects on the health monitoring of civil infrastructures available in literature, which shows the importance of considering thermal effects on the real life, *in situ* applications of health monitoring methods. Due to the complexity of civil structures, effect of temperature on the health monitoring have been experimentally studied and analyzed and finite element models have been constructed [99; 43; 84; 12]. Different detection algorithms have been proposed in these references in order to better extract damage and temperature related effects on vibratory characteristics of structures from data experimentally collected. The results from these studies are applied to a special structure under investigation and the large amount of data collected is usually gathered during a long-term monitoring of the structure.

1.1.2. The Electromechanical Impedance-based Method

The presence of damage, in the form of a crack, is considered as a local change in the properties and characteristics of a structure. Therefore, high-frequency excitation and the study of higher-frequency modes of the structure are necessary to detect, localize and quantify the extent of damage. The higher-frequency excitations might cause difficulty or limitations in the practical applications of the conventional vibration-based damage identification because of low energy in these modes and the high modal density. The electrical impedance method, however, is based on the high frequency excitations of the structure and is practical in both global and local damage detection, depending on the applied excitation frequency range.

Impedance-based structural health monitoring (SHM) is possible through monitoring changes in the measured, high-frequency electrical impedance of small, self-

sensing piezoceramic (PZT) patches [69]. This method works through the coupling between the electrical admittance (inverse of the electrical impedance) of the PZT patches bonded to or embedded within the host structure and the mechanical impedances of the PZT and the structure itself. This technique is not based on any structural model, making it applicable to any complex structure [62]. Impedance methods can be applied as an on-line SHM system and due to the low required excitation forces it can be run by self-powered systems [63]. It's been shown that the real part of the measured complex impedance is more sensitive to damage features within the structure while the imaginary part is more sensitive to temperature variations [82]. The measured impedance of the PZT patches provides useful data regarding the health of the host structure. However, this data in its unprocessed, original state does not provide quantifiable information regarding the presence and the state of the damage within the structure. Therefore, by processing the measured signal, an index needs to be defined which is sensitive to the damage and insensitive to the other parameters. Different statistical methods are widely used in the impedance-based SHM in order to form damage indices, some examples are the root mean square deviation (RMSD), covariance (Cov), correlation coefficient (CC) and the mean absolute percentage deviation (MAPD) [104].

The impedance-based structural health monitoring method is based on the assumption that in the electromechanical coupling between the host structure and the piezoelectric wafer, all of the parameters except the mechanical impedance of the structure remain unchanged during the formation of damage in the structure. One of the factors that can cause such a change is the variation in the environmental parameters such as temperature. The material properties of the PZT as well as the Young's modulus of the host structure are known to be temperature-dependent. Therefore if the ambient temperature is varied, the impedance-based SHM shows variations in the integrity of the host structure when there exist none (called false positives). There have been efforts performed to compensate for the effect of temperature in the impedance-based structural health monitoring applications [81; 79; 60].

1.1.3. The Guided Wave-based Method

One of the most commonly applied NDT techniques is based on the use of ultrasonic waves for the detection of flaws. This method was first suggested for defect detection in metals in 1929 [19]. In these types of NDT setups, ultrasonic waves are generated in a transducer and emitted through the monitored structure. The generated wave will then reflect back to the transducer from the interface and from any defects in the structure. This signal is converted to the electrical signals in the transducer and then analyzed. Therefore, for these acousto-ultrasonic systems, piezoceramics are favorable transducers as they are capable of having the role of a sensor and an actuator at the same time and can operate at frequencies high enough to initiate structural waves. The type of wave used in the guided wave-based SHM is the elastic Lamb wave. This type of elastic wave can propagate in a solid plate or shell with free surfaces. The properties of Lamb waves make them ideal for SHM application as they are capable of traveling long distances inside the structure and cover a large area between the actuator and the sensor, and their propagation profile is sensitive to the anomalies inside the structure. Several excellent reviews of guided wave structural health monitoring are available in literature [49; 86].

A rule of thumb in ultrasonic scanning techniques is that these methods are capable of detecting damage and discontinuities of size larger than one-half of the wavelength of the applied ultrasonic wave [65]. However, the sensitivity of guided waves in ultrasonic methods, such as Lamb waves, doesn't follow simple rules and more complicated factors come in to play when relating the wavelength to the damage size. It has been reported in various work that damage sizes much smaller than the wavelength of the applied guided waves may also be detected [65]. In monitoring the damage with the Lamb wave propagating in a structure, the information received at the sensor needs to be analyzed and the flaw specifications need to be extracted from the raw data. There exist different methods of quantifying damage in structures, two of which being the calculation of damage-index [52] and the time-reversal method [47; 108; 53].

Similar to the other structural health monitoring methods, the guided wave-base SHM is affected by variations in the environmental factors such as temperature fluctuations. Variations in temperature inside the structure change the structural material

properties and that, in turn, affects the energy of the traveling wave inside the structure. This issue of the effect of varying temperature on the guided wave-base SHM has been addressed in literature [64; 97; 71; 87]. In most of these studies the parameters that are considered to be affected by different ranges of temperature variations are the time-of-flight of the wave and the performance of the piezoelectric sensors and actuators.

1.2. Thesis Overview

Structural Health Monitoring (SHM) is the implementation of damage detection and characterization algorithms using *in vitro* sensing and actuation for rapidly determining faults in structural systems before the damage leads to catastrophic failure. SHM systems provide near real time information on the state of the integrity of civil, mechanical and aerospace structures. A roadblock in implementing SHM systems in practice is the possibility of false positives introduced by environmental changes, such as temperature variations, often misinterpreted as damage. The effect of temperature on SHM is not currently understood from first principles, and the present study will provide the fundamental mechanics modeling of temperature effects on SHM methodologies that search for cracks in the structural systems found in civil infrastructure, mechanical and aerospace systems in order to remove this roadblock to implementation.

1.2.1. Research Objectives

The principle objective of the present study is to understand and model how thermal loadings and changes in ambient temperature influence the electrical impedance- and vibration-based SHM procedures used for detecting cracks in structures. To achieve these end goals, the effect of presence and growth of damage (in the form of a single fatigue crack) needs to be studied and fully understood for these SHM methods. This will be accomplished by building an analytical model representing the presence of the crack in the beam structures and how this presence affects dynamic behavior of the beam. Different parameters such as crack approximation and depth and position of the crack along the beam need to be considered as modeling parameters. Support conditions of the

beam also affect the severity of the influence of the crack and need to be included as a parameter in the modeling.

Temperature variations also affect the dynamic behavior of a structure and therefore the outcome of a SHM monitoring algorithm. The effect of temperature has been mostly considered through the resultant thermal loading. However, the material properties of the structure also vary with temperature and as a result alter the dynamic response of the structure. In order to fully understand how temperature influences the dynamic behavior of a structure, the two effects of thermal stresses (originating from thermal expansion) and the temperature-dependent material properties need to be studied by applying the concept of continuum mechanics. This is particularly crucial in verifying the legitimacy of considering the two thermal effects as being uncoupled. The effect of temperature variations will, therefore, be investigated by representing a modeling of the mechanics of temperature effects on basic beam structures, considering both effects of thermal stress formation and variations in material properties of the beam. The next step would be forming an accurate modeling of the cracked beam structure under thermal fluctuations by integrating the two above-mentioned models.

This research will result in the discovery and understanding of the temperature effects on SHM methodologies and add a scientific basis to predicting false positives in applications. The effect of temperature on SHM is not currently understood from first principles, and the proposed work will provide the required theoretical basis for others to use in applications.

1.2.2. Chapter Summaries

The present dissertation is organized in the following manner. Chapter 1 provides the background study and literature review of the SHM methodologies and an overview of the research endeavors of modeling the thermal effects in these SHM techniques.

The analytical and experimental studies on quantifying the smallest detectable crack size in aluminum structures are presented in Chapter 2. The main focus of the MURI team at Virginia Tech was to propose and examine methods and models for *in situ* interrogation and detection of damage in the specimen. This was done by applying the impedance-based SHM method and using piezoceramic sensors and actuators to Lug

specimen and beam samples. A brief overview of piezoelectricity and the electrical impedance-based structural health monitoring are then given in this chapter. The impedance-based SHM method is applied to the detection of fatigue cracks and quantifying the smallest detectable crack size in the Lug samples and aluminum beams. The experimental setup and results are given for these specimens and the non-linear damage feature extraction is applied for the better detection of fatigue cracks in the micro-level size. Temperature is also shown to be an important factor in the structural health monitoring applications and its effect on the impedance-based monitoring of the initiation and growth of fatigue cracks in the Lug samples is experimentally investigated and the results are given in the last part of this chapter.

In Chapter 3, an effective health monitoring method is described which eliminates the need for frequent visual inspection of railway switches by totally automating inspection of the switches' mechanical condition. This chapter focuses on the use of smart materials and structures and the electrical impedance-based method for the health monitoring of bolted joints in railroad switches.

One of the main objectives of the current dissertation, as mentioned earlier, is to analytically model the effect of temperature variations on the vibratory response of beam and plate structures. This is done by modifying the stress formulations inside the structure to include the effect of thermal loading and temperature fluctuations. Other than the thermal stress formulations, the effect of temperature variations on the material properties of the structure is considered as another parameter to be included in the modeling. In order to justify the inclusion of thermal effects from both points of view (i.e. material properties variations and generation of thermal stresses) and to verify that these two effects do not overlap, derivation and assumptions behind thermal stress formulations are investigated in the Chapter 4. First, the formulations of stresses inside a body are derived and the relevant assumptions are explained. A review of *thermoelasticity* and *theory of thermal stresses* along with the fundamental relations, equations and assumptions are then provided.

The vibratory response of an Euler-Bernoulli beam with two different support conditions of simply supported (on both ends) and clamped (on both ends) is studied in Chapter 5. The beam is assumed to have a single, non-breathing crack on one side and is

assumed to be under thermal loading and temperature variations. In the first part of the modeling, free vibrations of the cracked beam without considering the effect of temperature fluctuations is studied and the mode shapes of the cracked beam are formulated using two different approaches. The effect of temperature variations on the mode shapes of free vibrations of the cracked beam are then studied considering two effects of temperature-dependent material properties and induced thermal stresses inside the beam. Temperature distribution inside the beam is assumed to be steady state initially. In the last part of the modeling, the cracked beam is considered to have a surface-bonded layer of piezoelectric (PZT) sensor and the effect of the general case of temperature distributions inside the beam is studied along with the effect of damage growth.

A summary of the results of the research performed in this dissertation is presented in Chapter 6, the final chapter, and the major contributions of this work to the research community are described. Recommendations for future work are also presented in which the advances made by the work in this dissertation can be extended in the future.

CHAPTER 2

QUANTIFYING THE SMALLEST DETECTABLE FATIGUE CRACK IN THE AEROSPACE SYSTEMS

The work presented in this chapter is the analytical and experimental studies as part of the Structural Health Monitoring (SHM) Multidisciplinary University Research Initiative (MURI) project on quantifying the smallest detectable crack size in aluminum structures. The SHM MURI project was established in 2006 and funded by the Air Force Office of Scientific Research (AFOSR). An overview of the SHM MURI project and the specimen (Lug sample) used in the experimental studies are first given. The main focus of the MURI team at Virginia Tech was to propose and examine methods and models for *in situ* interrogation and detection of damage in the specimen. This was done by applying the impedance-based SHM method and using piezoceramic sensors and actuators. A brief overview of piezoelectricity and the electrical impedance-based structural health monitoring are then given in this chapter. The impedance-based SHM method is applied to the detection of fatigue cracks and quantifying the smallest detectable crack size in the Lug samples and aluminum beams. The experimental setup and results are given for these specimens and the non-linear damage feature extraction is applied for the better detection of fatigue cracks in the micro-level size. Temperature is also shown to be an important factor in the structural health monitoring applications and its effect on the impedance-based monitoring of the initiation and growth of fatigue cracks in the Lug samples is experimentally investigated and the results are given in the last part of this chapter.

2.1. Motivations and the Specimen Configuration

The work presented in this chapter is part of the SHM MURI project established in 2006 and funded by the Air Force Office of Scientific Research (AFOSR). The schools collaborating in this project were the Arizona State University, Virginia Polytechnic Institute and State University, the University of Southern California and John Hopkins University. The ultimate goal of this project was to improve the life cycle estimate of the aircraft systems. This goal was proposed to be achieved through “integration of material characterization (including high temperature), computational modeling, sensor instrumentation, information management, damage detection and benchmark laboratory experiments” [1].

The main focus of the MURI team at the Center for Intelligent Materials Systems and Structures (CIMSS) at Virginia Tech was to propose and examine methods and models for *in situ* interrogation and detection of damage in the lug joints. The overall objective was to develop integrated sensor systems capable of sensing structural damage across multiple length scales “*in situ*” by clarifying sensing scales of current sensor systems (piezoelectric based, fiber optic based, strain gauge based, etc.) and connecting these scales to the modeling efforts at ASU and the NDE efforts at JHU. This goal was achieved by using piezoceramic sensors and actuators and applying the impedance-based SHM method to the detection of cracks in the early stage of nucleation in the lug specimen as well as other aluminum samples. As explained later, this SHM method is based on the electromechanical coupling between the host structure and the piezoceramic transducers. It is also assumed that all of the parameters except the mechanical impedance of the structure remain unchanged during the formation of damage in the structure. However, if the environmental parameters such as temperature vary, temperature dependent material properties of the transducers and the host structure change. This could be a source of errors in the detection of cracks in the lug joints and, therefore, the effect of temperature variations is also considered in the following crack detection studies.

2.1.1. The Lug Joint

The sample used in the experimental studies presented here was a Lug joint and is shown in Figure 2.1 and Figure 2.2. Lug joints are connector type elements used as structural supports for pin connections. The complex geometries of these joints cause multiple stress concentration points and therefore cause these joints to be structural hotspots in various aerospace systems.

The lug sample used in the experimental analysis was made from 0.25" thick Al 2024-T351 alloy plate and had a sand blasted surface finish. The dimensions of the sample are shown in Figure 2.1. Snapshots of this aluminum specimen are also shown in Figure 2.2.

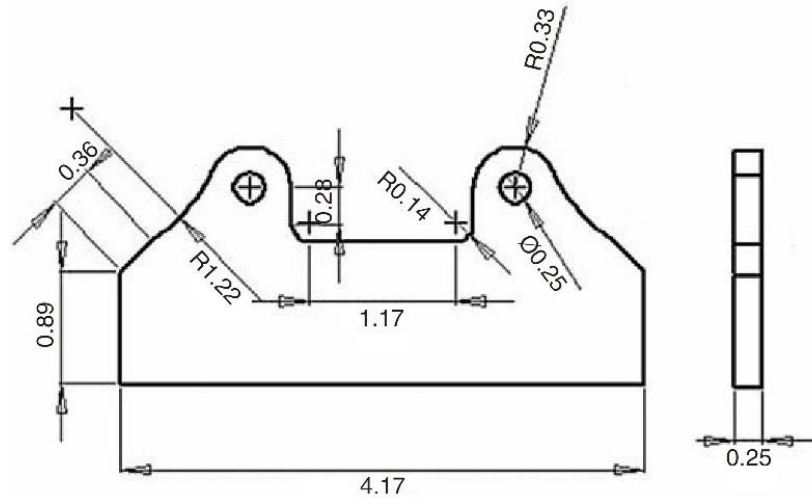


Figure 2.1. Dimensions of the Lug joint

It was observed that the lug joints, when subjected to fatigue loading with constant amplitude of 110–1100 lbs, failed at the shoulders as shown in Figure 2.2a and Figure 2.2b.

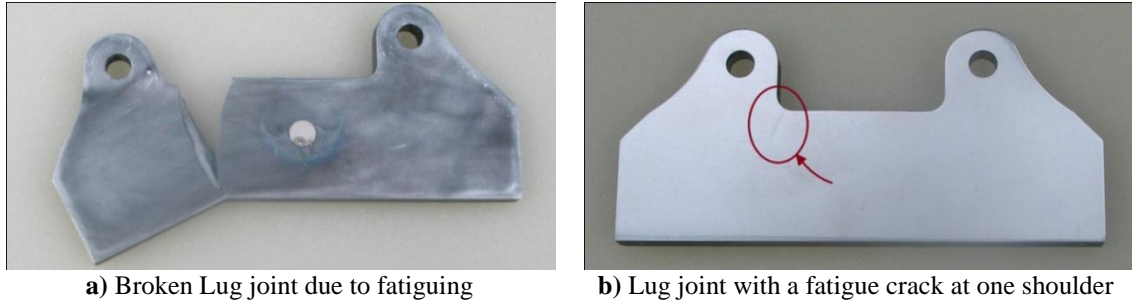


Figure 2.2. Schematic of the Lug joint with the damage and piezoceramic sensor

The impedance-based SHM method was applied in the experimental analysis for quantifying the smallest detectable fatigue crack in the lug joints. In this SHM method the vibratory response of the structure (the lug joint) measured by piezoceramic sensors are continuously compared to that of a damage-free reference state. It is shown, as explained in section 2.3, that the measured electrical impedance of the surface-bonded piezoceramic sensors is coupled to the mechanical impedance of the structure. By extracting the damage index from the measured electrical impedance, presence and extent of damage may be qualified.

2.2. Introduction to Piezoelectricity

The piezoelectricity effect was discovered in the late nineteenth century by Curie brothers when they found that some materials produce an electric output when undergoing mechanical strain. The generation of charges in these materials due to an applied mechanical deformation is called the direct piezoelectric effect. One year after the discovery of direct piezoelectric effect, the converse effect was mathematically deduced by Gabriel Lippmann. The converse (opposite) effect was then experimentally verified by Curie brothers.

The electromechanical coupling of the initially discovered piezoelectric materials (natural crystals including quartz and Rochelle salt) were weak and hence not practical. In mid-twentieth century, piezoelectric materials became more practical due to the generation of synthetic piezoelectric materials with enhanced coupling properties. The existence of piezoelectric effect in a material is related to the presence of electric dipoles in the material. After the fabrication of the synthetic piezoelectric material, it does not

show much of piezoelectricity effect due to the fact that the directions of electric dipoles in the material are random. These dipoles are aligned by poling process which consists of heating the piezoelectric material above the *Curie* temperature and placing it in a strong electric field.

The basic properties of piezoelectric materials may be expressed mathematically as a relation between the mechanical variables of strain and stress and the electrical variables of electric displacement and electric field. Considering the direct and converse effects in the piezoelectric materials, the linear constitutive relations of these materials may be formulated in indicial notation as [67]

$$\begin{aligned} S_i &= s_{ij}^E T_j + d_{ik} E_k \\ D_m &= d_{mj} T_j + \varepsilon_{mk}^T E_k \end{aligned} \quad (2.1)$$

where i and j take on values between 1 and 6, m and k take on values between 1 and 3, S_i is the mechanical strain, T_j is the mechanical stress, D_m and E_k are the electrical displacement and field, respectively, s_{ij}^E is the mechanical compliance in zero electric field, d_{ik} is the piezoelectric strain coefficient and ε_{mk}^T dielectric permittivity in zero mechanical strain.

A common mixture of materials in making the synthetic piezoelectric materials is lead (Pb), zirconium (Zr) and titanium (Ti). The piezoelectric material made from the combination of these three is lead zirconate titanate, commonly known as PZT, and is the most common piezoelectric material. Other piezoelectric materials are barium titanate and sodium-potassium niobate. Barium titanate was the first synthetic piezoelectric ceramic discovered. The direct piezoelectric effect makes the piezoelectric materials applicable in making sensors and the converse effect may be used for actuation applications. One of the main shortcomings of the piezoelectric materials is their brittleness. Piezoelectric fiber-based materials have been developed in order to enhance the flexibility of these materials. These fiber-based materials consist of piezoceramic fibers (rods) sandwiched between layers of adhesive and flexible surface electrodes. Macro fiber composites (MFC) are one of these flexible materials developed by NASA in 1996 and commercially available since 2002 [3]. While these piezoelectric composite

materials are more flexible and have more diverse applications, they have weaker electromechanical coupling compared to the monolithic ceramics.

2.3. Introduction to the Impedance-based Structural Health Monitoring

The impedance-based SHM is possible through monitoring changes in the measured electrical impedance signatures of self-sensing piezoceramic sensors [69]. This method works through the coupling between the electrical impedance (inverse of the electrical admittance, $Y(\omega)$) of the PZT patches bonded to the host structure and the mechanical impedances of the PZT ($Z_a(\omega)$) and the structure itself ($Z(\omega)$), given in [69] as

$$Y(\omega) = \frac{I}{V} = i\omega a \left(\bar{\epsilon}_{33}^T - \frac{Z(\omega)}{Z(\omega) + Z_a(\omega)} d_{3x}^2 \hat{Y}_{xx}^E \right) \quad (2.2)$$

where V and I are the input voltage to and the output current from the attached PZT patches. a , d_{3x} , \hat{Y}_{xx}^E and $\bar{\epsilon}_{33}^T$ are the geometric constant, the piezoelectric coupling constant, Young's modulus, and the complex dielectric constant of the PZT at zero stress, respectively. The impedance-based technique is not based on any structural model, hence, it is applicable to any complex structure and the measured data can be easily interpreted [11; 62]. It can be applied to the on-line SHM and due to the low required excitation forces it can be run by self-powered systems [93]. It's been shown that the real part of the measured complex impedance is more sensitive to the damage features within the structure while the imaginary part is more temperature sensitive [101; 18; 82].

One of the most common impedance analyzers is the HP 4194A, or its predecessor HP 4192. Using these devices, two parameters related to the impedance will be measured. The most common pair of measurements is the R - X mode which measures the real and imaginary part of the complex impedance. The measurements made through HP impedance analyzer are more precise and can be made in a wide range of frequency. This piece of equipment, however, is rather expensive and bulky, which makes it

unpractical for most of *in-situ* applications. To address the shortcomings related to the HP impedance analyzer, some other setups have been proposed [89; 35; 50; 83].

The measured impedance of the PZT patches provides useful data regarding the health of the host structure. However, this data in its unprocessed, original state does not provide quantifiable information regarding the presence and the state of the damage within the structure. Therefore, processing the measured signal, a feature (or index) needs to be extracted which is sensitive to the damage and insensitive to the other parameters. Damage indices are also favorable as they provide a much smaller set of processed data out of the usually large amount of the recorded data. Different statistical methods are widely used in the impedance-based SHM in order to form damage indices. Some of the linear damage indices are given in the following [104]:

- i. Root mean square deviation (RMSD)

$$RMSD(\%) = \sqrt{\frac{\sum_{i=1}^N (y_i - x_i)^2}{\sum_{i=1}^N x_i^2}} \times 100 \quad (2.3)$$

where x_i and y_i ($i = 1, 2, \dots, N$) are real parts of the electrical impedance (signatures) measured for the structure at the damage-free reference state and the after the damage initiation, respectively.

- ii. Mean absolute percentage deviation (MAPD)

$$MAPD(\%) = \frac{100}{N} \sum_{i=1}^N \left| \frac{y_i - x_i}{x_i} \right| \quad (2.4)$$

- iii. Covariance change (Cov)

$$Cov = \frac{1}{N} \sum_{i=1}^N (x_i - \bar{x})(y_i - \bar{y}) \quad (2.5)$$

Covariance evaluates the averaged product of the deviations of the real part of the impedance from its respective mean. In Eq. (2.5) \bar{x} and \bar{y} are the mean values of

real part of the measured impedance. Covariance determines whether two ranges of data (before and after the initiation of damage) move together. A negative or zero value of the covariance is an indication of the presence of damage in the structure.

iv. Correlation coefficient (CC)

$$CC = \frac{Cov(x,y)}{\sigma_x \sigma_y} \quad (2.6)$$

where σ_x and σ_y are standard deviations of the signature data sets x and y , respectively. The CC is a scaled covariance so that it is independent of the measurement units. The more closely correlated the two signatures (i.e, the healthier the system), the closer the CC is to the value 1. Therefore it is common to use “1-CC” instead of CC in order to have the damage index increase by increasing the severity of damage.

There are also some non-linear feature extraction techniques which will be explained in more details in section 2.4.2.b.

2.4. Experimental Setup and Results

The impedance-based structural health monitoring technique is applied here to experimentally investigate the smallest detectable damage size in the aluminum structures of lug joint specimen and beams. The sensors/actuators used in the electrical impedance measurements were piezoelectric lead zirconate titanate (PZT) circular patches APC-850 WFB made by the APC International, Ltd. (<http://www.americanpiezo.com/>). These circular patches were 6.35 mm (0.25”) in diameter and 0.254 mm (0.01”) in thickness. Some of the material properties of this PZT are listed in Table 2.1.

Table 2.1. Material properties of the PZT circular patches used in the experiments
[\(http://www.americanpiezo.com/\)](http://www.americanpiezo.com/)

Curie Point, T_c ($^{\circ}\text{C}$)	360
Piezoelectric Charge Constant, d_{33} (10^{-12} m/V)	400
Electromechanical Coupling Factor (%)	
k_p	0.63
k_{33}	0.72
k_{31}	0.36
Piezoelectric Voltage Constant, g_{33} (10^{-3} m ² /C)	26
Young's Modulus, (10^{10} Pa)	
Y_{11}^E	6.3
Y_{33}^E	5.4
Density, ρ (g/cm^3)	7.7
Mechanical Quality Factor, Q_m	80

2.4.1. Quantifying the smallest detectable crack in the aluminum lug joints

The lug sample shown in Figure 2.2 is studied in the experimental analysis presented here. The sensor location is as shown in Figure 2.3a, in the center of the lug sample. The PZT sensor is attached to the surface of the lug joint using super glue and pressure. The lug joint sample is fatigued using the Material Testing Systems (MTS), as shown in Figure 2.3b, under 110-1100 lbs constant amplitude loading at 20 Hz frequency. The fatiguing cycle is stopped at every 20k cycles before the crack is visible. This step is reduced to 2.5k cycles after the formation of visible crack and continued until the sample breaks. At each of these fatiguing steps the lug joint was taken off the MTS machine and the electrical impedance of the sample is measured using the HP 4194A Impedance Analyzer, as shown in Figure 2.3c.

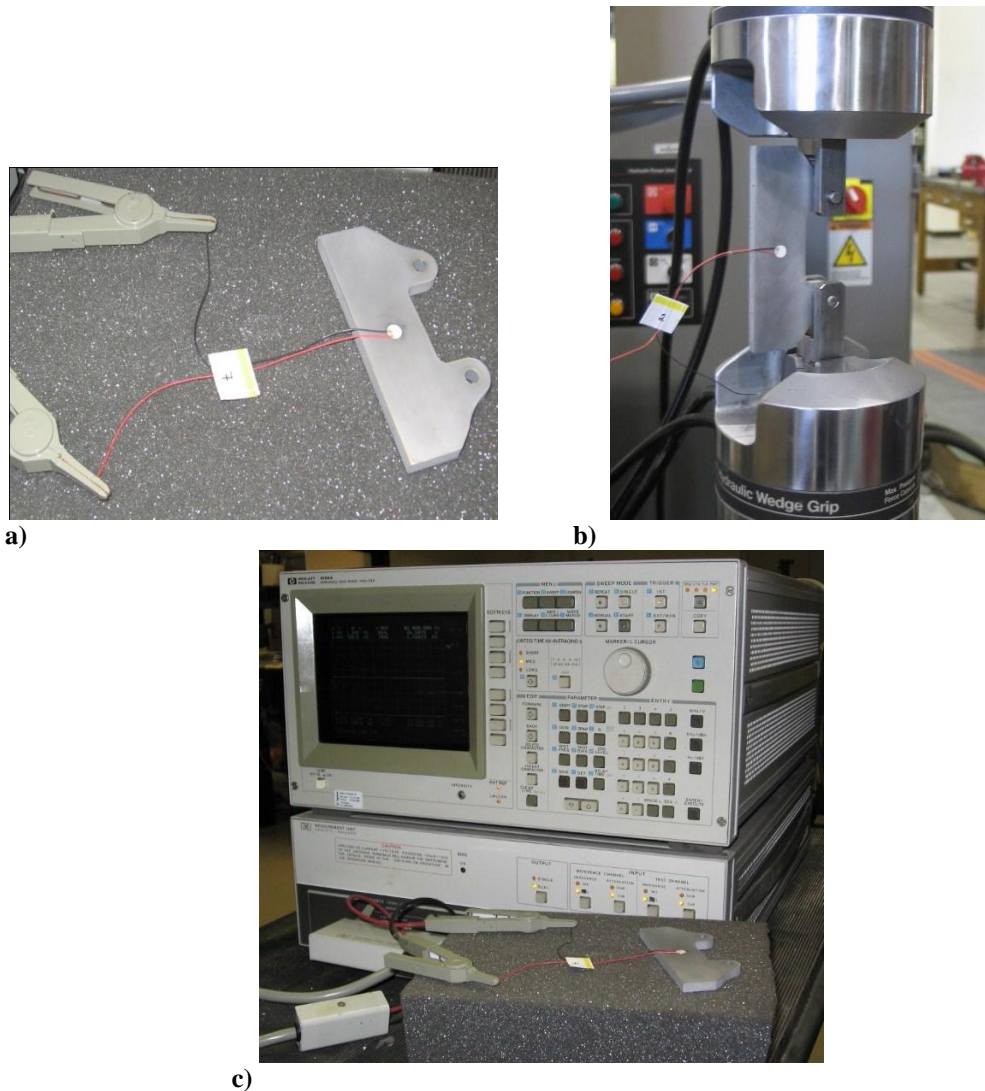


Figure 2.3. Snapshots of the lug joint a) with the surface-bonded PZT, b) assembled in the MTS machine to be fatigued and c) connected to the HP 4194A Impedance Analyzer for the electrical impedance measurements

The fatiguing process was done on various lug joints with identical specifications. The damage index in the form of RMSD and CC were then calculated from the measured electrical impedance of each fatiguing step of every sample. The results, however, did not show any trend in the variation of damage index with respect to the number of fatigue cycles. Various factors could have contributed to this outcome; one being the complex structure of the lug joints and the possibility of crack formation from different hotspots of the structure. In order to investigate this factor, similar experiments were done on aluminum beams with a small notch on one side. The simple structure of the beam and the presence of the notch give better control over the place of initiation and growth of the

crack. These experiments and the results are given in section 2.4.2. One other issue could be the integrity of the PZT sensor and the bonding layer. The PZT and the bonding layer undergo the same fatigue loading as the lug joint itself and are prone to fracture and degradation. Therefore monitoring the integrity of these two insures that the calculated damage index is only related to the possible damage inside the lug joint. The process of PZT and bonding layer health monitoring is also explained in section 2.4.2.a. Moreover, in order to better extract the fatigue crack damage features from the measured electrical impedance, the ARX non-linear feature extraction is employed as described in section 2.4.2.b.

2.4.2. Quantifying the smallest detectable crack in aluminum beam samples

The experimental procedure used for fatiguing the aluminum beams was similar to that of the lug samples described in the previous section. Multiple aluminum beam specimens of the size 12"×1"×1/8" with a 1/8" notch in the middle, as shown in Figure 2.4, were fatigued in the following experiments and their electrical impedance was measured at certain fatigue cycles, using the HP 4194A impedance analyzer. The fatiguing was done at the loading of 110-1100 lb and the loading frequency of 20 Hz. Fatiguing was stopped at 30k, 50k, 70k, 80k, 82.5k and 85k cycles for the electrical impedance to be measured.

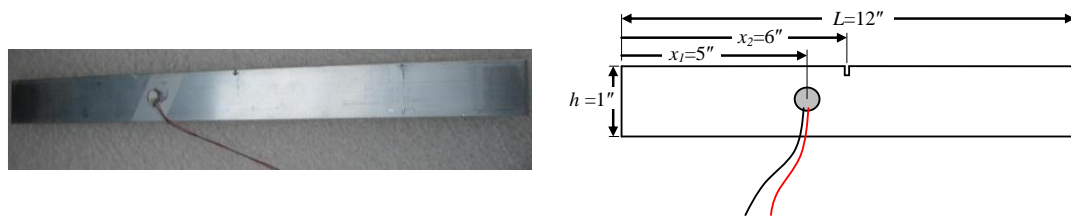


Figure 2.4. Schematics of the aluminum beam fatigued and tested

Damage indices in the form of cross correlation (CC) were calculated for each fatiguing step and compared for different aluminum beams. Applying the linear CC damage index formulation, no trend in the variation of these indices and the generation and growth of the crack in the beams was identified. Similar to what was explained in the previous chapter, there could have been different factors and parameters that needed to be investigated. One of these parameters, especially for fatiguing experiments, was the

integrity of the PZT sensors and the adhesive layer and was investigated as explained in section 2.4.2.a. Moreover, due to the nature of the damage in the form of a fatigue crack (compared to cuts or added masses) the possibility of damage detection using non-linear feature extractions was investigated as given in section 2.4.2.b.

2.4.2.a.PZT Self-Diagnosis

The embedded or surface-attached sensors and actuators used in the SHM practices is exposed to the same external loading as the structure and is prone to formation of damage in the form a crack just like the structure, especially for brittle piezoceramic sensors. Moreover, most of the structures being monitored along with the surface-bonded sensors and actuators are exposed to harsh environments. One other important concern regarding the functionality of the surface-bonded sensors used in SHM applications is the condition of the bonding layer between the sensor and the host structure. This factor is crucially important for the electrical impedance-based SHM since the concept and applicability of this method depends upon the electro-mechanical coupling between the host structure and the sensor/actuator. The coupling between the mechanical impedance of the host structure and the measured electrical impedance of the surface-bonded sensors modeled according the impedance-based SHM is possible only through an ideal bonding between the two parts. If the host structure is placed is exposed to harsh environmental factors, such as elevated ambient temperatures, or undergoes external loading, the bonding layer between the sensors and the host structure might deviate from being ideal or even the sensors might get partially or completely de-bonded. Therefore, in order to guarantee the functionality of surface bonded sensors and actuators used in the SHM applications, the integrity of theses transducers need to be monitored as well as the integrity of the host structure itself.

One of the practical procedures in monitoring the integrity of the surface-bonded piezoceramic sensors as well as the bonding layer between these sensors and the host structure is the self-diagnosis of the piezoceramic sensors which is based on the processing of the measured electrical admittance through these sensors [80]. According to this procedure, change in the integrity of the piezoceramic sensors as well as the

condition of the bonding layer may be monitored by monitoring the variations in the imaginary part of the measured electrical admittance (reciprocal of the impedance).

In order to apply this method, the electrical impedance of the free piezoceramic patch needs to be recorded prior to the surface attachment. Plotting the imaginary part of the electrical admittance measured for a free piezoceramic patch versus the frequency results in a line with a specific slope. This slope is analogous to the capacitive values of the piezoceramic patch [80]. The attachment of the sensor on to the surface of the host structure causes a significant downward shift in this slope. This measured data (the electrical admittance of the attached sensor prior to any loading) is used as the baseline in the further processing of the integrity monitoring of the piezoceramic sensors. Throughout the operational life of the piezoceramic sensors, the slope of the imaginary part of the admittance versus the frequency is monitored. An upward shift in this slope compared to the baseline is an indication of sensor getting de-bonded from the surface of the host structure (the capacitance is getting closer to that of a free sensor patch). Moreover, the loss of integrity and breakage of the piezoceramic sensor patch causes a downward shift in the slope of the imaginary part of the measured admittance versus the frequency [80]. The main advantage of this method is that the integrity of the piezoceramic patches may be monitored by processing the same data that is measured for monitoring the integrity of the host structure and no extra data needs to be recorded.

In the beam fatiguing experiment, the piezoceramic (PZT) sensor needs to be attached to the surface of the beam prior to the loading and the electrical impedance of the PZT patch needs to be measured to be used as the baseline in the health monitoring processing. The electrical impedance of each PZT patch needs to be also measured prior to being bonded to the surface of the host structure. The slope of the electrical admittance versus the frequency is monitored throughout the fatiguing of the beams in order to track the integrity of the PZT patch and the bonding layer. The electrical admittance versus the frequency is plotted for 6 different beams at the baseline and six different loading cycles of 30k, 50k, 70k, 80k, 82.5k and 85k as well as the free PZT patch. These graphs are shown in Figure 2.5 for the frequency range of 10-60 kHz.

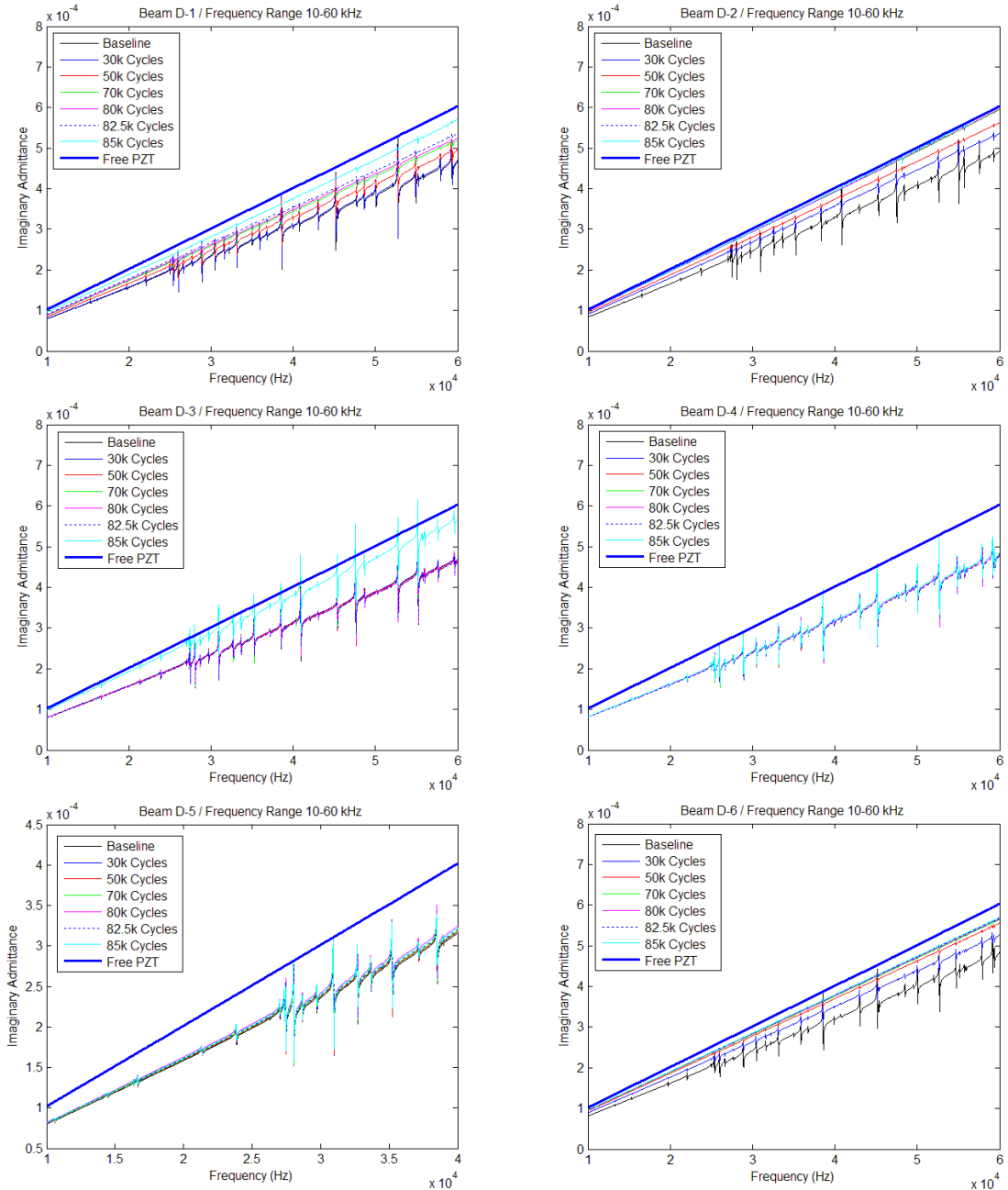


Figure 2.5. The electrical admittance versus the frequency for beams “D-1”-“D-6” at seven different loading cycles of zero (Baseline), 30k, 50k, 70k, 80k, 82.5k and 85k and the free PZT patch for the frequency range of 10-60 kHz

It is seen from Figure 2.5 that only the PZT patches bonded to the surface of the two beams of D-4 and D-5 remain intact during the fatiguing process. As for the beams D-1, D-2 and D-6, a gradual de-bonding of the PZT patch from the surface of the beam is seen as the number of fatigue cycles increases. For the beam D-3, on the other hand, the

bonded PZT patch gets mostly de-bonded between the 82.5k and the 85k fatiguing cycles.

If the integrity of the PZT sensor and the bonding layer is not monitored or taken into consideration, the damage index calculated from the electrical impedance measured from the PZT sensors may be misinterpreted. Considering beam number D-1, the damage index CC may be calculated for the measured electrical impedance as shown in Figure 2.6a. If the integrity of the PZT and the bonding layer is not taken into consideration, it could be deduced from the variations of the damage index that a fatigue crack had been formed between 80k and 82.5k fatiguing cycles. However, by considering the variations of the imaginary admittance with respect to the frequency as given in Figure 2.6b it may be observed that the PZT layer is mostly de-bonded at these two states.

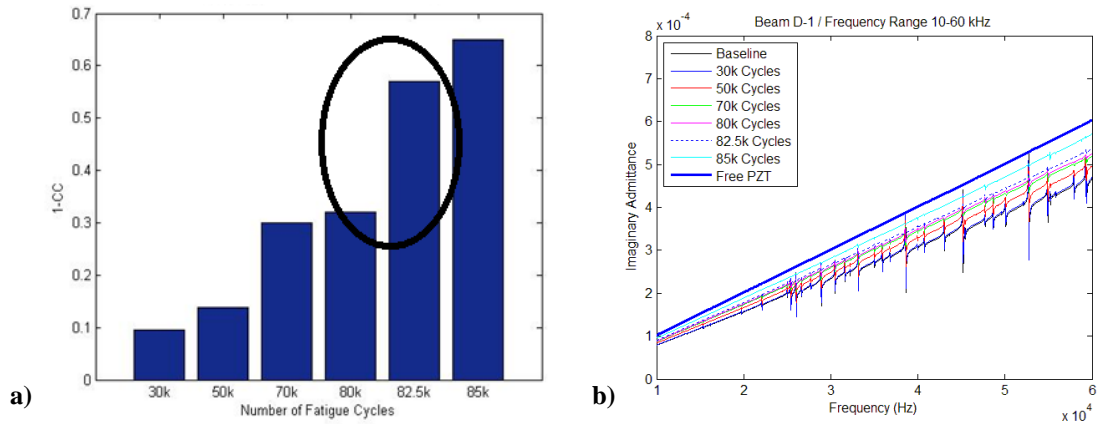


Figure 2.6. a) Damage index calculated for beam D-1 over the frequency range of 30-60 kHz and b) the electrical admittance versus the frequency for this beam at different fatigue cycles

As observed in the above mentioned PZT self diagnosis results, the PZT patches bonded to the surface of the structure (here beams) and used in the measurements of the electrical impedance are prone to fatiguing and become de-bonded from the surface of the structure before the damage has reached a detectable state. On the other hand, by detecting that the PZT has been de-bonded from the surface, it cannot be re-attached, since the electromechanical coupling between the PZT sensor and the host structure needs to remain unchanged compared to the damage-free reference state. This coupling is correlated with the adhesive (bonding) layer condition. Therefore, the application of PZT sensors and the impedance-based SHM could impose a dilemma on the health monitoring

of a structure undergoing fatigue loading. Therefore, more sophisticated methods of bonding and embedding need to be considered for the PZT transducers that are beyond the scope of the present study. As a result, other methods of the structural health monitoring need to be investigated for monitoring the initiation and growth of fatigue cracks different aluminum samples. Vibration-based health monitoring of cracks growth in beams structures are analytically and numerically studied in chapter 5.

2.4.2.b. Non-linear feature extraction of frequency-domain ARX model

The measured impedance of the PZT patches provides useful data regarding the health of the host structure. However, as explained earlier, this data in its unprocessed state does not provide quantifiable information regarding the presence and the state of the damage within the structure. Some of the statistical methods used in calculating linear damage indices were given earlier in section 2.3. These linear damage indices are very practical in detecting the presence of macro-scale damage, however, non-linear feature extractions would be more accurate in detecting damage initiation while in micro-scale.

In the non-linear feature extraction of frequency-domain ARX model, the output at a specific frequency, $y(\omega_k)$, is related to the input at that frequency and the outputs to a finite number of its surrounding frequencies.

The ARX model comes in different forms depending on the number and the order of surrounding frequencies included in the model. The simplest frequency-domain ARX model of the first order is given as

$$Y(k) = B(k)U(k) + A_1(k)Y(k - 1) + A_{-1}(k)Y(k + 1) \quad (2.7)$$

where k is the frequency counter, $B(k)$ is the exogenous coefficient, $A_1(k)$ and $A_{-1}(k)$ are the frequency-domain autoregressive (AR) coefficient, $U(k)$ is the input at the k^{th} frequency and $Y(k - 1)$, $Y(k)$ and $Y(k + 1)$ are the outputs at $(k - 1)^{\text{th}}$, k^{th} and $(k + 1)^{\text{th}}$ frequency, respectively. The first term in Eq. (2.7) accounts for the nominal linear dynamics and the other two terms (the AR series) account for the non-linear, multi-harmonic nature of the response spectrum [4].

The sensitivity of damage extraction technique to the change in the structure's integrity also depends on the choice of frequency range over which the impedance is

measured. This range is suggested to be the one containing 20-30 peaks and therefore including a high density of the structure's modes [101]. The common high-frequency band for the electrical impedance measurement ranges from 30 kHz up to 400 kHz [82]. The appropriate frequency range for a given structure, however, is determined by trial-and-error.

2.4.2.b.I. Experimental setup and results

The goal of the experiments in this section is to investigate whether it is possible to detect the nucleation of the fatigue crack at the micro-level size by applying the non-linear feature extraction methods to the impedance-based SHM. In the first set of experiments, two aluminum beam specimens of the size 12"×1"×1/8" with a 1/8" notch in the middle, as shown in Figure 2.7a, were fatigued and their electrical impedance was measured at certain fatigue cycles, using the HP 4194A impedance analyzer, as shown in Figure 2.7. The fatiguing was done at the loading of 300-1300 lb and the loading frequency of 20 Hz. Fatiguing was stopped at 30k, 50k, 70k, 80k, 82.5k and 85k cycles for the electrical impedance to be measured.

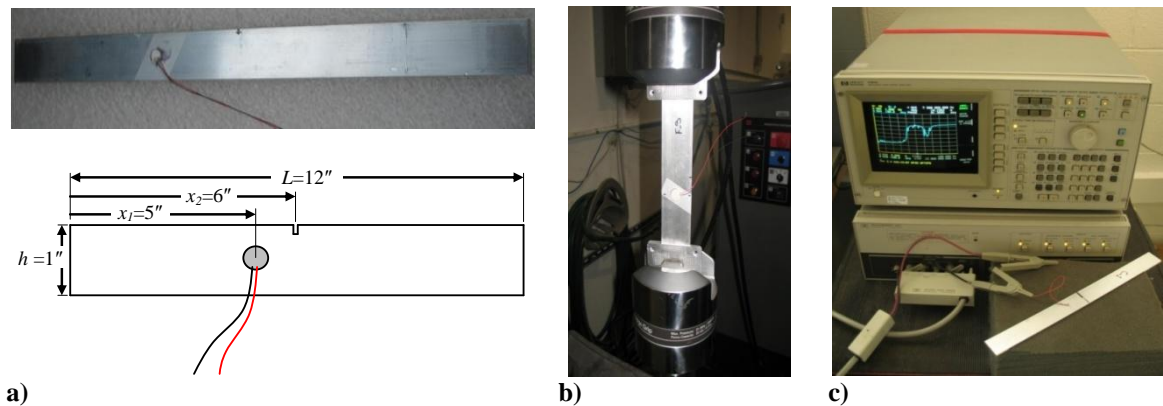


Figure 2.7. Schematics of a) the aluminum beam fatigued and tested, b) the MTS machine used in fatiguing and c) the HP 4194A impedance analyzer [8]

The correlation coefficient (CC) of the real part of measured electrical impedance through the attached circular PZT patch was then calculated for the frequency range of 50-80 kHz (this range of frequency was found to be more sensitive to the damage in these aluminum beams). The damage index is formed by calculating the CC between the results

of each fatigue step to the one for the intact beam. These results for the two beams of B1 and B2 are shown in Figure 2.8.

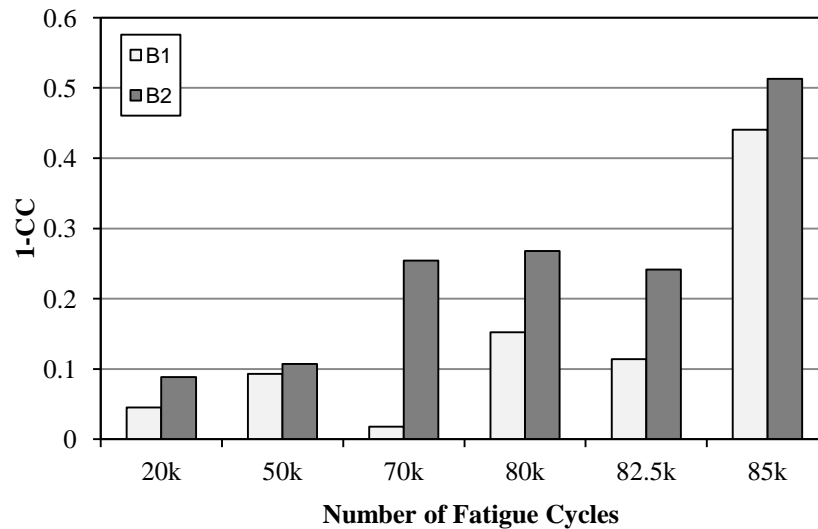


Figure 2.8. Damage index (1-CC) of the two aluminum beams, B1 and B2, in the frequency range of 50-80 kHz of the electrical impedance measurements [8]

It is clearly seen that by increasing the number of loading cycle, the amount of (1-CC) increases, which is a sign of growing defect in the beams. Both beams were found to have visible fatigue cracks at the groove of their notch. Looking at the cracks on these beams using a microscope (with 10x zooming), it was seen that the length of the crack in beam B2 is more than the one in beam B1, as shown in Figure 2.9. In other words, the damage is more severe and progressed for B2 than B1, which is clearly and qualitatively observed from the results of Figure 2.8.

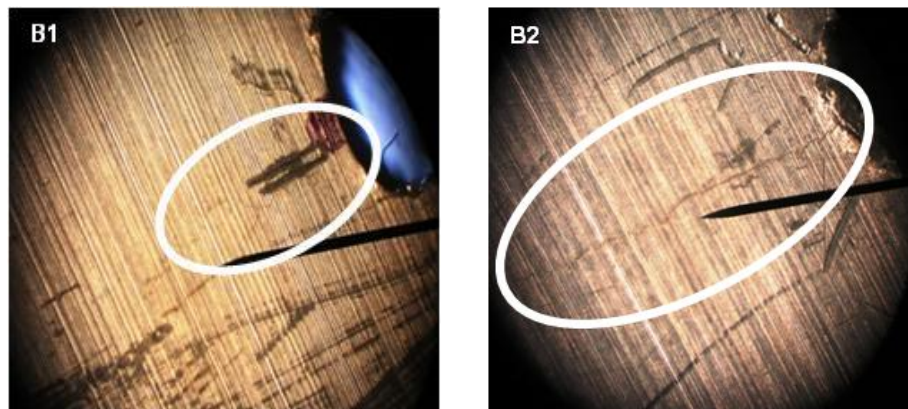


Figure 2.9. Snapshots of the fatigue cracks in a) beam B1 and b) beam B2 [8]

While the aluminum test specimens show global linearity, it was expected that the presence of fatigue cracks and their breathing under the PZT-induced local high-frequency excitation would introduce non-linearity into the structure. In order to verify this concept, the second set of experiments is done on an aluminum beam (T1) with the same structural specification as beams B1 and B2. The non-linearity assumption of the fatigued Al beam is investigated from two different paths; one by applying the ARX model feature extraction method to the real part of the measured electrical impedance at the same frequency range of 50-80 kHz, and two by comparing the damage index of the beam at three different input voltages to the system. The specimen was fatigued up to 120k cycles and the impedance was recorded for the three input voltages at almost every 10k cycle step. It is important to note that the fatigue crack wasn't visible up to the 120k fatigue cycles for this test beam.

The frequency-domain ARX model was used to extract the non-linear features of the beam. The non-linear damage index together with the linear one (for the real part of the electrical-impedance measured at 1.0V) is shown in Figure 2.10 for beam T1 over the frequency range of 50-80 kHz. It is clearly shown that by applying the non-linear feature extraction model, the micro-cracking effect may be observed, at the 100k-110k fatiguing.

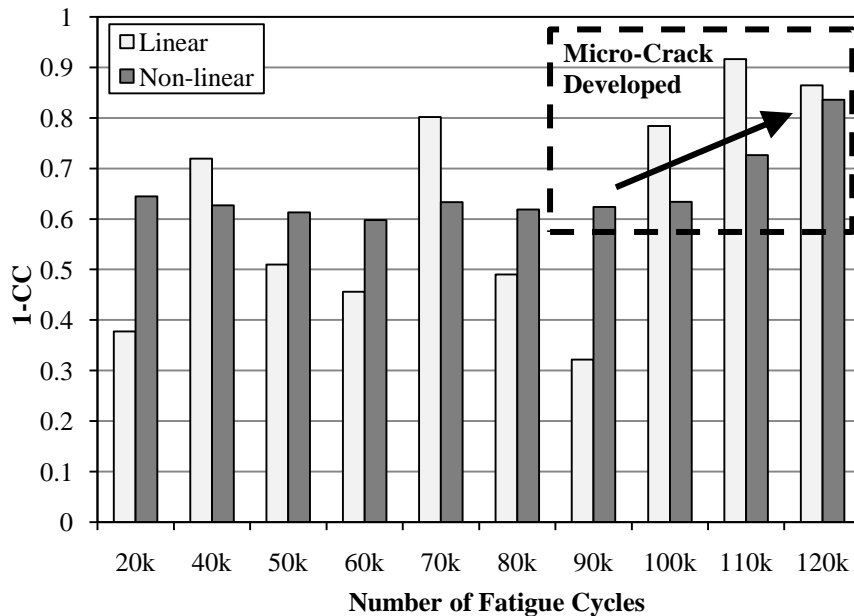


Figure 2.10. The comparison of linear and non-linear damage indices for beam T1 over the frequency range of 50-80 kHz and the input voltage of 1.0V [8]

It is known that one of the characteristics of a linear system is that by multiplying the input by a specific value, its output will also be multiplied by the same value. In the case of the electrical-impedance being measured as the output and processed for calculating the damage index, the effect of input-change on the output needs to be interpreted in a different fashion, as follows. The change (e.g. increase) in the input voltage of a linear structure will change (e.g. increase) the value of the measured impedance. However, it won't shift the resonance peaks in the response signature. In other words, the outputs of two different input voltages will remain closely correlated, resulting in a CC close to 1 (or "1-CC" close to zero). On the other hand, changing the input voltage of a non-linear system will excite different sub-harmonics, resulting in a non-negligible "1-CC" between the outputs of different input levels. The electrical impedance is measured for this beam (T1) at three different input voltages in order to investigate the non-linearity in the test beam caused by the presence of a fatigue crack. The input voltage of the HP 4194A impedance analyzer is limited in the range of 0-1.0 V. Therefore, the three input voltages of 0.2, 0.6 and 1.0 V were chosen. Using the CC over the frequency range of 50-80 kHz of the measured electrical impedance, the linear damage indices were calculated for comparison of the outputs of the input voltages of 0.6V and 1.0V with the 0.2V. These results are shown in Figure 2.11.

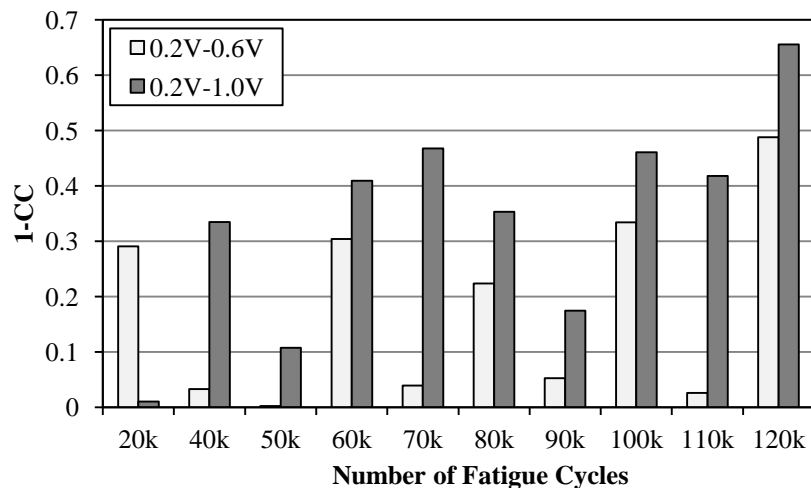


Figure 2.11. The correlation coefficient of the measured electrical-impedance for different input voltages to a fatigued aluminum beam at different fatigue cycles [8]

It is clearly seen that in most of the cases, the outputs of different voltage levels are not well correlated, verifying the concept of structural non-linearity in a fatigued beam. It is also shown in Figure 2.11 that the output of the two input voltages of 0.2V and 0.6V (light grey bar) are better correlated compared to that of the 0.2V and 1.0V (dark grey bar). In other words, as the difference in the input voltages gets more, the outputs become less correlated, which may be interpreted as the increased number of sub-harmonics being excited at higher input voltages.

The final step in verifying the concept of non-linearity being introduced by formation and growth of fatigue cracks was to repeat the previous set of experiment, this time to a system with more likely linear type of damage. The saw-cut was considered to be an appropriate candidate for such a linear damage. In this set of experiments, the cuts were made in a similar aluminum beam with an increasing size and the electrical-impedance was measured at each 1/16"-cut and for the three different input voltages of 0.2, 0.6 and 1.0V, for 8 steps of the saw-cut. The measured electrical-impedance was processed in a manner similar to the second set of experiments and the results are shown in Figure 2.12. It is clearly seen that the outputs of different input voltages are closely correlated (with the value of "1-CC" close to zero), which verifies the assumed linear structure for a beam with the saw-cut, as opposed to the nonlinearity introduced to the beams due to the presence of fatigue cracks.

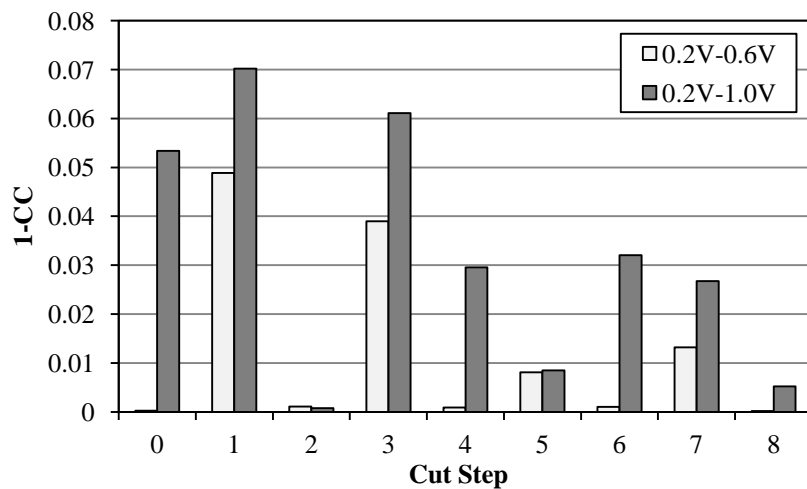


Figure 2.12. The correlation coefficient of the measured electrical-impedance for different input voltages to an aluminum beam at different saw cuts [8]

2.5. The Effect of Temperature on the Impedance-based Monitoring of the Growth of Damage in Lug Samples

The impedance-based structural health monitoring method is based on the assumption that in the electromechanical coupling as formulated in Eq. (2.2) all of the parameters except the mechanical impedance of the structure remain unchanged during the formation of damage in the structure. Earlier in section 2.4.2.a the variations in the mechanical impedance of the PZT sensor was studied and a PZT-diagnosis method was examined. Another factor that can change the parameters in Eq. (2.2) is the change in the environmental factors such as temperature. The material properties of the PZT such as d_{3x} , \hat{Y}_{xx}^E and $\bar{\epsilon}_{33}^T$ as well as the Young's modulus of the host structure are known to be temperature-dependent. Therefore if the ambient temperature is varied, the impedance-based SHM shows variations in the integrity of the host structure while there exist none. There have been past efforts in compensating the effect of temperature in the impedance-based structural health monitoring practices [81].

In this section, the effect of temperature on three large lug samples is studied. These samples, shown in Figure 2.13, were three times the size of the lug samples shown in Figure 2.1. Two of these lugs were already fatigued and have fatigue cracks of length 0.314" (for sample 4) and 0.684" (for sample 2). The un-cracked lug was used as the baseline in the calculation of damage indices, since the lug samples were damaged without any data collected in their healthy state. Data collection in these samples was done through surface-bonded macro fiber composite (MFC) sensors as shown in Figure 2.13. The electrical impedance of the samples was measured at six different temperature set points of 25, 35, 45, 55, 65 and 75°C. In order to provide varying temperature set points the environmental/temperature chamber shown in Figure 2.14 was used.

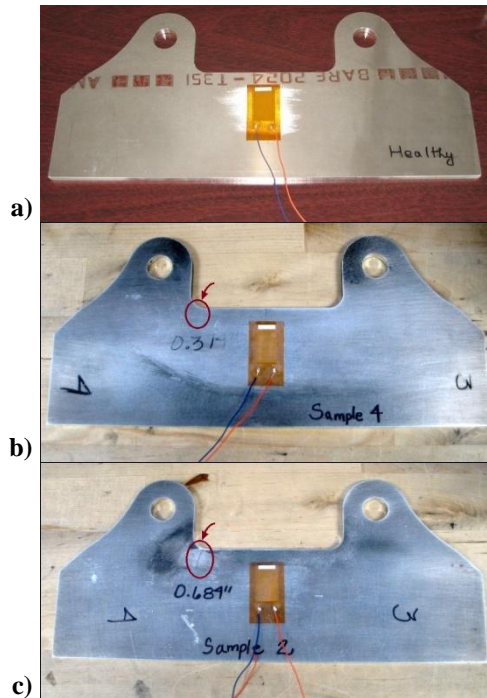


Figure 2.13. Snapshots of the a) healthy large lug joint, b) cracked large lug joint with the crack length of 0.314", and c) cracked large lug joint with the crack length of 0.684"



Figure 2.14. The environmental chamber

The real part of the measured electrical impedance of each of the three samples is plotted versus the frequency for the frequency range of 12.4-12.8 kHz in Figure 2.15. This range of frequency has been chosen for better depiction of the variations of the real impedance with respect to temperature and damage.

The damage index in the form of RMSD (%) has also been calculated for the measured electrical impedance and is given in Figure 2.16 and Figure 2.17. Different frequency ranges have been studied and two ranges have been chosen as the most

sensitive to the damage presence in the lug specimen. This frequency range, as mentioned before, is found by trial and error. It should be noted that the damage index shown in Figure 2.16 is calculated for each sample considering the measurements of that same sample in temperature set point of 25°C. Two different frequencies of 12.4-12.8 and 13.6-14 kHz are shown in this figure.

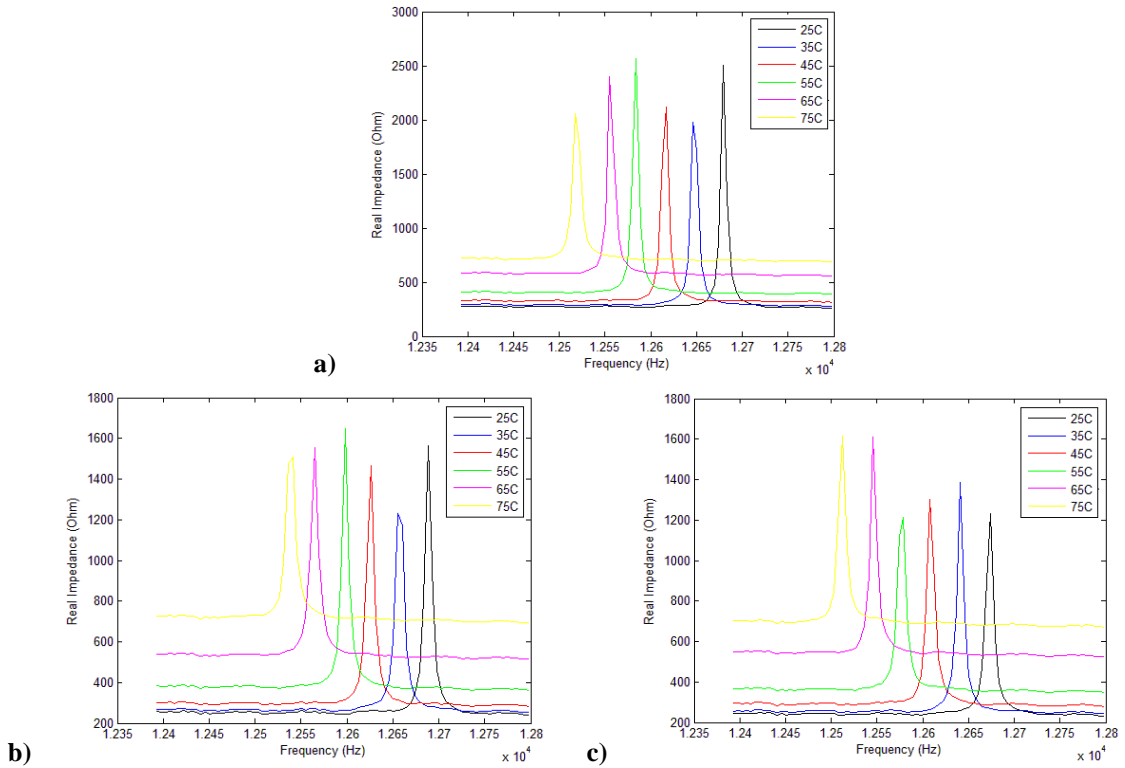


Figure 2.15. a) Healthy, b) Sample 4, c) Sample 2

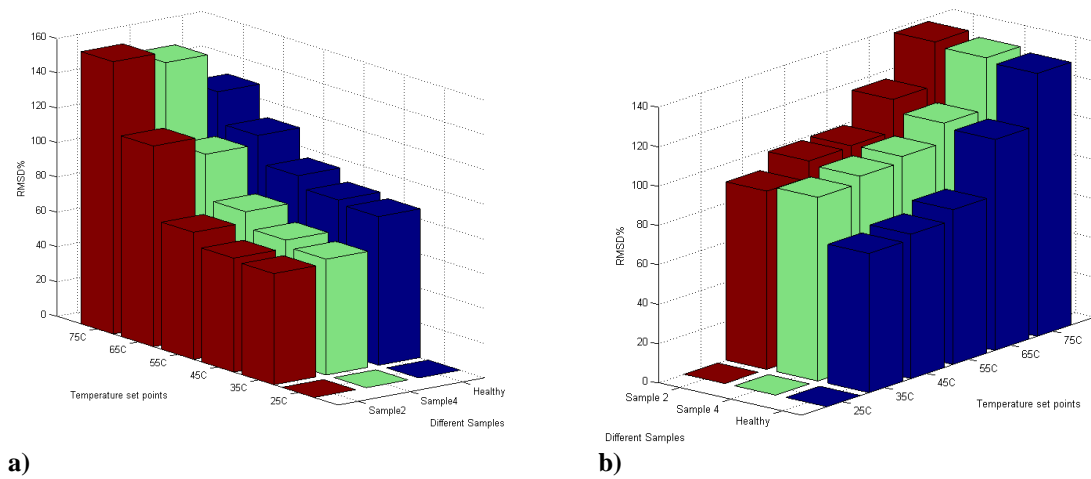


Figure 2.16. RMSD calculated For each lug sample, baseline is the measurement at 25°C of the same lug for the frequency range of a) 12.4-12.8 kHz and b) 13.6-14 kHz

In Figure 2.17, however, the baseline and reference in the calculations of the damage index is the electrical impedance measured at temperature set point of 25°C for the healthy lug sample. The frequency range considered in these damage index calculations are 12.4-12.8 kHz.

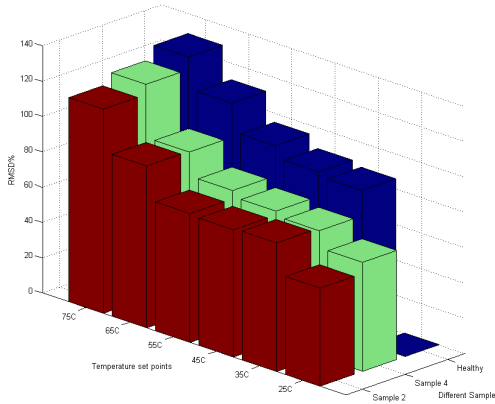


Figure 2.17. RMSD calculated for frequency range of 12.4-12.8 kHz, For each lug sample, baseline is the measurement at 25°C of the Healthy lug

As clearly shown in Figure 2.16, temperature variations causes variations in the damage index of the lug samples for the healthy and damaged ones. More tests would be necessary with more variations on the length of the crack in the lug samples in order to quantify and separate the two effects of fatigue crack and temperature variations in the impedance-based structural health monitoring.

2.6. Chapter Summary

The work presented in this chapter was the analytical and experimental studies as part of the Structural Health Monitoring (SHM) Multidisciplinary University Research Initiative (MURI) project established in 2006 and funded by the Air Force Office of Scientific Research (AFOSR). The main focus of the MURI team at Virginia Tech was to propose and examine methods and models for *in situ* interrogation and detection of damage in the specimen. This was done by applying the impedance-based SHM method and using piezoceramic sensors and actuators.

The impedance-based structural health monitoring technique was applied here to experimentally investigate the smallest detectable damage size in the aluminum structures of lug joint specimen and beams. In this SHM method the measured electrical impedance from the piezoceramic sensors (which are coupled to the mechanical impedance of the samples) were continuously compared to that of a damage-free reference state. This comparison was done throughout the fatiguing process of the lug samples at different fatigue cycles and damage states. The fatiguing process was done on various lug joints with identical specifications. The damage index in the form of RMSD and CC were then calculated from the measured electrical impedance of each fatiguing step of every sample. The results, however, did not show any trend in the variation of damage index with respect to the number of fatigue cycles. Various factors were considered to have contributed to this outcome; one being the complex structure of the lug joints and the possibility of crack formation from different hotspots of the structure. In order to investigate this factor, similar experiments were done on aluminum beams with a small notch on one side.

One other issue considered was the integrity of the PZT sensor and the bonding layer. The PZT and the bonding layer underwent the same fatigue loading as the lug joint itself and were prone to fracture and degradation. Therefore the integrity of these two was monitored as well to insure that the calculated damage index was only related to the possible damage inside the lug joint. It was observed in the PZT self diagnosis procedure that the PZT patches bonded to the surface of the structure and used in the measurements of the electrical impedance got de-bonded from the surface of the structure before the damage had reached a detectable state. On the other hand, by detecting that the PZT had been de-bonded from the surface, it could not be re-attached, since the electromechanical coupling between the PZT sensor and the host structure needed to remain unchanged compared to the damage-free reference state. The application of PZT sensors and the impedance-based SHM was, therefore, found to impose a dilemma on the health monitoring of a structure undergoing fatigue loading. As a result, other methods of the structural health monitoring, such as the vibration-based SHM, were considered to be better choices for monitoring the initiation and growth of fatigue cracks.

Moreover, in order to better extract the fatigue crack damage features from the measured electrical impedance, the ARX non-linear feature extraction was employed. It was shown that applying this method of feature extraction resulted in observing a trend in the variation of damage index as the number of fatigue cycles increased. From the experimental results provided for the aluminum beam studied here, the damage index calculated using the non-linear feature extraction was shown to remain unchanged up to the 100k fatigue cycles and have a sudden change for the 110k fatigue cycles. The damage index was shown to grow monotonically for the fatigue cycles larger than 110k. This was interpreted as the initiation of a micro-crack inside the beam that has not yet reached a visible state. Such trend in the variation of damage index was not seen when the linear feature extraction was applied. Therefore, the non-linear feature extraction would be helpful in improving the early detection of fatigue cracks in structures compared to the linear method.

Using three different input voltages of 0.2, 0.6 and 1.0V of the HP 4194A impedance analyzer, the measured impedances were compared to examine the validity of considering fatigue cracks with non-linear structural behavior. It was shown that as the difference between the two input voltages increase, the correlation between the outputs gets less. This verified the presence of non-linearity in a beam's structure having fatigue cracks. It was later shown that repeating the same set of experiment for a growing saw-cut (which is intuitively assumed to have a linear structural behavior) resulted in close correlation between the outputs for different levels of input voltage.

Another factor affecting the electromechanical coupling in the impedance-based SHM was considered to be the change in the environmental factors such as temperature. The effect of temperature on three large lug samples was studied by measuring the electrical impedance of the lug samples at six different temperature set points of 25, 35, 45, 55, 65 and 75°C using the environmental/temperature chamber. It was shown, through calculation of damage indices of the measured electrical impedance, that temperature variations cause variations in the damage index of the lug samples for the healthy and damaged cases. In other words, if the ambient temperature was varied, the impedance-based SHM would show variations in the integrity of the host structure while there existed none. More tests would be necessary with more variations on the length of

the crack in the lug samples in order to quantify and separate the two effects of fatigue crack and temperature variations in the impedance-based structural health monitoring.

AUTOMATED STRUCTURAL HEALTH MONITORING OF BOLTED JOINTS IN RAILROAD SWITCHES

Monitoring the integrity of railway switch systems is a key factor in preventing train derailments. Conventional switch inspection on the rail systems is a labor intensive and sometimes unreliable approach to maintaining the switch integrity. In this chapter, an effective health monitoring method is described which eliminates the need for frequent visual inspection of railway switches by totally automating inspection of the switches' mechanical condition. This chapter focuses on the use of smart materials and structures and the electrical impedance-based method for the health monitoring of bolted joints in railroad switches.

3.1. Motivations

Current switch bolt inspection on rail systems is a labor intensive and sometimes unreliable approach to maintaining the switch integrity. Recent rail accidents in the United Kingdom (Potters Bar in 2002 and Grayrigg in 2007) underscore the need for routine inspections of the switch mechanisms. From the Grayrigg report of 26 February 2007 the main causes of the accident were suspected to be the rupture of the bolts of the switch bars, especially the one maintaining the switch rails at a correct distance apart [88]. Such findings also resulted from the 2002 crash report but unfortunately frequent visual inspections were not forthcoming.

In the following experimental setup the loosening of nuts and bolts is studied as one of the major causes of train derailment and the impedance-based SHM method is

applied for indicating this type of damages in the switch system. As described earlier in chapter 2, the impedance-based SHM utilizes piezoceramic wafers as the self-sensing components which are subject to the same harsh environmental conditions as the monitored structure, especially in the case of railroad switches. Therefore, in the present work, the electrical impedance measurements are used for monitoring the integrity of the switch structure as well that of the piezoceramic transducers to maintain their.

3.2. Overview of the Railroad Switches and Their Components

Railroad *switches* (aka *turnouts* or *points*) are mechanical installations enabling trains to switch from one railway track to another at a junction. This route selection is carried by two rails, known as *switch rails*, movable from one side of the track to the other side, as shown in Figure 3.1.

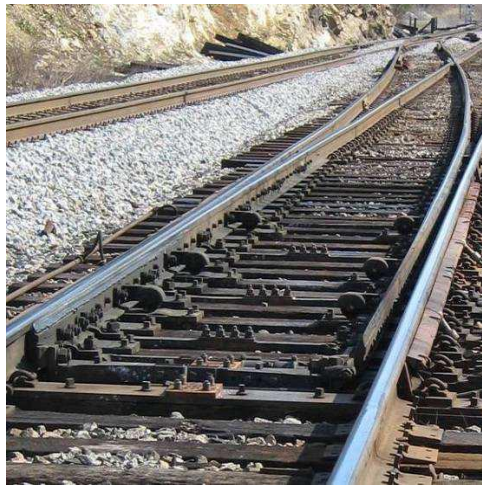


Figure 3.1. A snapshot of a railroad switch

These two switch rails are kept apart at a set distance and are moved at the same time by a series of *switch rods* (aka *stretcher bars*), shown in Figure 3.2a. In order not to interfere with the track signaling circuit, switch rods are divided into two parts, joined by an insulated bolted joint, as shown in Figure 3.2b.



Figure 3.2. Snapshots of a) a switch rod and b) an insulated bolted joint

The bar at the movable end of the switches is connected to the *detector*, which indicates whether the switches are correctly positioned. This bar is called the *lock rod* and is shown in Figure 3.3a. Switch rails and switch rods are connected to each other by *clips* made of steel, bolted to both parts, shown in Figure 3.3b.



Figure 3.3. Snapshots of a) a lock rod and b) its clip

Switch rods are one of the important parts regarding the functionality of railway switches and are prone to the loosening of their bolted clips and breakage. Failure or loosening of these rods is one of the major causes of train derailments.

3.3. Rail Track Experimental Set-up and Results

A full scale prototype of a real switch track shown in Figure 3.4 was made by Thomas Marquié at the Center for Intelligent Material Systems and Structures (CIMSS). This prototype was machined from A36 steel with the Young's modulus of 200 GPa; close to that of the R260 steel. A detailed description of this full scale prototype is given in Appendix A.

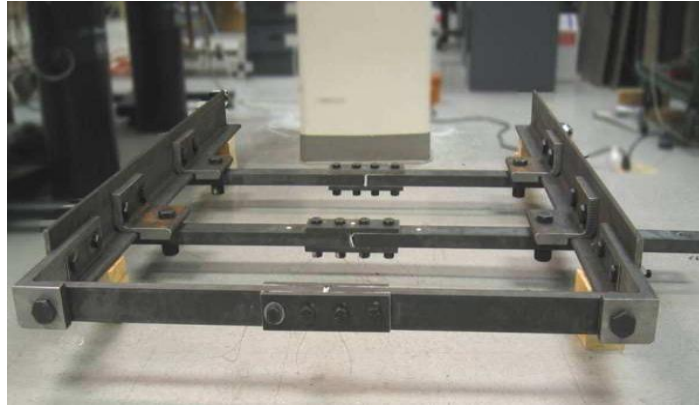


Figure 3.4. Laboratory prototype of a rail system with bolted joints

The two parts of the switch rods were insulated using the fiberglass Insulation Paper, 1/8" thick, 16" width and 10' length as shown in Figure 3.5.

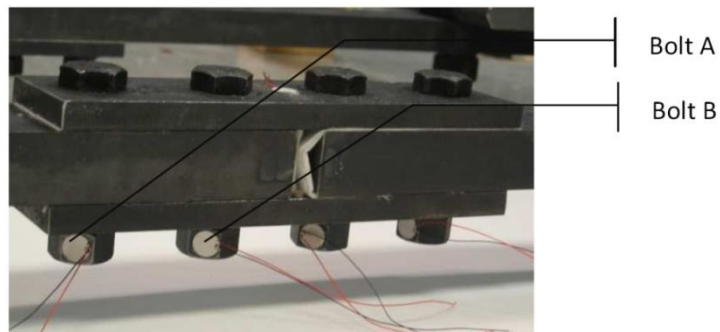


Figure 3.5. Insulated bolted joint in the experimental prototype with the PZT patches glued to the nuts

Wired, circular piezoceramic (PZT) wafers were used in the impedance measurements in the experimental setup. They were both attached to the nuts and the rods' surfaces, as shown in Figure 3.5 and Figure 3.6.



Figure 3.6. PZT patches attached to the switch rod surface

3.3.1. Detection of the Bolts Loosening

In order to detect the loosening of the bolts, PZT patches are attached to the nuts of the four connecting bolts of one the switch rods, as shown in Figure 3.5. The bolts loosening are detected by examining the electrical impedance measured by two of these PZT sensors. The sensitivity of each of these two PZT sensors is also investigated.

3.3.1.a. On-nut Detection

The purpose of this experiment was to determine if $\frac{1}{4}$ turn loosening of a switch track's bolt could be detectable via the impedance-based SHM method. All the bolts were tightened up to 75 ft-lbs and the PZT's electrical impedance (baseline) was measured using the HP 4194A impedance analyzer. The measurements were repeated having bolt A, shown in Figure 3.5, loosened for of a quarter of turn, which was equivalent to a torque of 10 ft-lbs. The loosened bolt was retightened and the impedance was measured. The real part of the measured impedance of these three cases is shown in Figure 3.7a for the frequency range of 70 kHz to 120 kHz.

In order to quantify these three measurements, their RMSD metrics were calculated and are shown in Figure 3.7b.

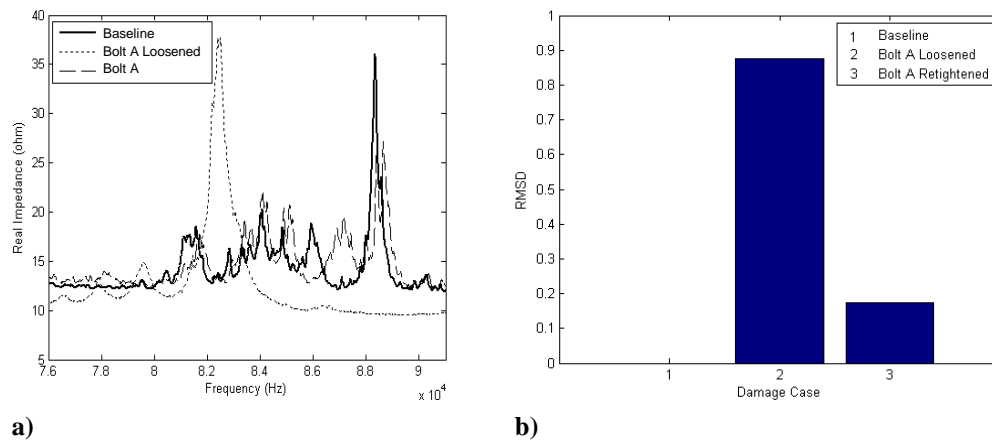


Figure 3.7. a) Impedance signatures of the loosened and retightened bolt A and b) their RMSD Damage metric

The comparison of RMSD values shows that a quarter turn of a bolt can be clearly detected by measuring the electrical impedance of a PZT Patch at the bolted connection.

Additionally, the RMSD calculated for the retightened bolt will be used for introducing a threshold to the detection of a loosened bolt.

The next step was to determine the change in the measured impedances and RMSD metrics while the tightening torque of the bolt is decreased in steps from 75 ft-lbs down to the 15 ft-lbs. These different torque levels are given in Table 3.1.

Table 3.1. Loosening torque levels

Case	Torque level (ft-lbs)
1	75
2	70
3	60
4	50
5	40
6	30
7	20
8	10

The measured on-nut impedances and their calculate RMSD are shown in Figure 3.8a. and Figure 3.8b, respectively.

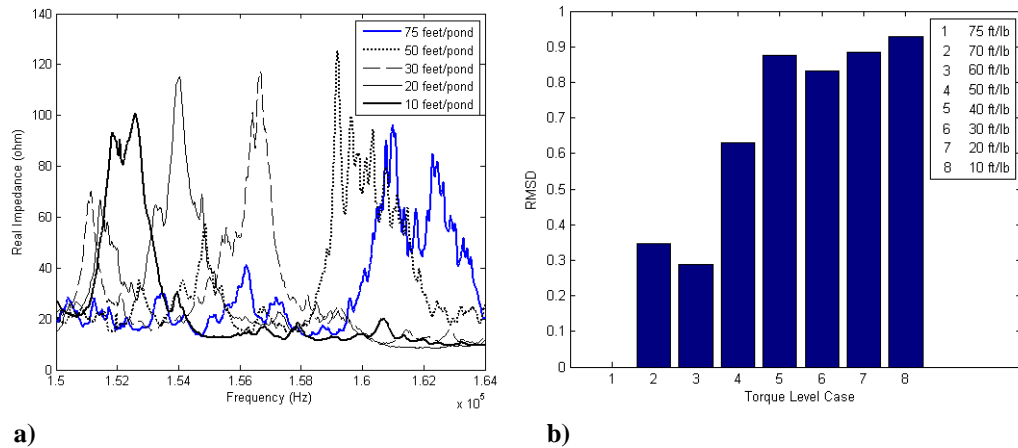


Figure 3.8. a) Impedance signature for different torque levels and b) their RMSD Damage metric

It is clearly observed from Figure 3.8b that the proposed damage detection method can unmistakably detect the damage when the assembly is loosened for 25 ft-lbs which corresponds to merely 2/3 of a bolt turn, having its RMSD metric way above the damage detection threshold. This should be considered as a key factor of this method as it definitely comes in very handy in the early detection of bolt loosening.

3.3.1.b. PZT Sensitivity

The abovementioned method of placing the PZT on the nut would clearly detect the bolt loosening. However, it hasn't yet been shown whether this method is capable of detecting which exact bolt, of different ones in the vicinity of each other, has been loosened. In order to verify this capability, the sensitivity of each PZT sensor, attached to a nut, to the loosening of its own bolt and to the loosening of its adjacent ones is examined in the following.

The RMSD damage metrics shown in Figure 3.9 are calculated for the impedance measured at each of the two PZTs A and B while bolt A was loosened for a quarter of a turn.

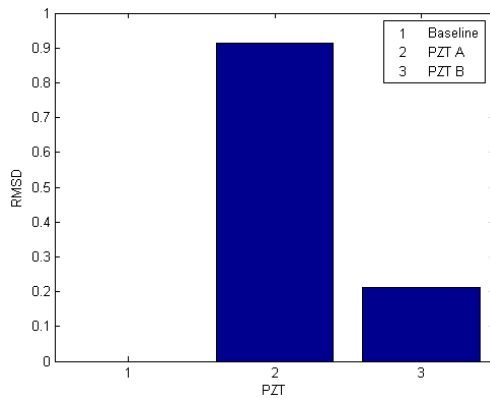


Figure 3.9. Damage metric investigating the PZT Sensitivity

The results in Figure 3.9 show that the RMSD of PZT B is close to the one of the retightened bolt in Figure 3.7b which was set as the bolt loosening threshold. In other words, PZT B is incapable of detecting damage (loosening) on bolt A. Thus only the PZT bonded to the awry bolt can detect its damage. This, therefore, affirms that the proposed damage detection method is capable of isolating the damage and exactly determining which bolt has been loosened.

3.3.1.c. Switch Bolt PZT Sensor Self-diagnostics

Integrated to the railroad switch's structure, PZT patches will be placed in a harsh environment, causing them to face breakage or bonding defects. Therefore, the structural health of these PZT sensors/actuators need to be monitored meanwhile monitoring the health of the host structure, i.e. the railroad switch. In the following experiment the

applicability of PZT sensor self-diagnostic procedure to the health monitoring of the railroad switch was examined.

Three samples were examined and their electrical impedances were measured over the frequency range of 10 kHz to 20 kHz. These three samples, as shown in Figure 3.10, were a free round PZT patch (healthy case), a broken on-nut PZT patch (broken case) and a semi de-bonded PZT from the nut (de-bonded case). After data processing of the measured electrical admittance, the plot of the imaginary part of the admittance versus frequency change was formed as shown in Figure 3.11.

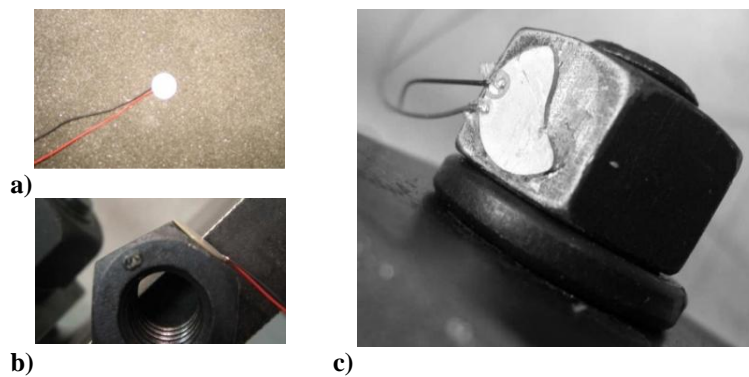


Figure 3.10. Snapshots of a) free PZT, b) partly bonded PZT patch, and c) a broken PZT patch

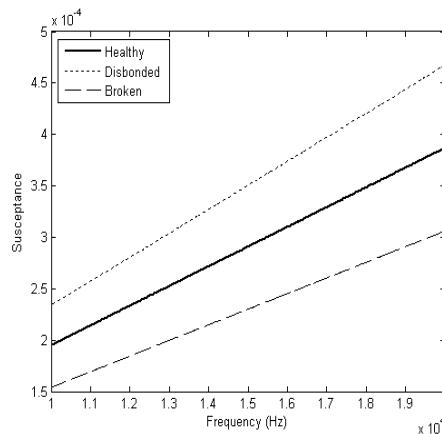


Figure 3.11. PZT susceptance-frequency line for different integrity conditions of the PZT patch

The acquired susceptance-frequency lines showed that the sensor breakage caused a downward shift in the slope of the line for the healthy case, while bonding defects induced an upward shift in the slope. These results verify that the impedance self-diagnostic technique can be integrated with the continuous monitoring of the railroad

switches and considering the harsh railroad environment, it appears to be an essential need.

3.4. Chapter Summary

The impedance-based structural health monitoring technique was applied in monitoring the loosening of bolted joints in a full-scale railroad switch. It was shown that a quarter of a turn of a bolt could be clearly detected by measuring the electrical impedance of a PZT patch at the bolted connection. The experimental results also showed that the proposed damage detection method could unmistakably detect the damage when the bolt assembly was loosened for 25 ft-lbs which corresponds to merely $1/10^{\text{th}}$ of a bolt turn, with the damage index value above the damage detection threshold assigned experimentally. This important result comes in very handy in the early detection of bolt loosening. It was then shown experimentally that having the PZT sensors/actuators attached to the bolts' nuts, each PZT would be much more sensitive to the damage on its own bolt than the neighboring bolts. This affirmed that the proposed damage detection method is capable of isolating the loosened bolt from the others.

COEFFICIENTS OF THERMAL EXPANSION AND THE ELASTIC CONSTANTS OF A BODY

One of the main objectives of the current thesis, as given in the next chapter, is to analytically model the effect of temperature variations on the vibratory response of beam structures. This is done by modifying the stress formulations inside the structure to include the effect of thermal loading and temperature fluctuations. Other than the thermal stress formulations, the effect of temperature variations on the material properties of the structure is considered as another parameter to be included in the modeling. In order to justify the inclusion of thermal effects from both points of view (i.e. material properties variations and generation of thermal stresses) and to verify that these two effects do not overlap, derivation and assumptions behind thermal stress formulations are investigated in the present chapter. First, the formulations of stresses inside a body are derived and the relevant assumptions are explained. A review of *thermoelasticity* and *theory of thermal stresses* along with the fundamental relations, equations and assumptions are then provided.

4.1. Stress Tensor Formulations

For a thermoelastic and homogeneous body going from the initial un-deformed state to the present deformed shape, the present values of the internal energy (e), entropy (η), heat flux (\mathbf{q}) and the stress tensor ($\tilde{\mathbf{T}}$) depend upon the present values of temperature (θ), deformation gradients (\mathbf{F}) and temperature gradients (\mathbf{g}) [15]. It is also known that the Helmholtz free energy (ϕ) is given by

$$\phi = e - \eta\theta \quad (4.1)$$

Therefore, the stress tensor and the Helmholtz free energy may be given as

$$\begin{aligned} \tilde{\mathbf{T}}(\mathbf{X}, t) &= \tilde{\mathbf{T}}(\mathbf{F}(\mathbf{X}, t), \theta(\mathbf{X}, t), \mathbf{g}(\mathbf{X}, t)) \\ \phi(\mathbf{X}, t) &= \phi(\mathbf{F}(\mathbf{X}, t), \theta(\mathbf{X}, t), \mathbf{g}(\mathbf{X}, t)) \end{aligned} \quad (4.2)$$

where \mathbf{X} is the coordinate in the un-deformed state and t is the time.

Applying the second law of thermodynamics of irreversible processes (which results in the Clausius-Duhem inequality for the referential description of motion of the body), it is shown that the Helmholtz free energy is independent of temperature gradients [15]. Knowing this independence and following the material objectivity (stating that a rigid body rotation does not affect the Helmholtz free energy), Helmholtz free energy may be rewritten as

$$\phi = \phi(\mathbf{E}, \theta) \quad (4.3)$$

where \mathbf{E} is the Green-St. Venant strain tensor. It is also shown from the Clausius-Duhem inequality that the stress tensor is related to the Helmholtz free energy as

$$\tilde{T}_{iL} = \rho_0 \frac{\partial \phi}{\partial F_{iL}} \quad (4.4)$$

Assuming the initial state of $\mathbf{E}_0 = \mathbf{0}$ and θ_0 and that the strain variations as well as the temperature variations are small, i.e. $|\mathbf{E}| \ll 1$ and $\left| \frac{\theta - \theta_0}{\theta_0} \right| \ll 1$, the free energy of Eq. (4.3) may be expressed, in terms of Taylor series expansion around the initial state of $\mathbf{E}_0 = \mathbf{0}$ and θ_0 and keeping only the terms up to the second order, as

$$\begin{aligned} \phi = \phi(\mathbf{E}, \theta) &= \phi(\mathbf{0}, \theta_0) + \left. \frac{\partial \phi}{\partial E_{LM}} \right|_{\text{Ref}} E_{LM} + \left. \frac{\partial \phi}{\partial \theta} \right|_{\text{Ref}} (\theta - \theta_0) + \\ &+ \left. \frac{1}{2} \frac{\partial^2 \phi}{\partial E_{LM} \partial E_{PQ}} \right|_{\text{Ref}} E_{LM} E_{PQ} + \left. \frac{\partial^2 \phi}{\partial E_{LM} \partial \theta} \right|_{\text{Ref}} E_{LM} (\theta - \theta_0) + \left. \frac{1}{2} \frac{\partial^2 \phi}{\partial \theta^2} \right|_{\text{Ref}} (\theta - \theta_0)^2 \end{aligned} \quad (4.5)$$

where the subscript of ‘‘Ref’’ refers to the value of the parameter at the reference configuration for the initial state.

Considering the stress tensor formulation as given in Eq. (4.4) and the second order approximation of the Helmholtz free energy as given in Eq. (4.5), the symmetric second Piola-Kirchoff stress tensor (S_{LM}) may be related to the Helmholtz free energy as [15]

$$S_{LM} = \rho_0 \frac{\partial \phi}{\partial E_{LM}} = S_{LM}^0 + C_{LMPQ} E_{PQ} + \alpha_{LM} (\theta - \theta_0) \quad (4.6)$$

where S_{LM}^0 is the second Piola-Kirchoff stress tensor at the reference configuration, C_{LMPQ} is the elastic constants of the body at the reference configuration and α_{LM} is the stress-temperature moduli. These three coefficients are formulated as

$$\begin{aligned} S_{LM}^0 &= \rho_0 \left. \frac{\partial \phi}{\partial E_{LM}} \right|_{\substack{\mathbf{E}_0 = \mathbf{0} \\ \theta_0 = 0}} \\ C_{LMPQ} &= \rho_0 \left. \frac{\partial^2 \phi}{\partial E_{LM} \partial E_{PQ}} \right|_{\substack{\mathbf{E}_0 = \mathbf{0} \\ \theta_0 = 0}} \\ \alpha_{LM} &= \rho_0 \left. \frac{\partial^2 \phi}{\partial E_{LM} \partial \theta} \right|_{\substack{\mathbf{E}_0 = \mathbf{0} \\ \theta_0 = 0}} \end{aligned} \quad (4.7)$$

In order to formulate the relation between the coefficient of thermal expansion, $\hat{\alpha}_{LM}$, and the stress-temperature moduli, α_{LM} , a free body (i.e. $\mathbf{S} = \mathbf{0}$) is considered to be uniformly heated from the reference temperature of θ_0 to the present temperature of θ . The displacements of this body is given by [15]

$$u_L = (\theta - \theta_0) \hat{\alpha}_{LM} X_M + c_M \quad (4.8)$$

where c_M is a constant vector. Therefore, by applying the displacement of Eq. (4.8) to the general formulation of the Green-St. Venant strain tensor ($E_{LM} = \frac{1}{2} (u_{A,B} + u_{B,A} + u_{i,A} u_{i,B})$) yields

$$E_{LM} = \frac{1}{2} [(\theta - \theta_0) (\hat{\alpha}_{LM} + \hat{\alpha}_{ML}) + (\theta - \theta_0)^2 \hat{\alpha}_{AL} \hat{\alpha}_{AM}] \quad (4.9)$$

Substituting Eq. (4.9) into Eq. (4.6) and assuming zero stress at the reference configuration, the three parameters of C_{LMPQ} , α_{LM} and $\hat{\alpha}_{LM}$ will be related as

$$\alpha_{LM} = -\frac{1}{2}C_{LMPQ}[(\hat{\alpha}_{PQ} + \hat{\alpha}_{QP}) + (\theta - \theta_0)\hat{\alpha}_{AP}\hat{\alpha}_{AQ}] \quad (4.10)$$

Assuming a symmetric tensor for the coefficients of thermal expansion, i.e. $\hat{\alpha}_{PQ} = \hat{\alpha}_{QP}$, and considering only the first order terms in Eq. (4.10), this equation will be simplified as

$$\alpha_{LM} = -C_{LMPQ}\hat{\alpha}_{PQ} \quad (4.11)$$

By substituting Eq. (4.11) into Eq. (4.6) and assuming a stress-free initial condition, the second Piola-Kirchoff stress tensor is simplified to

$$S_{LM} = C_{LMPQ}E_{PQ} + \alpha_{LM}(\theta - \theta_0) \quad (4.12)$$

It is important to note that the stress formulation of Eq. (4.12) is only valid if temperature variations as well as the strain variations are small with respect to the reference (initial) state of the body. Therefore, the material properties of C_{LMPQ} and α_{LM} are given for the initial state of the body. The small variations of strain and temperature imply that the variations of these material properties are negligible. If temperature variations are not small, however, Taylor series expansion of the Helmholtz free energy as given in Eq. (4.5) is not valid anymore. Assuming that the variations in the strain are small, which is a valid assumption for the applications studied in the next chapters, the Helmholtz free energy may be approximated, by applying Taylor series expansion around the initial state of zero strain, $\mathbf{E}_0 = \mathbf{0}$, and by keeping terms up to the second order of the strain, as

$$\begin{aligned} \phi = \phi(\mathbf{E}, \theta) &= \phi(\mathbf{0}, \theta) + \left. \frac{\partial \phi(\mathbf{E}, \theta)}{\partial E_{LM}} \right|_{\mathbf{E}_0=\mathbf{0}} E_{LM} + \frac{1}{2} \left. \frac{\partial^2 \phi(\mathbf{E}, \theta)}{\partial E_{LM} \partial E_{PQ}} \right|_{\mathbf{E}_0=\mathbf{0}} E_{LM} E_{PQ} \\ &= A_1(\theta) + B_{LM}(\theta)E_{LM} + D_{LMPQ}(\theta)E_{LM}E_{PQ} \end{aligned} \quad (4.13)$$

where

$$\begin{aligned}
A_1(\theta) &= \phi(\mathbf{0}, \theta) \\
B_{LM}(\theta) &= \left. \frac{\partial \phi(\mathbf{E}, \theta)}{\partial E_{LM}} \right|_{\mathbf{E}_0=\mathbf{0}} \\
G_{LMPQ}(\theta) &= \left. \frac{1}{2} \frac{\partial^2 \phi(\mathbf{E}, \theta)}{\partial E_{LM} \partial E_{PQ}} \right|_{\mathbf{E}_0=\mathbf{0}}
\end{aligned} \tag{4.14}$$

Therefore, the second Piola-Kirchhoff stress tensor may be formulated as

$$S_{LM} = S_{LM}^0(\theta) + D_{LMPQ}(\theta)E_{PQ} \tag{4.15}$$

where

$$\begin{aligned}
S_{LM}^0(\theta) &= \rho_0 \left. \frac{\partial \phi(\mathbf{E}, \theta)}{\partial E_{LM}} \right|_{\mathbf{E}_0=\mathbf{0}} \\
D_{LMPQ}(\theta) &= \rho_0 \left. \frac{\partial^2 \phi(\mathbf{E}, \theta)}{\partial E_{LM} \partial E_{PQ}} \right|_{\mathbf{E}_0=\mathbf{0}}
\end{aligned} \tag{4.16}$$

Comparing the two formulations of the second Piola-Kirchhoff stress tensor as given in Eqs. (4.12) for small variations in temperature and as given in Eq. (4.15) for large variations in temperature, shows that the effect of temperature on the stress formulation in a general case is seen from two parameters: 1) $S_{LM}^0(\theta)$ which is the amount of stress at the un-deformed state and at different temperature set points, and 2) $D_{LMPQ}(\theta)$ that may be simply formulated as

$$D_{LMPQ}(\theta) = \frac{\partial S_{LM}}{\partial E_{PQ}} \tag{4.17}$$

In other words $D_{LMPQ}(\theta)$ is the rate of change of stress with respect to the strain, which is the same as the elastic constants of the body at the reference configuration and at different temperature set points. For the initial temperature at the un-deformed shape and also for small temperature variations with non-varying material properties, this value is equal to the elastic constant of C_{LMPQ} given at the initial state. For the small temperature variations, $S_{LM}^0(\theta)$ could also be approximated (by Taylor series expansion around the initial temperature set point) as $\alpha_{LM}(\theta - \theta_0)$. For large temperature variations, however, such approximation would impose errors.

Based on the above-mentioned explanation, it is shown that the temperature variations affect the stress inside a body through affecting its temperature-dependent elastic coefficients (material properties) as well as through the thermal stress generation in the un-deformed state. This, therefore, results in the formulation of stress inside the body as

$$S_{LM} = \alpha_{LM}(\theta - \theta_0) + D_{LMPQ}(\theta)E_{PQ} \quad (4.18)$$

Therefore, considering the two effects of thermal stress and temperature-dependent material properties of a body as the two factors in studying the effect of temperature on a vibratory behavior of a structure is shown to be a valid assumption. It is important to note, however, that the stress formulation given in Eq. (4.18) includes an approximation due to the consideration of only the first order term in approximating $S_{LM}^0(\theta)$. This approximation needs to be justified depending on the application. In the analytical formulations given in the present and the following chapters, stress is formulated as given in Eq. (4.18).

4.1.1. The Effect of Temperature on the Material Properties

A practical example of the effect of temperature on the material properties is given in this section for the structures made of aluminum. Aluminum is one of the most commonly used metals for aircraft and will be used in the analytical and experimental studies in this thesis. The material properties of aluminum at various temperature set points have not been well studied in literature and there is a lack of experimental data with this regard. Moreover, the majority of such studies look at temperature variations at quite large steps (with steps of 20°C) for large overall ranges of temperature variations ((-273)-500°C). In our application, we are rather interested in smaller ranges of temperature variations with small increments. Due to the lack of available data, at this point the experimental results of available literature [102] are used in the present work and linear interpolation is assumed between the data points of material properties. Upon improvements in the temperature-material properties data, theoretical background related to modeling temperature-dependent material properties will also be modified.

Values of altering material properties of Young's modulus of elasticity (E) and shear modulus (G) with respect to temperature is given in Table 4.1 [102]. Having the two material properties of E and G , Poisson's ratio (ν) (also given in Table 4.1) may be calculated using the equation of $\nu = \frac{E}{2G} - 1$.

Table 4.1. Change in the material properties of aluminum with respect to temperature variations

Temperature °C	0	20	40	60	80	100	140	180	220
Young's Modulus, Mpsi (GPa)	10.17 (70.12)	10.07 (69.43)	9.96 (68.67)	9.84 (67.84)	9.73 (67.09)	9.61 (66.26)	9.38 (64.67)	9.14 (63.02)	8.90 (61.36)
Shear Modulus, Mpsi	3.81	3.77	3.73	3.69	3.65	3.60	3.52	3.43	3.35
Poisson's Ratio	0.334	0.335	0.335	0.335	0.334	0.334	0.333	0.332	0.330

Based on the values given in Table 4.1, it is noticed that the Young's modulus of elasticity varies more dominantly with respect to temperature (1.1% of variations in 20°C) as compared to the Poisson's ratio (0.05% variations in 20°C). Therefore, considering modulus of elasticity as the only temperature-dependent material property wouldn't cause a significant error in to the modeling. It is also noted that the Young's modulus varies linearly with respect to time, as shown in Figure 4.1.

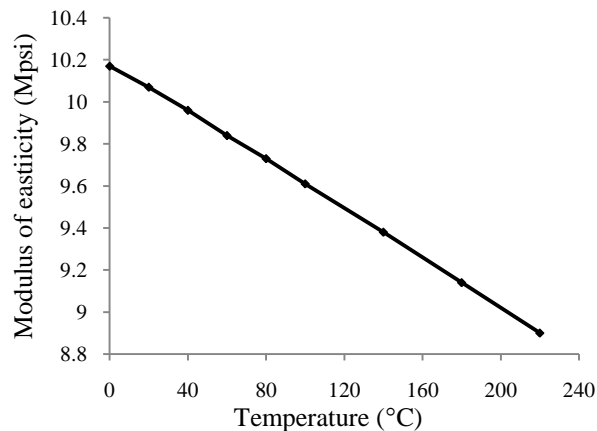


Figure 4.1. Variations of the Young's modulus of aluminum with respect to temperature

Therefore, a linear formulation of the modulus of elasticity as a function of temperature can be considered as

$$E(\theta) = E_i + \frac{dE}{d\theta}(\theta - \theta_i) \quad (4.19)$$

where E_i is the modulus of elasticity at the reference temperature of θ_i .

The mass density of the material per unit area (ρ) is also temperature dependent due to the dimensional expansions of the structure with respect to the increasing temperature. Due to the small value of thermal expansion coefficient of aluminum (22.2×10^{-6} m/m per °C, 12.3×10^{-6} in/in °F) and the small size of the structures studied in this thesis, change in the dimensions, and hence the mass density of these structures is neglected here without imposing a significant error.

4.2. Fundamental Differential Equations of Thermoelasticity

Derivation of the differential equations used in thermoelasticity given here in this section are based on the assumption that the Helmholtz free energy of the body is approximated by applying the second order Taylor series in the vicinity of the initial undeformed state (for strain and temperature) as [77]

$$\phi(\boldsymbol{\varepsilon}, \theta) = \frac{1}{2} c_{ijkl} \varepsilon_{ij} \varepsilon_{kl} - \beta_{ij} \varepsilon_{ij} \mathcal{T} - \frac{1}{2} m \mathcal{T}^2 \quad (4.20)$$

where

$$\begin{aligned} c_{ijkl} &= \left(\frac{\partial \sigma_{ij}}{\partial \varepsilon_{kl}} \right)_{\mathcal{T}} = \rho_0 \frac{\partial^2 \phi(0, \theta_0)}{\partial \varepsilon_{ij} \partial \varepsilon_{kl}} \\ \beta_{ij} &= - \left(\frac{\partial \sigma_{ij}}{\partial \theta} \right)_{\varepsilon} = -\rho_0 \frac{\partial^2 \phi(0, \theta_0)}{\partial \varepsilon_{ij} \partial \theta} \\ m &= -\rho_0 \frac{\partial^2 \phi(0, \theta_0)}{\partial \theta^2} \\ \mathcal{T} &= \theta - \theta_0 \end{aligned} \quad (4.21)$$

and ε_{ij} and σ_{ij} are the strain and stress tensors. It has also been assumed that the free energy of the un-deformed state and its first derivatives with respect to temperature and strain vanish. Considering an isotropic material, the free energy of the body may be simplified as

$$\phi(\boldsymbol{\varepsilon}, \theta) = \mu \varepsilon_{ij} \varepsilon_{ij} + \frac{1}{2} \lambda \varepsilon_{kk} \varepsilon_{mm} - \gamma \varepsilon_{kk} \mathcal{T} - \frac{1}{2} m \mathcal{T}^2 \quad (4.22)$$

where μ and λ are Lamé constants of a homogeneous body. Knowing that the stresses and the entropy are related to the Helmholtz free energy as

$$\begin{aligned} \sigma_{ij} &= \frac{\partial \phi}{\partial \varepsilon_{ij}} \\ S &= \frac{\partial \phi}{\partial \theta} \end{aligned} \quad (4.23)$$

and by considering the coefficient of (thermal) linear volume expansion (α_t) related to γ as $\gamma = 3K\alpha_t$ (with $K = \lambda + \frac{2}{3}\mu$), the stresses and the entropy are formulated as

$$\begin{aligned} \sigma_{ij} &= 2\mu \varepsilon_{ij} + (\lambda \varepsilon_{kk} - \gamma \mathcal{T}) \delta_{ij} \\ S &= \gamma \varepsilon_{kk} + c_\varepsilon \log \left(1 + \frac{\mathcal{T}}{\theta_0} \right) \end{aligned} \quad (4.24)$$

where c_ε is the specific heat at constant strain and is equal to $c_\varepsilon = \theta \left(\frac{\partial S}{\partial \theta} \right)_\varepsilon = m\theta_0$. Considering the assumption that the temperature variations are small compared to the initial state temperature, i.e. $\left| \frac{\mathcal{T}}{\theta_0} \right| \ll 1$, the entropy may be further simplified as

$$S = \gamma \varepsilon_{kk} + \frac{c_\varepsilon}{\theta_0} \mathcal{T} \quad (4.25)$$

Considering the Fourier law of heat conduction, i.e. $q_i = -\lambda_0 \theta_{,i}$ with $\lambda_0 > 0$ being the material thermal conductivity of an isotropic material, the entropy balance for this material is presented as [77]

$$\theta \dot{S} = \lambda_0 \mathcal{J}_{,ii} + W \quad (4.26)$$

where q_i is the heat flux vector, W is the heat generated, the indicial notation $[\]_{,i} = \frac{\partial [\]}{\partial x_i}$ with x_i being the coordinates on the present configuration and $\dot{S} = \frac{\partial S}{\partial t}$. Substituting the entropy given in Eq. (4.25) into Eq. (4.26) yields

$$\left(\nabla^2 - \frac{1}{\kappa} \frac{\partial}{\partial t}\right) \mathcal{T} - \zeta \dot{\varepsilon}_{kk} = -\frac{Q}{\kappa} \quad (4.27)$$

where $\zeta = \frac{\gamma \theta_0}{\lambda_0}$, $Q = \frac{\kappa W}{\lambda_0}$ and $\kappa = \frac{\lambda_0}{c_\varepsilon}$. If the temperature variations are not small then Eq. (4.27) is modified to a non-linear form as

$$\mathcal{T}_{,ii} - \frac{1}{\kappa} \dot{\mathcal{T}} - \zeta \dot{\varepsilon}_{kk} - \frac{\zeta}{\theta_0} \mathcal{T} \dot{\varepsilon}_{kk} = -\frac{W}{\lambda_0} \quad (4.28)$$

The general equation of motion of a body is given as [77]

$$\sigma_{ij,j} + \chi_i = \rho_0 \ddot{u}_i \quad (4.29)$$

where χ_i is the body forces vector and u_i is the displacement vector. Considering the linear strain-displacement relationship of $\varepsilon_{ij} = \frac{1}{2}(u_{i,j} + u_{j,i})$ and substituting the stress formulation of Eq. (4.24) into Eq. (4.29) yields

$$\mu u_{i,jj} + (\lambda + \mu) u_{j,ji} + \chi_i = \gamma \mathcal{T}_{,i} + \rho_0 \ddot{u}_i \quad (4.30)$$

Therefore, Eqs. (4.27) and (4.30) form the coupled set of equations for temperature and displacement relations used in thermoelasticity which are rewritten together as [77]

$$\begin{aligned} \mu u_{i,jj} + (\lambda + \mu) u_{j,ji} + \chi_i &= \gamma \mathcal{T}_{,i} + \rho_0 \ddot{u}_i \\ \left(\nabla^2 - \frac{1}{\kappa} \frac{\partial}{\partial t}\right) \mathcal{T} - \zeta \dot{\varepsilon}_{kk} &= -\frac{Q}{\kappa} \end{aligned} \quad (4.31)$$

There exist different temperature and displacement boundary conditions, depending on the problem, that complete the set of differential equations of Eq. (4.31). Some of these temperature boundary conditions are as:

- a. the prescribed temperature on the bounding surface area of the body
- b. the given temperature gradient on the bounding surface of the body; This boundary condition corresponds to a known flow of heat through the surface. If the temperature gradient is zero, it describes a thermal insulation over the surface.
- c. the heat exchange over the surface having the format of a known function

Differential equations of Eq. (4.31) also require initial conditions. The initial conditions need to be of the following form for the temperature and displacement and the first derivative of displacement with respect to time at the natural state of the body

$$\begin{aligned}\mathcal{T}(\mathbf{x}, 0) &= f_1(\mathbf{x}) \\ u_i(\mathbf{x}, 0) &= g_1(\mathbf{x}) \\ \dot{u}_i(\mathbf{x}, 0) &= g_2(\mathbf{x})\end{aligned}\tag{4.32}$$

4.2.1. Heat Conduction Happening Very Slowly (Adiabatic Process)

Assuming that the heat conduction causes a really slow heat exchange between different parts of the body, then it is safe to assume that each part is thermally insulated and the process is adiabatic (i.e. no heat is transferred to or from the body). Therefore, there exist no heat sources to the body and the surface of the body is thermally insulated and the coupled set of equations of Eq. (4.31) may be simplified as [77]

$$\begin{aligned}\mu u_{i,jj} + (\lambda + \mu)u_{j,ji} + \chi_i &= \gamma \mathcal{T}_{,i} + \rho_0 \ddot{u}_i \\ \mathcal{T}_{,jj} - \frac{1}{\kappa} \dot{\mathcal{T}} - \zeta \dot{e} &= 0\end{aligned}\tag{4.33}$$

where $e = \varepsilon_{kk}$ is the dilatation. Having $S = \text{constant}$ or $\dot{S} = 0$ for an adiabatic process, temperature distribution may be formulated as

$$\mathcal{T} = -\zeta_{\mathcal{T}} \kappa e\tag{4.34}$$

where $\zeta_{\mathcal{T}} = \frac{\gamma_{\mathcal{T}} \theta_0}{c_{\varepsilon} \kappa}$ and $\gamma_{\mathcal{T}} = (3\lambda_{\mathcal{T}} + 2\mu_{\mathcal{T}})\alpha_t$. Eq. (4.34) shows that for an adiabatic process, temperature inside the body is proportional to the dilatation. Substituting this equation into the equation of motion of Eq. (4.30) yields

$$\mu_{\mathcal{T}} u_{i,jj} + (\lambda_{\mathcal{T}} + \mu_{\mathcal{T}} + \kappa \zeta_{\mathcal{T}} \gamma_{\mathcal{T}}) u_{j,ji} + \chi_i = \rho_0 \ddot{u}_i\tag{4.35}$$

where $\gamma_{\mathcal{T}}$, $\mu_{\mathcal{T}}$ and $\lambda_{\mathcal{T}}$ are constants at temperature \mathcal{T} .

4.3. Fundamental Differential Equations of Theory of Thermal Stresses

Let's rewrite the set of differential equations given in Eq. (4.31) here

$$\begin{aligned}\mu u_{i,jj} + (\lambda + \mu)u_{j,ji} + \chi_i &= \gamma \mathcal{T}_i + \rho_0 \ddot{u}_i \\ \left(\nabla^2 - \frac{1}{\kappa} \frac{\partial}{\partial t}\right) \mathcal{T} - \zeta \dot{\epsilon}_{kk} &= -\frac{Q}{\kappa}\end{aligned}$$

Solving these equations in their coupled state makes the solution rather complicated. It has been shown that the effect of neglecting the coupling term of $\zeta \dot{\epsilon}_{kk}$ on the values of displacement and temperature is negligible [77]. Neglecting this term will uncouple the two equations as

$$\begin{aligned}\mu u_{i,jj} + (\lambda + \mu)u_{j,ji} + \chi_i &= \gamma \mathcal{T}_i + \rho_0 \ddot{u}_i \\ \left(\nabla^2 - \frac{1}{\kappa} \frac{\partial}{\partial t}\right) \mathcal{T} &= -\frac{Q}{\kappa}\end{aligned}\tag{4.36}$$

and temperature may be found from the second equation and put into the first equation as a known term in solving the first equation for the displacement. Another example of this problem is when the function of temperature variation is assumed to be known as a prescribed function and is substituted to the first equation of Eq. (4.31), and is solved for the unknown displacements. Neglecting the coupling term of $\zeta \dot{\epsilon}_{kk}$ and considering the un-coupled set of differential equations as given in Eq. (4.36) form the basis of the theory of thermal stresses. This theory will be applied in the analytical modeling presented in the rest of this thesis.

4.4. Chapter Summary

The effect of temperature variations on the vibratory response of structures is modeled by considering the two effects of temperature-dependent material properties and thermal stress formations inside the structure. The inclusion of thermal effects from both of these points of view (i.e. material properties variations and generation of thermal stresses) was justified in this chapter. By studying the assumptions considered in deriving thermal stress formulations it was verified in the present chapter that these two effects of

thermal fluctuations do not overlap (are not dependent). Thus considering the two effects of thermal stress and temperature-dependent material properties of a body as the two factors in studying the effect of temperature on a vibratory behavior of a structure was shown to be a valid assumption.

It was shown that to formulate the stresses inside a body for small temperature variations, the Helmholtz free energy may be approximated around the initial state (of zero strain and initial temperature set point) of the body using the second order Taylor series expansion. The elastic moduli of the body were assumed to be non-varying for this case. For large temperature changes, however, it was shown that the free energy could be approximated by applying Taylor series expansion around the initial state of zero strain, $\mathbf{E}_0 = \mathbf{0}$, and by keeping terms up to the second order of the strain. The elastic moduli of the body (the material properties) were also shown to be varying as a function of the fluctuating temperature. The final formulation of the stresses inside a body for large temperature variations was derived and was shown to include an approximation which needs to be justified depending on the application. This form of the stress formulation will be used in the analytical studies given in this thesis.

The effect of temperature on different material properties of aluminum was described as a special example. It was shown that the Young's modulus of elasticity of aluminum varies more dominantly with respect to temperature (1.1% of variations in 20°C) as compared to the Poisson's ratio (0.05% variations in 20°C). It was also noted that the Young's modulus varies linearly with respect to time.

THE EFFECT OF A SINGLE CRACK ON THE VIBRATORY CHARACTERISTICS OF EULER- BERNOULLI BEAMS

In this chapter, the vibratory response of an Euler-Bernoulli beam with two different support conditions of simply supported (on both ends) and clamped (on both ends) is studied. The beam is assumed to have a single, non-breathing crack on one side and is assumed to be under thermal loading and temperature variations. In the first part of the modeling, free vibrations of the cracked beam without considering the effect of temperature fluctuations is studied and the mode shapes of the cracked beam are formulated using two different approaches. The effect of temperature variations on the mode shapes of free vibrations of the cracked beam are then studied considering two effects of temperature-dependent material properties and induced thermal stresses inside the beam. Temperature distribution inside the beam is assumed to be steady state initially. In the last part of the modeling, the cracked beam is considered to have a surface-bonded layer of piezoelectric (PZT) sensor and the effect of the general case of temperature distributions inside the beam is studied along with the effect of damage growth. Each of the abovementioned scenarios for an Euler-Bernoulli beam with different crack locations and severity and various temperature variations scenarios is then numerically studied. Summary and concluding remarks are given at the end of the chapter.

5.1. Background Review on Modeling the Effect of Crack and Temperature Variations on the Vibration Response of a Structure

To date, there have been numerous approaches to modeling damage, in particular cracks, in beam-like structures [6; 76; 7; 44; 85]. A crack changes the mode shapes and reduces the resonance frequency of the beam as it changes the local stiffness of the beam at the location of the crack. Initiation and growth of single or multiple cracks in a beam, therefore, may be monitored by studying the variations in the beam's resonant frequency and mode shapes. Therefore, analytical modeling of the relation between the resonance frequency of the beam and different parameters of location and severity of the crack would be helpful in SHM applications. One of the first papers on the analytical modeling of the effect of a crack presence on the vibration-based response of a beam used the Rayleigh-Ritz approximation by modifying the stress distribution in the Euler-Bernoulli beam [31]. In this modeling, the stress field near a pair of symmetric cracks was assumed to be maximum at the place of the crack and decay experimentally with distance from the crack. The function of stress distribution in the vicinity of the crack includes a parameter that is found experimentally. Presence and growth of a crack in a vibrating beam was also modeled as the resultant reduction in the stiffness of the beam at the place of the crack. Freund *et al* (1976) formulated this resultant stiffness by applying fracture mechanics formulations, stress intensity factor and the elastic deformation energy [48]. This form of modeling the crack in a beam was later combined with various beam formulations in order to analytically study the vibration-based response and mode shapes of a cracked beam. Chondros *et al* used the resultant stiffness crack modeling and applied the Hu-Washizu-Barr variational formulations in formulating the vibration-based response of a beam with a single-edge crack [29; 30]. Ostachowicz *et al* (1991) applied the resultant crack stiffness formulation and modeled the crack as a massless rotational spring [78]. They were among the first to model the cracked beam as a bi-section, connected at the crack location with a torsional spring. Compatibility conditions are applied at the crack location to formulate the mode shapes of the cracked beam. Their studies were limited to the numerical analysis of a cantilever beam with multiple, single-edged cracks. The concept of crack modeling as a massless rotational spring connecting the two sections of

the beam was later used in different references for various support conditions, number of cracks and loading of the beam. These studies were initially done numerically for Euler-Bernoulli and Timoshenko beams with single or multiple cracks. Later, closed-form expressions of the mode shapes and resonant frequencies of vibrating cracked beam were formulated for different boundary conditions and crack specifications [59; 45; 68; 10]. This form of modeling of the vibrations and mode shapes of a cracked beam has also been applied to the identification (i.e. determining the location and size) of a crack in a vibrating beam. Closed-form expressions of the location and severity of the crack were provided for different support conditions of the beam [75; 51; 37]. The early works on the vibration-based response of a cracked beam assume a non-breathing crack in order to avoid non-linear terms and complexity added to the modeling of the structure. In recent years, however, more work has been focused on the effect of the opening and closing of the crack on the vibration response of a cracked beam [28; 91].

The theory of thermal stresses is originally summarized by Boley and Wiener (1960), Nowacki (1975) and modernized with applications by Hetnarski and Eslami (2008). Thermoelastic vibrations of beams and plates without cracking or layered piezoceramic materials are known and well studied [20; 56; 54; 27; 72]. Detailed analytical results are available studying thermal effects on vibration for various boundary conditions and different plate shapes and for linear and non-linear models. These studies look at the coupling between temperature and strain fields. The temperature influence on material properties of these structures, however, has been ignored in modeling temperature-induced variations of dynamic responses. One of the only studies of the changes in vibratory response of a system due to temperature variations in the structure shows, through sensitivity analysis, that the natural frequencies of a vibrating plate are dominated by temperature-induced variations in the material's Young's modulus. However, through comparison between analytical and experimental results, it is shown that the effect of variation in the material properties only accounts for part of natural frequency shift when the boundaries of a structure are completely restrained [112; 111]. Similarly Afshari, et al., (2009) showed that temperature-induced shifts in natural frequency become larger in beams as the structure becomes more constrained. Thus boundary conditions are another important factor in modeling and considerations of

thermal effects on the dynamic characteristics of different material structures. It is important to note that no previous research available in literature considers both the effects of temperature-induced material properties *and* thermoelastic coupling.

Despite the fact that each of the two problems of thermoelastic vibrations and vibration-based crack detection are analytically well studied in the literature, analytical considerations of temperature variation effects on the accuracy of monitoring the presence and growth of a crack has not been undertaken. Several case studies present extensive studies of thermal effects on the health monitoring of civil infrastructures illustrating the importance of considering thermal effects on real life, in situ applications of health monitoring methods. However, due to the complexity of civil structures, the effect of temperature on the health monitoring has only been studied experimentally. In addition, finite element models have been constructed for empirical studies [99; 43; 84; 12]. Different detection algorithms have been proposed in these references in order to better extract damage and temperature related effects on vibratory characteristics of structures from experimentally collected data.

5.2. Theory and Modeling

The beam studied here is assumed to be a uniform Euler-Bernoulli beam having a single fatigue crack at a distance of x_c from the beginning of the beam. The beam is assumed to have length L , width b , thickness h_b and a uniform cross section along the beam. The beam is studied at two different support conditions of fixed-fixed and simply supported on both ends. The transverse displacement of the beam in y -direction depends on the position along the length of the beam, x , and time and is denoted as $v(x, t)$.

For simplicity in the modeling, the fatigue crack is assumed to be non-breathing during the deformations of the beam. The crack is treated as a localized reduction in the stiffness and modeled as a massless rotational spring at the location of the crack. The beam is then considered to be of bisections connected by this spring, as shown in Figure 5.1.

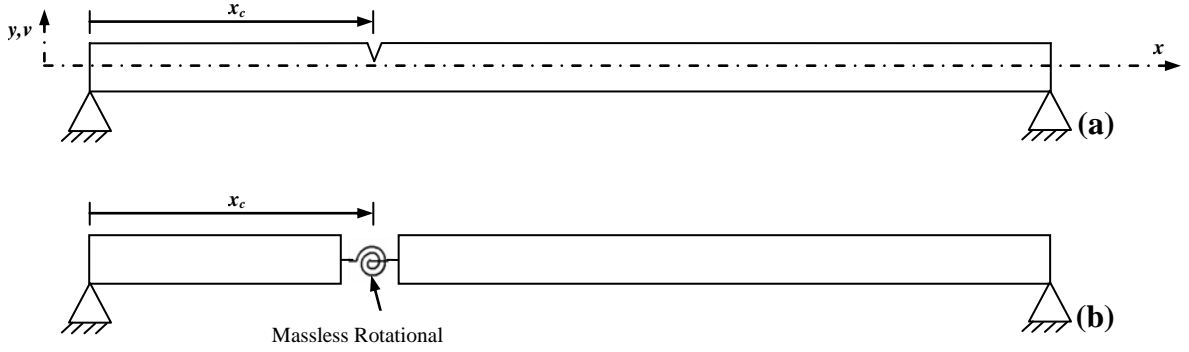


Figure 5.1. Beam a) with a single fatigue crack, b) with a single fatigue crack treated as a massless rotational spring

5.2.1. Modeling the Presence of Damage in the Form of a Crack

Presence of the damage in the form of a part-through-the-depth crack that is along the whole width of the beam is most commonly modeled as a local reduction in the stiffness of the beam in the form of a massless rotational spring connecting the two parts of the cracked beam, as shown in Figure 5.1. The compliance and the stiffness of the resultant rotational spring are formulated from the strain energy and fracture mechanics formulations, as explained in the following. It is assumed that the beam of Figure 5.1 has a single crack of depth a_c and is under bending moments as shown in Figure 5.2.

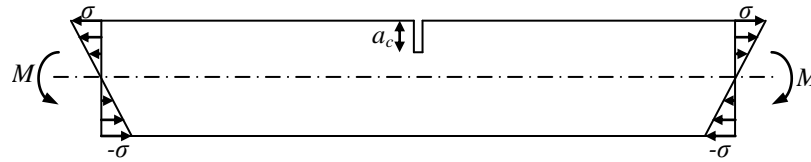


Figure 5.2. Beam with a single crack under pure bending

The stress intensity factor for a beam under pure bending is formulated as [103]

$$K = \sigma \sqrt{\pi a_c} F(a_c/h_b) \quad (5.1)$$

where $F(a_c/h_b)$ for $a_c/h_b \leq 0.6$, with 0.2% accuracy is [103]

$$F(a_c/h_b) = 1.122 - 1.40(a_c/h_b) + 7.33(a_c/h_b)^2 - 13.08(a_c/h_b)^3 + \quad (5.2)$$

$$14.0(a_c/h_b)^4$$

and the stress σ for a beam with rectangular cross section and the bending moment of M is formulated as [16]

$$\sigma = \frac{Mc}{I} = \frac{Mh_b/2}{bh_b^3/12} = \frac{6M}{bh_b^2} \quad (5.3)$$

The total strain energy of elastic deformation in a solid having a crack is given as

$$U_T = \int_{A_c} \mathcal{G} dA_c \quad (5.4)$$

where \mathcal{G} is the elastic energy available per unit increase in crack surface area. For plane stress conditions \mathcal{G} is calculated as [103]

$$\mathcal{G} = \frac{K^2}{E_b} \quad (5.5)$$

Substituting Eqs. (5.1), (5.3) and (4.2) into Eq. (5.4) and having $dA_c = bda$ results as

$$U_T = b \int_0^{a_c} \frac{K^2}{E_b} da = \frac{3M^2\pi h_b}{E_b I h_b} \int_0^{a_c} \frac{a}{h_b} F^2(a/h_b) da \quad (5.6)$$

The total strain energy may be simply formulated as

$$U_T = \frac{3\pi h_b M^2}{E_b I} \Psi(a_c/h_b) \quad (5.7)$$

where

$$\begin{aligned} \Psi(a_c/h_b) = & 0.629(a_c/h_b)^2 - 1.047(a_c/h_b)^3 + 4.602(a_c/h_b)^4 \\ & - 9.975(a_c/h_b)^5 + 20.295(a_c/h_b)^6 - 32.993(a_c/h_b)^7 \\ & + 47.041(a_c/h_b)^8 - 40.693(a_c/h_b)^9 + 19.6(a_c/h_b)^{10} \end{aligned} \quad (5.8)$$

Applying the Castigliano's theorem, the rotation corresponding to the applied moment, M , will be formulated as [30]

$$\phi = \frac{\partial U_T}{\partial M} = \frac{6\pi h_b M}{E_b I} \Psi(a_c/h_b) \quad (5.9)$$

Knowing that the compliance of the crack is given as the ratio of the rotation to the applied moment, it will be formulated as

$$C_c = \frac{1}{k_c} = \frac{\phi}{M} = \frac{6h_b\pi}{E_b I} \Psi(a_c/h_b) \quad (5.10)$$

where k_c is the stiffness at the place of the crack.

5.2.1.a.Mode shapes of a cracked beam

One of the most commonly used modeling of a cracked beam is to model the crack as a massless rotational spring that connects the two sections of the beam. The stiffness of the beam at the place of the crack (the stiffness of the resultant rotational spring) is approximated as described in section 5.2.1 and given in Eq. (5.10). Closed-form expressions of the mode shapes and resonant frequencies of vibrating cracked beam are then formulated by considering the beam's support conditions and the compatibility conditions at the place of the crack. This type of modeling, referred to as the exact model, is initially introduced in the following section. Later, Rayleigh-Ritz approximation is applied to proposing an approximate formulation of the mode shapes of the cracked beam. In the proposed formulation, the crack is modeled in a similar fashion (as a massless rotational spring) and the presence of the crack is included in the modeling by formulating the amount of energy an un-cracked beam loses due to the crack-resultant added rotation.

5.2.1.a.I. Exact modeling

The equation of motion of the free vibrations of the Euler-Bernoulli beam of Figure 5.1 is

$$(E_b I) \frac{\partial^4 v(x,t)}{\partial x^4} + (\rho_b A) \frac{\partial^2 v(x,t)}{\partial t^2} = 0 \quad (5.11)$$

where $v(x, t)$ is the transverse deflection of the vibrating beam and $E_b I$ and $\rho_b A$ are the flexural rigidity and mass per unit length of the beam, respectively. Applying the

separation of variables to the transverse deflection of the vibrating beam, the solution may be written as

$$v(x, t) = \sum_{j=1}^k X^j(x) e^{i\omega_j t} \quad (5.12)$$

where $X^i(x)$ is the i -th mode shape of the vibrating beam with the resonant frequency of ω_j . Substituting Eq. (5.12) into Eq. (5.11) the following spatial differential equation will be obtained

$$X^i{}'''' - \gamma_i^4 X^i = 0 \quad (5.13)$$

where $\gamma_i^4 = \frac{\rho_b A \omega_i^2}{E_b I}$. A general solution to Eq. (5.13) is

$$X^i(x) = \sum_{j=1}^4 D_j^i S_j^i(x) \quad (5.14)$$

where D_j^i 's are constants determined from the beam's boundary conditions and $S_j^i(x)$'s are the following linearly independent fundamental solutions

$$\begin{aligned} S_1^i(x) &= \frac{1}{2} \cos(\gamma_i x) + \frac{1}{2} \cosh(\gamma_i x) \\ S_2^i(x) &= \frac{1}{2\gamma_i} \sin(\gamma_i x) + \frac{1}{2\gamma_i} \sinh(\gamma_i x) \\ S_3^i(x) &= -\frac{1}{2\gamma_i^2} \cos(\gamma_i x) + \frac{1}{2\gamma_i^2} \cosh(\gamma_i x) \\ S_4^i(x) &= -\frac{1}{2\gamma_i^3} \sin(\gamma_i x) + \frac{1}{2\gamma_i^3} \sinh(\gamma_i x) \end{aligned} \quad (5.15)$$

This form of normalized formulation of $S_j^i(x)$ results in the following simplified relations at the origin

$$\begin{pmatrix} S_1^i(0) & S_1^{i'}(0) & S_1^{i''}(0) & S_1^{i'''}(0) \\ S_2^i(0) & S_2^{i'}(0) & S_2^{i''}(0) & S_2^{i'''}(0) \\ S_3^i(0) & S_3^{i'}(0) & S_3^{i''}(0) & S_3^{i'''}(0) \\ S_4^i(0) & S_4^{i'}(0) & S_4^{i''}(0) & S_4^{i'''}(0) \end{pmatrix} = \begin{pmatrix} 1 & 0 & 0 & 0 \\ 0 & 1 & 0 & 0 \\ 0 & 0 & 1 & 0 \\ 0 & 0 & 0 & 1 \end{pmatrix} \quad (5.16)$$

As mentioned earlier in this chapter, the cracked beam of Figure 5.1 is modeled as a bi-sectional beam connected at the place of the crack with the massless rotational spring

with the compliance formulated in Eq. (5.10). The compatibility conditions require the force and displacement on both sides of the crack to be equal. For the beam of Figure 5.1 having a single crack, these conditions may be expressed as

$$\begin{aligned} X_2^i(x_c) &= X_1^i(x_c), \\ M_2^i(x_c) &= M_1^i(x_c), \\ V_2^i(x_c) &= V_1^i(x_c), \\ X_2^{i'}(x_c) &= X_1^{i'}(x_c) + E_b I C_c X_1^{i''}(x_c), \end{aligned} \quad (5.17)$$

where $X_1^i(x)$ and $X_2^i(x)$ are the mode shapes of the i -th mode of the free vibrations of the first ($0 < x \leq x_c$) and the second ($x_c < x \leq L$) segment of the bi-sectional beam and $M^i(x)$, and $V^i(x)$ are the moment and shearing force of the i -th mode, respectively. Applying the compatibility conditions at the place of the crack, the i -th mode shapes of the free vibrations of a cracked beam, are formulated as

$$X^i(x) = X_1^i(x) + C_E X_1^{i''}(x_c) S_2^i(x - x_c) H(x - x_c), \quad 0 \leq x \leq L \quad (5.18)$$

where $H(x)$ is the Heaviside function and the $X_1^i(x)$ function is formulated by applying the support conditions at $x = 0$ to Eq. (5.14). This function is given for the simply-supported and clamped-clamped beam as

$$\text{Simply-Supported:} \quad X_1^i(x) = D_2^i S_2^i(x) + D_4^i S_4^i(x), \quad 0 \leq x < x_c \quad (5.19)$$

$$\text{Clamped-Clamped:} \quad X_1^i(x) = D_3^i S_3^i(x) + D_4^i S_4^i(x), \quad 0 \leq x < x_c$$

where $C_E = E_b I C_c$. Applying the boundary conditions at the end of the beam ($x = L$) to the mode shapes of Eq. (5.18) and factoring the unknown constants of D_2^i , D_3^i and D_4^i , results in the following matrix formulations

$$\begin{bmatrix} a_1^i & b_1^i \\ a_2^i & b_2^i \end{bmatrix} \begin{bmatrix} D_2^i \\ D_4^i \end{bmatrix} = \begin{bmatrix} 0 \\ 0 \end{bmatrix} \quad (5.20)$$

$$\begin{bmatrix} m_1^i & n_1^i \\ m_2^i & n_2^i \end{bmatrix} \begin{bmatrix} D_3^i \\ D_4^i \end{bmatrix} = \begin{bmatrix} 0 \\ 0 \end{bmatrix} \quad (5.21)$$

where a_1^i , b_1^i , a_2^i and b_2^i and m_1^i , n_1^i , m_2^i and n_2^i are

$$\begin{cases} a_1^i = S_2^i(L) + C_E S_2^{i''}(x_c) S_2^i(L - x_c) \\ b_1^i = S_4^i(L) + C_E S_4^{i''}(x_c) S_2^i(L - x_c) \\ a_2^i = S_2^{i''}(L) + C_E S_2^{i''}(x_c) S_2^{i''}(L - x_c) \\ b_2^i = S_4^{i''}(L) + C_E S_4^{i''}(x_c) S_2^{i''}(L - x_c) \end{cases} \quad (5.22)$$

$$\begin{cases} m_1^i = S_3^i(L) + C_E S_3^{i''}(x_c) S_2^i(L - x_c) \\ n_1^i = S_4^i(L) + C_E S_4^{i''}(x_c) S_2^i(L - x_c) \\ m_2^i = S_3^{i''}(L) + C_E S_3^{i''}(x_c) S_2^{i''}(L - x_c) \\ n_2^i = S_4^{i''}(L) + C_E S_4^{i''}(x_c) S_2^{i''}(L - x_c) \end{cases} \quad (5.23)$$

By setting the determinant of the coefficient matrices equal to zero, the characteristic equations will be formulated. In other words, the characteristic equations for a cracked simply-supported and a cracked fixed-fixed beam are given, respectively, as

$$a_1^i b_2^i = a_2^i b_1^i \quad (5.24)$$

$$m_1^i n_2^i = m_2^i n_1^i \quad (5.25)$$

This modeling approach is practical and has been used by many researchers for an Euler-Bernoulli or Timoshenko beam with a uniform cross section and different boundary conditions. It provides the closed form formulations of the mode shapes of the beam as the crack grows and is attractive when the variations in the resonant frequency of the beam due to the presence and growth of the crack are of interest in SHM practices.

5.2.1.a.II. Approximate modeling of the cracked beam using Rayleigh-Ritz method

Formulating the closed-form solutions is not possible for most of problems and satisfying all boundary conditions is not straightforward for complex structures. Rayleigh-Ritz is a helpful method in approximating the mode shapes and resonant frequencies of structural and mechanical systems. In this method, similar to the assumed modes technique, the mode shapes of the structure are approximated by a finite series consisting of known functions (trial functions) multiplied by unknown coefficients (Ritz coefficients/generalized coordinates). Therefore a partial differential equation is

converted to a set of ordinary differential equations. The trial functions need to be differentiable and satisfy at least the geometric boundary conditions (these functions are called the *admissible functions*). Formulating and using trial functions that satisfy natural boundary conditions as well the geometric boundary conditions results in better approximations of the structure (these trial functions satisfying both geometric and natural boundary conditions are called the *comparison functions*).

Rayleigh-Ritz method, as mentioned earlier, is only an approximation technique and is a helpful method in formulating the upper bound of the fundamental frequencies of the mechanical structures. Minimizing the Rayleigh's quotient (formulated by equating the maximum potential and kinetic energies) with respect to the unknown Ritz coefficients results in forming an algebraic eigenvalue problem instead of a differential one. The fundamental frequencies, Ritz coefficients and the mode shapes of the structure are then approximated by forming the solution of this eigenvalue problem.

One of the important factors in the convergence of the Rayleigh-Ritz approximation, as mentioned earlier, is the choice of trial functions, especially for the case where discontinuities, such as damage, are present in the structure. This method is of interest as it will be applied in integrating the two effects of temperature variations and crack presence.

Considering only the effect of crack initiation and growth in the beam (and assuming that the temperature remains unchanged), different trial functions may be considered in approximating the resonant frequency of a cracked beam using Rayleigh-Ritz method. A simple approach, introduced in the present work, is to model the cracked beam as an un-cracked beam that loses energy due to the crack-resultant added rotation at the place of the crack. In the Rayleigh-Ritz method, mode shapes of the vibrating beam are approximated as

$$X^{(k)}(x) = \sum_{i=1}^n c_i^{(k)} \phi^i(x) \quad (5.26)$$

where $c_i^{(k)}$'s are unknown, constant Ritz coefficients and $\phi^i(x)$'s are the admissible functions, satisfying boundary conditions. As given earlier in Eq. (5.12) the transverse deflection of the k -th mode of vibration of the beam is given using the assumed mode method as

$$v^{(k)}(x, t) = X^{(k)}(x)e^{i\omega_k t} \quad (5.27)$$

where $\omega^{(k)}$ is the k -th mode resonant frequency of the beam. The admissible functions used here, for approximating the mode shapes of the cracked beam shown in Figure 5.1, are the i -th mode shapes of an un-cracked beam with the appropriate boundary conditions, given for simply supported and fixed-fixed boundary conditions as
Simply Supported:

$$\begin{aligned} \phi^i(x) &= D_i \sin \zeta_i x \\ \zeta_i &= \frac{i\pi}{L}, \quad i = 1, 2, \dots, n \end{aligned} \quad (5.28)$$

Fixed-Fixed:

$$\begin{aligned} \phi^i(x) &= D_i \left[(\cos \zeta_i x - \cosh \zeta_i x) - \frac{\cos \zeta_i L - \cosh \zeta_i L}{\sin \zeta_i L - \sinh \zeta_i L} (\sin \zeta_i x - \sinh \zeta_i x) \right] \\ \cos \zeta_i L \cosh \zeta_i L &= 1, \quad i = 1, 2, \dots, n \end{aligned} \quad (5.29)$$

In the proposed approximation, the crack is still assumed to be treated as a massless rotational spring with the resultant compliance as given earlier in Eq. (5.10). When using the mode shapes of the un-cracked beam as the admissible functions for Rayleigh-Ritz approximation, the maximum strain energy needs to be modified to account for the loss of energy due to the presence of the crack. This energy loss is proportional to the amount of the added flexibility due to the presence of crack/rotational-spring. This may be quantified as the added rotation of the spring for the k -th mode of vibrations, $\Delta\Phi^{(k)}$, given by

$$\Delta\Phi^{(k)} = C_c M^{(k)}(x_c, t) = -C_E \frac{\partial^2 v^{(k)}}{\partial x^2}(x_c, t) \quad (5.30)$$

where $M^{(k)}(x_c, t)$ is the bending moment of the k -th mode of vibrations of the un-cracked beam at the place of the crack and is equivalent to $M^{(k)}(x_c, t) = -E_b I \frac{\partial^2 v^{(k)}}{\partial x^2}(x_c, t)$. By substituting Eq. (5.27) into Eq. (5.30) the added rotation may be simply given as

$$\Delta\Phi^{(k)} = -C_E X^{(k)''}(x_c) e^{i\omega_k t} \quad (5.31)$$

The maximum potential energy related to the added rotation of $\Delta\Phi^{(k)}$ will then be

$$U_{\text{crack}}^{(k)} = \frac{1}{2} (\Delta\Phi^{(k)}) M^{(k)} = \frac{1}{2} E_b I C_E \left[X^{(k)''}(x_c) \right]^2 \quad (5.32)$$

This energy is proportional to the added compliance due to the presence of the crack and the added rotation, so it needs to be subtracted from the energy of the un-cracked beam in order to formulate the modified stiffness and mass matrices of Rayleigh-Ritz approximation.

For an Euler-Bernoulli beam with a uniform cross section, the strain and kinetic energies of the k -th mode of the beam without considering the effect of presence of the crack are given as

$$\begin{aligned} \pi_b^{(k)} &= \frac{1}{2} \iiint_{V_{\text{beam}}} \sigma_{xx}^{b(k)} \varepsilon_{xx}^{b(k)} dV_{\text{beam}} = \frac{1}{2} \int_0^L E_b I \left(\frac{\partial^2 v^{(k)}}{\partial x^2} \right)^2 dx \\ T_b^{(k)} &= \frac{1}{2} \iiint_{V_{\text{beam}}} \rho_b \left(\frac{\partial v^{(k)}}{\partial t} \right)^2 dV_{\text{beam}} = \frac{1}{2} \int_0^L \rho h_b b \left(\frac{\partial v^{(k)}}{\partial t} \right)^2 dx \end{aligned} \quad (5.33)$$

By substituting Eq. (5.27) into Eq. (5.33) the maximum values of these two energies may be simply given as

$$\begin{aligned} \pi_b^{(k)} &= \frac{1}{2} \int_0^L E_b I \left[X^{(k)''}(x) \right]^2 dx \\ T_b^{(k)} &= \frac{1}{2} (\omega_k)^2 \int_0^L \rho h_b b \left[X^{(k)}(x) \right]^2 dx \end{aligned} \quad (5.34)$$

By considering the presence of the crack, the maximum total strain and kinetic energies of the cracked beam may be written as

$$\begin{aligned} \pi_{\text{max}}^{(k)} &= \frac{1}{2} \int_0^L E_b I \left[X^{(k)''}(x) \right]^2 dx - \frac{1}{2} E_b I C_E \left[X^{(k)''}(x_c) \right]^2 \\ T_{\text{max}}^{(k)} &= \frac{1}{2} (\omega_k)^2 \int_0^L \rho h_b b \left[X^{(k)}(x) \right]^2 dx \end{aligned} \quad (5.35)$$

Substituting the Rayleigh-Ritz approximation of Eq. (5.26) into Eq. (5.35), these two energies may be expressed as

$$\begin{aligned}\pi_{\max}^{(k)} &= \frac{1}{2} \mathbf{c}^{(k)T} \mathbf{k}^{(1)} \mathbf{c}^{(k)} \\ T_{\max}^{(k)} &= \frac{1}{2} (\omega_k)^2 \mathbf{c}^{(k)T} \mathbf{m}^{(1)} \mathbf{c}^{(k)}\end{aligned}\quad (5.36)$$

Applying the mode shapes as formulated in Eq. (5.76) to the maximum kinetic and strain energies results in forming the Rayleigh's quotient as

$$R^{(k)}(c_1^k, \dots, c_N^k) = \omega_k^2 = \frac{\pi_{\max}^{(k)}}{T_{\max}^{*(k)}} \quad (5.37)$$

where

$$T_{\max}^{*(k)} = \frac{1}{2} \rho h_b b \int_0^L [X^{(k)}(x)]^2 dx \quad (5.38)$$

Ritz coefficients of c_i^k are found by minimizing Rayleigh's quotient of Eq. (5.37) with respect to c_j^k [90]

$$\frac{\partial R^{(k)}}{\partial c_j^k} = 0 \quad (5.39)$$

Differentiating Eq. (5.37) with respect to c_j^k gives

$$\frac{\partial R^{(k)}}{\partial c_j^k} = \frac{1}{T_{\max}^{*(k)}} \left[\frac{\partial \pi_{\max}^{(k)}}{\partial c_j^k} - \omega_k^2 \frac{\partial T_{\max}^{*(k)}}{\partial c_j^k} \right] \quad (5.40)$$

Applying the derivatives of Eq. (5.40) to Eq. (5.36), the problem will be reduced to finding eigenvalues and eigenvectors of the following matrix equation

$$[\mathbf{k}^{(1)} - (\omega_k)^2 \mathbf{m}^{(1)}] \mathbf{c}^{(k)} = \mathbf{0} \quad (5.41)$$

where $\mathbf{c}^{(k)} = \{c_1^{(k)}, c_2^{(k)}, \dots, c_n^{(k)}\}^T$ is the vector of Ritz coefficients. The modified stiffness and mass matrices for the transverse vibrations of the cracked beam are formulated as

$$\begin{aligned}
k_{ij}^{(1)} &= E_b I \int_0^L \phi^{i''}(x) \phi^{j''}(x) dx - E_b I C_E [\phi^{i''}(x_c)] [\phi^{j''}(x_c)] \\
m_{ij}^{(1)} &= \rho h_b b \int_0^L \phi^i(x) \phi^j(x) dx
\end{aligned} \tag{5.42}$$

which include the effect of the presence of a growing crack. Once $\mathbf{c}^{(k)}$ vector is found from Eq. (5.41), it will be substituted into Eq. (5.26) and mode shapes of the cracked beam, $X^{(k)}(x)$, will be approximated.

The proposed approximation method is beneficial as there is no need for formulating the mode shapes of the cracked beam as given in the reference modeling approach. The only crack-related parameter needed is its compliance, C_c , which is easily formulated as Eq. (5.10) as a function of size of the crack. It will be shown later in the numerical results section that applying the proposed approximation will not impose a significant error to the calculated resonant frequencies of the cracked beam compared to the those formulated by the exact modeling of the cracked beam as given in section 5.2.1.a.I. In other words, the proposed modeling effort provides a close approximation of the mode shapes of a cracked beam without any further closed-form formulations of the mode shapes of the beam as given in the exact modeling of section 5.2.1.a.I.

Another approach to the approximation of the mode shapes of a cracked beam that results in more accurate formulations of the resonance frequencies of the beam is to model the cracked beam as a bisection connected with the massless rotational spring at the place of the crack, as shown in Figure 5.1. The presence of the crack is included in this formulation in two parts: 1) the trial functions used in the Rayleigh-Ritz approximation for the two sections of the beam are modified so that they satisfy the compatibility conditions at the place of the crack and 2) the energy stored in the crack modeled as a rotational spring needs to be added to the total strain energy [46; 94]. The resonant frequencies of the cracked beam are found by solving the following eigenvalue problem (similar to Eq. (5.41))

$$[\mathbf{k}^{(2)} - (\omega_k)^2 \mathbf{m}^{(2)}] \mathbf{d}^{(k)} = \mathbf{0} \tag{5.43}$$

where $\mathbf{d}^{(k)} = \{d_1^{(k)}, d_2^{(k)}, \dots, d_n^{(k)}\}^T$ is the vector of Ritz coefficients and the stiffness and mass matrices of $\mathbf{k}^{(2)}$ and $\mathbf{m}^{(2)}$, respectively, are formulated as

$$\begin{aligned}
k_{ij}^{(2)} &= \int_0^{x_c} E_b I \varphi_1^{i''}(x) \varphi_1^{j''}(x) dx + \int_{x_c}^L E_b I \varphi_2^{i''}(x) \varphi_2^{j''}(x) dx \\
&\quad + \frac{1}{2} E_b I C_E \varphi_1^{i''}(x_c) \varphi_1^{j''}(x_c) \\
m_{ij}^{(2)} &= \int_0^{x_c} \rho h_b b \varphi_1^{i''}(x) \varphi_1^{j''}(x) dx + \int_{x_c}^L \rho h_b b \varphi_2^{i''}(x) \varphi_2^{j''}(x) dx \\
&\quad \varphi_1^i(x); 0 \leq x \leq x_c, \quad \varphi_2^i(x); x_c < x \leq L
\end{aligned} \tag{5.44}$$

where $\varphi_1^i(x)$ and $\varphi_2^i(x)$ are the trial functions on the two sections of the cracked beam. The mode shapes of the vibrating beam are formulated by applying the Rayleigh-Ritz approximation as

$$X^{(k)}(x) = \sum_{i=1}^n d_i^{(k)} \varphi^i(x) \tag{5.45}$$

where $\varphi^i(x)$ is given as a function of the trial functions of the two sections of the beam as

$$\varphi^i(x) = \varphi_1^i(x) + H(x - x_c) \varphi_2^i(x) \tag{5.46}$$

where $H(x)$ is the Heaviside function. These trial functions are formulated by modifying the exact mode shapes of the free vibrations of an un-cracked beam by adding linear terms of x variable in order to satisfy the support conditions of the un-cracked beam as well as satisfy the compatibility conditions of Eq. (5.17) at the place of the crack. For a beam simply supported on both ends these functions are given as [94]

$$\begin{aligned}
\varphi_1^i(x) &= \sin\left(i\pi \frac{x}{L}\right) - (i\pi)^2 \eta \sin\left(i\pi \frac{x_c}{L}\right) \left(1 - \frac{x_c}{L}\right) x \\
\varphi_2^i(x) &= \sin\left(i\pi \frac{x}{L}\right) - (i\pi)^2 \eta \sin\left(i\pi \frac{x_c}{L}\right) (1 - x) \frac{x_c}{L}
\end{aligned} \tag{5.47}$$

where η is the crack sensitivity and defined as [94]

$$\eta = \frac{h_b}{L} m\left(\frac{a_c}{h_b}\right) \tag{5.48}$$

with $m(\alpha) = 2 \left(\frac{\alpha}{1-\alpha}\right)^2 (5.93 - 19.69\alpha + 34.14\alpha^2 - 35.84\alpha^3 + 13.2\alpha^4)$. It is shown that this approach results in very accurate approximations of the first four resonant

frequencies of a simply supported Euler-Bernoulli beam compared to the exact formulations [94].

It is important to note that when modeling the beam as a bi-section, presence of the crack as a massless rotational spring is seen at the boundaries of the system. Therefore, the energy of presence of the crack, U_{crack} , will be added to the total energy of the two sections of the beam before and after the crack. On the other hand, the crack presence formulated in Eqs. (5.35)-(5.41) is seen as a loss in the amount of potential energy of the un-cracked beam and hence U_{crack} (the energy of the crack due to the added rotation) is subtracted from the un-cracked beam's strain energy.

With the mode shapes of the free vibrations of the cracked beam being formulated, the effect of temperature variations on the cracked beam's vibratory response is studied in the following. The effect of temperature variations is first studied from the material's point of view and the general thermal stress formulations inside the beam are given. Then both effects of damage growth and temperature variations are studied together for the vibrations of the Euler-Bernoulli beam.

5.2.2. Modeling the Effect of Temperature Variations

Change in the temperature distribution inside the beam, $T(x, y, z, t)$, affects the vibratory characteristics of this system through alterations of material properties, like modulus of elasticity, as well as causing thermal stresses inside the beam, as studied earlier in chapter 4. It also changes the dimensions of the beam through material expansion. In the study presented here, the later effect is assumed to be negligible compared to the effects on the material properties and thermal stresses and, therefore, have not been considered in the present modeling.

Temperature alteration might happen in different forms of ambient temperature variation, applying a uniform heat flux or many other forms. One of the motivations of considering the effect of temperature variation is to investigate and to quantify how temperature variations affect the health monitoring results and how it can be compensated for. In most of the health monitoring applications, continuous measurement of the resonant characteristics of the system is not required and only a limited number of scheduled measurements would suffice. Therefore, temperature variation may be

considered as steady-state. This, in most cases, may be simplified as a uniform, time-independent temperature distribution inside the beam. Hence, the sole effect of temperature variations on the vibration characteristics of the system will be seen through the change in the material properties. In some special cases, like spacecraft and aircraft, the effect of temperature may be modeled as a constant heat flux. Temperature variation will happen only through the depth of the specimen and will be homogeneous along the length, i.e. $T(y, t)$. In these cases, a temperature effect on the vibratory response of the system will be caused through alterations in the material properties as well as thermal stress generation inside the system.

The effect of temperature variations on the material properties of aluminum was studied in section 4.1.1. In the following section, this effect will be studied regarding the resonant frequency changes it causes for a vibrating aluminum beam with different support conditions and dimensions. Later, the general thermal stress formulation inside a beam is provided.

5.2.2.a. The effect of variations in the temperature-dependent material properties on the resonant frequencies of an Euler-Bernoulli beam

Variations in the material properties of aluminum with respect to temperature changes were given earlier in Table 4.1. It was also shown that considering the modulus of elasticity of aluminum as the only temperature dependent material property wouldn't cause any significant error in the modeling. For the temperature varied from 0°C (32°F) to 220°C (428°F), the first natural frequency of an aluminum beam is calculated here that results from the varying modulus of elasticity in this range of temperature as given in Table 4.1. Temperature-dependent shift in the frequency is tabulated for an Euler-Bernoulli beam of length 9.45", width 0.75" and thickness 0.18", made of aluminum (mass density of 168.56 lb/ft³(2700 kg/m³)) in Table 5.1. These frequencies are calculated based on simple vibrations modeling of an Euler-Bernoulli beam, considering only the first mode of vibrations.

Table 5.1. Shift in the first natural frequency of an aluminum beam due to the temperature-varying modulus of elasticity for different boundary conditions

Boundary Condition	Cantilever	Pinned-Pinned	Clamped-Pinned	Clamped-Clamped
Frequency Shift (Hz/°C)	0.0188	0.0529	0.0828	0.1199

Based on the theoretical values of Table 5.1, the effect of temperature variation will be much more significant when both ends of the beam are fixed and the structure is restrained. These results show that with only about 5°C change in the temperature, the first natural frequency of a fixed beam may change for more than 0.5 Hz. This shift of frequency is equal to the presence of a crack of size 0.5 mm if the temperature is assumed to be non-varying [7]. These preliminary results are good indications of the effect of temperature-dependent material properties on the resonant frequency of a beam. The experimental results for a cantilever beam of the above-mentioned properties show slight variation of beam's natural frequency of the first mode with respect to the temperature variations. This result shows 0.0213 Hz/°C of frequency shift for a vibrating cantilever beam [7]. This drop in the resonant frequency of the first mode will be enhanced if both ends of the beam are pinned or clamped. This effect will be more extensively studied in the next sections.

It is important to note that the drop in the natural frequency of a beam due to the change in temperature depends on the value of the resonant frequency of the beam. In other words, the higher the resonance frequency of the beam, the more the shift due to temperature and material properties variation. As an example, for a beam with the same material properties listed earlier and with different length, width and thickness of 12", 1" and 0.125", the effect of modulus of elasticity variation of Table 4.1 on the resonant frequency is as listed in Table 5.2

Table 5.2. Shift in the first natural frequency of an aluminum beam of length, width and thickness of 12", 1" and 0.125", respectively

Boundary Condition	Cantilever	Pinned-Pinned	Clamped-Pinned	Clamped-Clamped
Frequency Shift (Hz/°C)	0.008	0.023	0.036	0.053

The results of Table 5.2 show that the change in the resonant frequency of the latter beam is less than the shorter beam. This is due to the fact that the natural frequency of the 12" long cantilever beam at 20°C is equal to 28 Hz, as compared to the one for the 9.45" long cantilever beam at the same temperature which is 64 Hz. Therefore, the larger the natural frequency of the structure, the more effective will temperature variations be on the health monitoring response of the system. This is another emphasis on the importance of considering temperature effects on the vibratory characteristics of real life structures, like civil infrastructures.

5.2.2.b. Thermal stresses inside a beam

As mentioned earlier in section 4.3, theory of *thermal stresses* studies the effect of heat on the deformations of a body. It applies classical heat conduction equations to formulate temperature variations inside the body. Once the temperature distribution is known, deformations of the body are formulated, neglecting their coupling to the heat production. In other words, in theory of thermal stresses it is assumed that the effect of deformations on temperature field is negligible and the function of temperature distribution inside the body is known. Considering the theory of thermal stresses and applying the Euler-Bernoulli assumptions and the linear strain-displacement relation, the axial stress inside the beam of Figure 5.1 considering the effect of thermal stress for the plane-stress condition is formulated as [20]

$$\sigma_{xx}^b = E_b(T)(\varepsilon_{xx}^b - \alpha_t T) \quad (5.49)$$

where α_t and $E_b(T)$ are the coefficient of thermal expansion and modulus of elasticity of the beam, respectively. For simplicity, the modulus of elasticity will be denoted as E_b in the formulations here. The strain inside an Euler-Bernoulli beam, ε_{xx}^b , is related to the coordinates and the lateral displacement of $v(x, t)$ of the beam as [20]

$$\varepsilon_{xx}^b = -y \frac{\partial^2 v(x, t)}{\partial x^2} \quad (5.50)$$

It is important to note that both values of the coefficient of thermal expansion and the modulus of elasticity of the beam are functions of temperature inside the beam. However,

variations of α_t with respect to temperature are assumed to be negligible here. It is also important to note that $T(x, y, z, t)$ considered here is the amount of change in temperature compared to the initial temperature inside the structure.

In the following two sections, the effect of temperature variations on the vibratory characteristics of an Euler-Bernoulli is studied along with the effect of a growing damage. In the first section, the effect of steady-state temperature variations is analyzed for the free vibrations of the beam and the variations in the resonant frequencies of the beam are studied. In the second section, the effect of general temperature variations on the vibrations of the cracked beam is studied considering different modeling parameters.

5.2.3. Modeling the Two Effects of Damage Growth and Steady-State Temperature Variations in the Formulations of Mode Shapes and Resonant Frequencies of Free Vibrations of a Cracked Euler-Bernoulli Beam

In order to include both effects of damage growth and temperature variations in the formulations of the mode shapes and resonant frequencies of a cracked beam, Rayleigh-Ritz approximation is applied here. Rayleigh-Ritz approximation is applied in formulating the strain and potential energies of the cracked beam. The maximum strain energy used in the Rayleigh-Ritz approximation is modified by adding the energy stored in the crack-resultant rotational spring. In order to have a better approximation of the effect of temperature variations on the resonant frequencies of the vibrating cracked beam, the trial functions are chosen to be the mode shapes of the two sections of the beam as formulating using the exact method given in section 5.2.1.a.I and Eq. (5.18). Temperature variations considered in the formulations given in this section are assumed to be steady-state (time-independent).

The axial stress inside an Euler-Bernoulli beam in the presence of temperature variations was formulated in Eq. (5.49). The temperature-dependent modulus of elasticity of the beam is simply denoted as E_b in the rest of this section. Considering a cross section of the beam as shown in Figure 5.3, the resultant bending moment, M_x^b , and axial force, N_x^b , may be related to the axial stress as

$$\begin{aligned}
M_x^b &= \iint_A \sigma_{xx}^b y dA = \int_{-b/2}^{b/2} \int_{-h_b/2}^{h_b/2} \sigma_{xx}^b y dy dz \\
N_x^b &= \iint_A \sigma_{xx}^b dA = \int_{-b/2}^{b/2} \int_{-h_b/2}^{h_b/2} \sigma_{xx}^b dy dz
\end{aligned}
\tag{5.51}$$

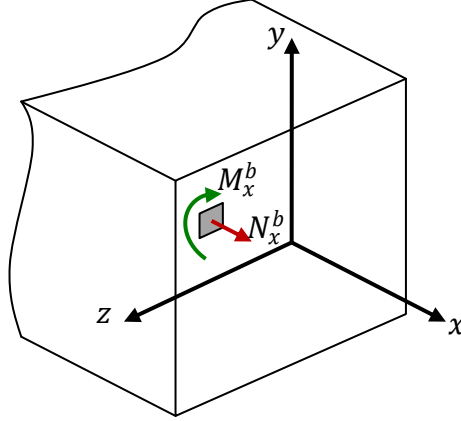


Figure 5.3. Force and moment diagram of the cross section of a beam

Substituting the stress as given in Eq. (5.49) into Eq. (5.51), the bending moment and axial force in the presence of temperature variations will be formulated as

$$\begin{aligned}
M_x^b &= -E_b I_z \frac{\partial^2 v(x,t)}{\partial x^2} - M_{T_z} \\
N_x^b &= -P_T
\end{aligned}
\tag{5.52}$$

where $I_z = \frac{1}{12} b h_b^3$ and

$$\begin{aligned}
P_T(x, t) &= \int_A \alpha_t E_b T(x, y, z, t) dA \\
M_{T_z}(x, t) &= \int_A \alpha_t E_b T(x, y, z, t) y dA \\
M_{T_y}(x, t) &= \int_A \alpha_t E_b T(x, y, z, t) z dA
\end{aligned}
\tag{5.53}$$

For the rest of formulations, I_z will be simply denoted as I . The formulations of thermal force and stresses as given in Eq. (5.53) are given for the general temperature distribution. For the steady-state case as considered in this section, however, the thermal moments and force will only be a function of the x -coordinate, if temperature depends on this coordinate.

The mode shapes and resonant frequencies of the cracked beam under temperature variations are approximated using the Rayleigh-Ritz method. The cracked beam is modeled as a bisection connected with the massless rotational spring at the place of the crack, as shown in Figure 5.1. The presence of the crack is included in this formulation in two parts: **i)** the trial functions used in the Rayleigh-Ritz approximation for the two sections of the beam are the mode shapes of free vibrations of the cracked beam in the absence of temperature variations as formulated earlier in section 5.2.1.a.I and Eq. (5.18), and **ii)** the energy stored in the crack modeled as a rotational spring is added to the total strain energy. The effect of temperature variations is also included in this formulation in two parts: **a)** the effect of temperature variations on the material properties of the beam (here only the modulus of elasticity) and on the equivalent compliance of the crack, and **b)** the effect of thermal stresses on the total energy stored at the crack-resultant rotational spring.

The strain and kinetic energies of the vibrations of the cracked bi-sectional Euler-Bernoulli beam without considering the energy stored in the crack-resultant spring is formulated as

$$\begin{aligned}\pi_b &= \frac{1}{2} \iiint_V \sigma_{xx}^b \varepsilon_{xx}^b dV \\ T_b &= \frac{1}{2} \iiint_V \rho_b \left(\frac{\partial v}{\partial t} \right)^2 dV\end{aligned}\tag{5.54}$$

Substituting the stress as formulated in Eq. (5.49) into Eq. (5.54), the strain and kinetic energies of the two sections of the cracked beam may be given as

$$\begin{aligned}\pi_b &= \frac{1}{2} \int_0^L E_b I \left(\frac{\partial^2 v}{\partial x^2} \right)^2 dx + \frac{1}{2} \int_0^L M_{T_z}(x) \frac{\partial^2 v}{\partial x^2} dx \\ T_b &= \frac{1}{2} \int_0^L \rho h_b b \left(\frac{\partial v}{\partial t} \right)^2 dx\end{aligned}\tag{5.55}$$

For simplicity, $M_{T_z}(x)$ will be denoted as M_{T_z} in the rest of formulations provided in this section.

The total strain energy of the cracked beam needs to be modified by adding the energy stored in the cracked beam. This energy is proportional to the amount of the added

flexibility due to the presence of crack/rotational-spring as given in Eq. (5.32) and reformatted here as

$$U_{\text{crack}} = \left[\frac{1}{2} (\Delta\Phi)M \right]_{x=x_c} = \frac{1}{2} C_c (M|_{x=x_c})^2 \quad (5.56)$$

where $M|_{x=x_c}$ is the bending moment of the un-cracked beam at the place of the crack and is equal to $M_x^b(x_c)$ as given in Eq. (5.52). The total energy stored in the crack is formulated by substituting Eq. (5.52) into Eq. (5.56) and given as

$$U_{\text{crack}} = \frac{1}{2} C_E E_b I \left(\frac{\partial^2 v}{\partial x^2} \Big|_{x=x_c} \right)^2 + \frac{1}{2} C_E M_{T_z} \frac{\partial^2 v}{\partial x^2} \Big|_{x=x_c} + \frac{1}{2} C_c (M_{T_z})^2 \quad (5.57)$$

The last term of Eq. (5.57) is independent of the lateral deflection and won't be included in the rest of the formulations.

The modified total strain and kinetic energies of the cracked beam will then be given as

$$\begin{aligned} \pi &= \frac{1}{2} \int_0^L \left[E_b I \left(\frac{\partial^2 v}{\partial x^2} \right)^2 + M_{T_z} \frac{\partial^2 v}{\partial x^2} \right] dx \\ &+ \frac{1}{2} C_E E_b I \left(\frac{\partial^2 v}{\partial x^2} \Big|_{x=x_c} \right)^2 + \frac{1}{2} C_E \left(M_{T_z} \frac{\partial^2 v}{\partial x^2} \Big|_{x=x_c} \right) \\ T &= \frac{1}{2} \int_0^L \rho h_b b \left(\frac{\partial v}{\partial t} \right)^2 dx \end{aligned} \quad (5.58)$$

By applying the separation of variables of Eq. (5.12), transverse deflection of the vibrating beam is formulated as $v(x, t) = \sum_{k=1}^N X^{(k)}(x) e^{i\omega_k t}$. According to the Rayleigh-Ritz method, mode shapes of the vibrating cracked beam under temperature variations are approximated as

$$X^{(k)}(x) = \sum_{i=1}^n g_i^{(k)} \psi^i(x) \quad (5.59)$$

where $g_i^{(k)}$'s are unknown, constant Ritz coefficients and $\psi^i(x)$'s are the admissible functions. Here, these functions are considered to be the mode shapes of the free vibrations of the cracked beam in the absence of temperature variations as formulated earlier and given in Eq. (5.18). Considering the modulus of elasticity of the beam as a

function of temperature gradient of $T(x, y, z, t)$ and simply denoted by $E_b(T)$, these mode shapes for the two sections of the beam may be rewritten as

$$\psi_2^i(x) = \begin{cases} \psi_1^i(x), & 0 \leq x \leq x_c \\ \psi_1^i(x) + C_E \psi_1^{i''}(x_c) S_2^i(x - x_c), & x_c \leq x \leq L \end{cases} \quad (5.60)$$

where $H(x)$ is the Heaviside function and the $\psi_1^i(x)$ function is formulated for the simply-supported and clamped-clamped beam as

$$\begin{aligned} \text{Simply-Supported: } \quad \psi_1^i(x) &= D_2^i S_2^i(x) + D_4^i S_4^i(x), \quad 0 \leq x < x_c \\ \text{Clamped-Clamped: } \quad \psi_1^i(x) &= D_3^i S_3^i(x) + D_4^i S_4^i(x), \quad 0 \leq x < x_c \end{aligned} \quad (5.61)$$

where D_2^i , D_3^i and D_4^i are constants. These mode shapes form the trial functions in the following Rayleigh-Ritz formulations.

By applying the assumed mode formulation of Eq. (5.12), the maximum total strain and kinetic energies of the cracked beam in the presence of thermal loading will be given as

$$\begin{aligned} \pi_{\max}^{(k)} &= \frac{1}{2} \int_0^L \left\{ E_b I \left[X^{(k)''}(x) \right]^2 + M_{T_z} X^{(k)''}(x) \right\} dx \\ &\quad + \frac{1}{2} C_E E_b I \left(X^{(k)''}(x_c) \right)^2 + \frac{1}{2} C_E M_{T_z}(x_c) X^{(k)''}(x_c) \\ T_{\max}^{(k)} &= \frac{1}{2} \rho h_b b \omega_k^2 \int_0^L \left[X^{(k)}(x) \right]^2 dx \end{aligned} \quad (5.62)$$

Substituting the mode shapes as formulated in Eq. (5.59) into these maximum kinetic and strain energies given in Eq. (5.62) results in forming the Rayleigh's quotient as

$$R^{(k)}(g_1^k, \dots, g_N^k) = \omega_k^2 = \frac{\pi_{\max}^{(k)}}{T_{\max}^{*(k)}} \quad (5.63)$$

where

$$T_{\max}^{*(k)} = \frac{1}{2} \rho h_b b \int_0^L \left[X^{(k)}(x) \right]^2 dx \quad (5.64)$$

Ritz coefficients of g_i^k are found by minimizing Rayleigh's quotient of Eq. (5.63) with respect to g_s^k [90]

$$\frac{\partial R^{(k)}}{\partial g_s^k} = 0 \quad (5.65)$$

Differentiating Eq. (5.63) with respect to g_s^k gives

$$\frac{\partial R^{(k)}}{\partial g_s^k} = \frac{1}{T_{\max}^{*(k)}} \left[\frac{\partial \pi_{\max}^{(k)}}{\partial g_s^k} - \omega_k^2 \frac{\partial T_{\max}^{*(k)}}{\partial g_s^k} \right] \quad (5.66)$$

knowing that $(\sum g_i^k \psi^j)^2 \neq 0$ and therefore $T_{\max}^{*(k)} \neq 0$, the minimization problem may be simplified as

$$\frac{\partial \pi_{\max}^{(k)}}{\partial g_i^k} - \omega_k^2 \frac{\partial T_{\max}^{*(k)}}{\partial g_i^k} = 0 \quad (5.67)$$

where the two partial derivatives are formulated from Eq. (5.62) as

$$\begin{aligned} \frac{\partial \pi_{\max}^{(k)}}{\partial g_s^k} &= \sum_{i=1}^n g_i^{(k)} \left[E_b I \int_0^{x_c} \psi_1^{s''}(x) \psi_1^{i''}(x) dx + E_b I \int_{x_c}^L \psi_2^{s''}(x) \psi_2^{i''}(x) dx \right. \\ &\quad \left. + C_E E_b I \psi_1^{s''}(x_c) \psi_1^{i''}(x_c) \right] + \int_0^{x_c} M_{T_z} \psi_1^{s''}(x) dx + \int_{x_c}^L M_{T_z} \psi_2^{s''}(x) dx \\ &\quad + C_E M_{T_z}(x_c) \psi_1^{s''}(x_c) \\ \frac{\partial T_{\max}^{*(k)}}{\partial g_s^k} &= \sum_{i=1}^n g_i^{(k)} \rho h_b b \left[\int_0^{x_c} \psi_1^s(x) \psi_1^i(x) dx + \int_{x_c}^L \psi_2^s(x) \psi_2^i(x) dx \right] \end{aligned} \quad (5.68)$$

Eq. (5.67) may be rewritten as

$$\sum_{i=1}^N (k_{is} - \omega_k^2 m_{is}) g_i^k = d_s, \quad i = 1, 2, \dots, N \quad (5.69)$$

where the modified stiffness and mass matrices of k_{is} and m_{is} and the vector d_s are formulated as

$$\begin{aligned} k_{is} &= E_b I \int_0^{x_c} \psi_1^{s''}(x) \psi_1^{i''}(x) dx + E_b I \int_{x_c}^L \psi_2^{s''}(x) \psi_2^{i''}(x) dx \\ &\quad + C_E E_b I \psi_1^{s''}(x_c) \psi_1^{i''}(x_c) \\ m_{is} &= \rho h_b b \left[\int_0^{x_c} \psi_1^s(x) \psi_1^i(x) dx + \int_{x_c}^L \psi_2^s(x) \psi_2^i(x) dx \right] \\ d_s &= C_E M_{T_z}(x_c) \psi_1^{s''}(x_c) + \int_0^{x_c} M_{T_z} \psi_1^{s''}(x) dx + \int_{x_c}^L M_{T_z} \psi_2^{s''}(x) dx \end{aligned} \quad (5.70)$$

This equation may be written in the matrix form as

$$\left[\mathbf{k} - (\omega^{(k)})^2 \mathbf{m} \right] \mathbf{g}^{(k)} = \mathbf{d} \quad (5.71)$$

where $\mathbf{g}^{(k)} = \{g_1^{(k)}, g_2^{(k)}, \dots, g_n^{(k)}\}^T$ is the vector of Ritz coefficients.

It is important to note from Eq. (5.70) that in the absence of temperature variations the thermal stress is equal to zero, therefore, vector \mathbf{d} equals zero. This reduces the matrix equation of Eq. (5.71) to the eigenvalue problem of finding the resonant frequencies of a cracked beam. Moreover, this equation shows that temperature variations affect the natural frequencies of the vibrating mode only through the change in the material properties. The characteristic equation of Eq. (5.71) may be numerically solved for different temperature and crack scenarios and is given in section 5.3 for some examples.

5.2.4. Vibrations of a PZT-actuated Beam with Varying Temperature Distribution and a Growing Crack

In this section the PZT-driven vibrations of a cracked Euler-Bernoulli beam is studied considering the effect of varying temperature distributions inside the beam along with the effect of damage growth. The presence of a surface-bonded layer of PZT actuator/sensor can be included in the modeling of the vibrations of the cracked beam of Figure 5.4 through modifications of the total strain energy (due to the electromechanical coupling between the beam and the PZT) and the total kinetic energy (due to the added mass of the PZT layer). The presence of the PZT layer also results in the addition of the internal energy of this piezoelectric layer to the total energy of the structure as explained in the following. It is assumed here that the crack does not occur under the PZT layer.

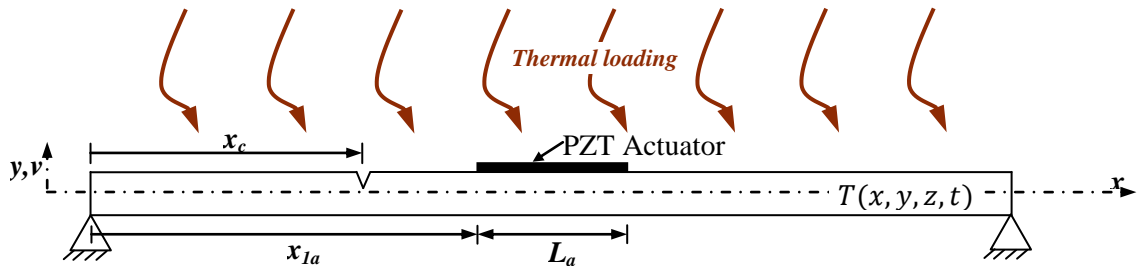


Figure 5.4. Beam with a single fatigue crack under PZT actuation

In order to formulate the equation of motion of the beam of Figure 5.4, Lagrange equations and the assumed mode method are applied here. Using the assumed mode approximation method, transverse deflection of the vibrating beam under the actuation of a surface-bonded PZT patch is given as [74]

$$v(x, t) = \sum_{k=1}^{n_a} v^{(k)}(x, t) = \sum_{k=1}^{n_a} X^{(k)}(x)q_k(t) \quad (5.72)$$

where n_a is the number of modes used in the summation, $X^{(k)}(x)$'s are admissible functions, satisfying the geometric boundary conditions of the vibrating beam and $q_k(t)$'s are the corresponding, unknown, time-dependent generalized coordinates. The admissible functions considered here are the mode shapes of the cracked beam in the absence of temperature variations and PZT actuation as formulated in section 5.2.1.a.I and given in Eq. (5.18). The total strain and kinetic energies of the beam with the PZT layer need to be formulated before applying the Lagrange equation. The strain and kinetic energies of the cracked beam under thermal loading was formulated in section 5.2.3 and given in Eq. (5.58). The kinetic and strain energies of the PZT layer together with the internal energy of this patch will be formulated in the following and added to the energies of the cracked beam in order to formulate the total energy of the complete structure of Figure 5.4.

Considering the linear piezoceramic constitutive relations, the stress (σ_{xx}^p) and strain (ε_{xx}^p) of the PZT are formulated as [67]

$$\begin{aligned} \sigma_{xx}^p &= c_{11}^E \varepsilon_{xx}^p - e_{31} E_3 \\ \varepsilon_{xx}^p &= -y \frac{\partial^2 v(x, t)}{\partial x^2} \end{aligned} \quad (5.73)$$

where c_{11}^E , e_{31} and E_3 are modulus of elasticity of the PZT at constant electric field, piezoelectric stress constant and the electric field across the electrodes of the PZT, respectively. Eq. (5.73) is formulated in the absence of temperature variations. If the temperature inside the PZT layer is not constant, the stress inside the beam will be modified as given in the following equation, while the strain relation will be the same as given in Eq. (5.73)

$$\begin{aligned}\sigma_{xx}^p &= c_{11}^{E,T} \varepsilon_{xx}^p - e_{31}^T E_3 - \lambda_1^E T \\ \varepsilon_{xx}^p &= -y \frac{\partial^2 v(x,t)}{\partial x^2}\end{aligned}\quad (5.74)$$

where T is the temperature variations and the modulus of elasticity and stress constant of the PZT are given at constant temperature [107]. λ_1^E is the stress-temperature coefficient at constant electric field and is given as [106]

$$\lambda_1^E = c_{11}^{E,T} \alpha_t^p \quad (5.75)$$

where α_t^p is the thermal expansion coefficient of the PZT. The relation between the electric field and the voltage $V(t)$ across the PZT surfaces, and between e_{31}^T and the piezoelectric strain constant of d_{31} are

$$\begin{aligned}E_3 &= \frac{V(t)}{h_a} \\ e_{31}^T &= c_{11}^{E,T} d_{31}\end{aligned}\quad (5.76)$$

The strain and kinetic energies of the PZT patch are formulated as

$$\begin{aligned}\pi_p &= \frac{1}{2} \iiint_{V_{\text{PZT}}} (\sigma_{xx}^p \varepsilon_{xx}^p) dV_{\text{PZT}} \\ T_p &= \frac{1}{2} \iiint_{V_{\text{PZT}}} \rho_a \left(\frac{\partial v}{\partial t} \right)^2 dV_{\text{PZT}}\end{aligned}\quad (5.77)$$

It is assumed that the PZT patch is located at x_{1a} , is L_a long and h_a thick and has the same width as the beam, as shown in Figure 5.4. It is also assumed that the PZT layer has a uniform density of ρ_a . These two energies may be simplified by substituting Eqs. (5.74) and (5.76) into Eq. (5.77) as

$$\begin{aligned}\pi_p &= \frac{1}{2} c_{11}^{E,T} I_p \int_{x_{1a}}^{x_{2a}} \left(\frac{\partial^2 v}{\partial x^2} \right)^2 dx + \frac{1}{2} J_p V(t) \int_{x_{1a}}^{x_{2a}} \frac{\partial^2 v}{\partial x^2} dx \\ &\quad + \frac{1}{2} \lambda_1^E \int_{x_{1a}}^{x_{2a}} M_T^p(x, t) \frac{\partial^2 v}{\partial x^2} dx \\ T_p &= \frac{1}{2} \rho_a h_a b \int_{x_{1a}}^{x_{2a}} \left(\frac{\partial v}{\partial t} \right)^2 dx\end{aligned}\quad (5.78)$$

where

$$\begin{aligned} x_{2a} &= x_{1a} + L_a \\ J_p &= e_{31}^T b(h_b + h_a)/2 \end{aligned} \quad (5.79)$$

, I_p is the area moments of inertia of the PZT layer with respect to the z -axis given as

$$I_p = \frac{1}{3} b h_a^3 + \frac{1}{4} b h_a h_b (h_b + 2h_a) \quad (5.80)$$

and assuming the temperature does not vary along the thickness of the PZT layer, $M_T^p(x, t)$ is given as

$$M_T^p(x, t) = \frac{h_a(h_a+h_b)}{2} \int_{-b/2}^{b/2} T(x, \frac{h_b}{2}, z, t) dz \quad (5.81)$$

The internal electrical energy of the PZT layer is also given by [9]

$$W_{ip} = \frac{1}{2} \iiint_{V_{\text{PZT}}} D_3 E_3 dV_{\text{PZT}} \quad (5.82)$$

where the electric displacement, D_3 , of the PZT layer is related to the strain, electric field across the electrodes and temperature as [107]

$$D_3 = e_{31}^T \varepsilon_{xx}^p + \epsilon_{33}^{\varepsilon, T} E_3 + P_3^\varepsilon T \quad (5.83)$$

with $\epsilon_{33}^{\varepsilon, T}$ being the dielectric permittivity of the PZT measured at zero strain and zero temperature variations and P_3^ε is the pyroelectric constant of the PZT measured at zero strain. In the modeling presented here, it is assumed that the material properties of the PZT layer do not vary with temperature and the effect of temperature on the PZT response is only included through considering the pyroelectric constant and the stress-temperature coefficient. By substituting Eqs. (5.74), (5.76) and (5.83) into Eq. (5.82), the internal electrical energy of the PZT layer may be simplified as

$$\begin{aligned} W_{ip} &= -\frac{1}{2} J_p V(t) \int_{x_{1a}}^{x_{2a}} \frac{\partial^2 v}{\partial x^2} dx + \frac{1}{2} \epsilon_{33}^{\varepsilon, T} V_{\text{PZT}} \left(\frac{V(t)}{h_a} \right)^2 \\ &\quad + \frac{1}{2} \frac{P_3^\varepsilon}{h_a} V(t) N_T^p(t) \end{aligned} \quad (5.84)$$

with $V_{\text{PZT}} = L_a b h_a$ and

$$N_T^p(t) = \int_{x_{1a}}^{x_{2a}} \int_{-b/2}^{b/2} \int_{h_b/2}^{h_b/2+h_a} T(x, y, z, t) dy dz dx \quad (5.85)$$

Total strain and kinetic energies of the PZT-actuated beam of Figure 5.4 are given as

$$\begin{aligned} \pi_{\text{total}} &= \pi_b + \pi_p + U_{\text{crack}} \\ T_{\text{total}} &= T_b + T_p \end{aligned} \quad (5.86)$$

where the strain and kinetic energies of the cracked beam and the energy stored in the crack was given in Eq. (5.58) and rewritten here as

$$\begin{aligned} \pi_b + U_{\text{crack}} &= \frac{1}{2} \int_0^L \left[E_b I \left(\frac{\partial^2 v}{\partial x^2} \right)^2 + M_{T_z}(x, t) \frac{\partial^2 v}{\partial x^2} \right] dx \\ &\quad + \frac{1}{2} C_E E_b I \left(\frac{\partial^2 v}{\partial x^2} \Big|_{x=x_c} \right)^2 + \frac{1}{2} C_E \left(M_{T_z} \frac{\partial^2 v}{\partial x^2} \Big|_{x=x_c} \right) \\ T_b &= \frac{1}{2} \int_0^L \rho h_b b \left(\frac{\partial v}{\partial t} \right)^2 dx \end{aligned} \quad (5.87)$$

By substituting Eqs. (5.78) and (5.87) into Eq. (5.86), the total kinetic and strain energies of the PZT-driven cracked beam of Figure 5.4 is given as

$$\begin{aligned} \pi_{\text{total}} &= \frac{1}{2} E_b I \int_0^L \left(\frac{\partial^2 v}{\partial x^2} \right)^2 dx + \frac{1}{2} c_{11}^{E,T} I_p \int_{x_{1a}}^{x_{2a}} \left(\frac{\partial^2 v}{\partial x^2} \right)^2 dx + \frac{1}{2} J_p V(t) \int_{x_{1a}}^{x_{2a}} \frac{\partial^2 v}{\partial x^2} dx \\ &\quad + \frac{1}{2} \int_0^L M_{T_z}(x, t) \frac{\partial^2 v}{\partial x^2} dx + \frac{1}{2} \lambda_1^E \int_{x_{1a}}^{x_{2a}} M_T^p(x, t) \frac{\partial^2 v}{\partial x^2} dx \\ &\quad + \frac{1}{2} C_E E_b I \left(\frac{\partial^2 v}{\partial x^2} \Big|_{x=x_c} \right)^2 + \frac{1}{2} C_E \left(M_{T_z} \frac{\partial^2 v}{\partial x^2} \Big|_{x=x_c} \right) \\ T_{\text{total}} &= \frac{1}{2} \int_0^L (\rho A)(x) \left(\frac{\partial v}{\partial t} \right)^2 dx \end{aligned} \quad (5.88)$$

where $(\rho A)(x) = \rho h_b b + \rho_a h_a b [H(x - x_{1a})H(x_{2a} - x)]$.

Substituting the assumed formulation of $v(x, t)$ as given in Eq. (5.72) into the potential, kinetic and the PZT-internal energies of Eqs. (5.88) and (5.84) yields

$$\begin{aligned}\pi_{\text{total}} &= \frac{1}{2} \sum_{k=1}^{n_a} \sum_{i=1}^{n_a} K_{ki} q_i(t) q_k(t) + \sum_{k=1}^{n_a} \left[R_T^k(t) + \frac{1}{2} \eta_{ip}^k V(t) \right] q_k(t) \\ T_{\text{total}} &= \frac{1}{2} \sum_{k=1}^{n_a} \sum_{i=1}^{n_a} M_{ki} \dot{q}_i(t) \dot{q}_k(t)\end{aligned}\quad (5.89)$$

$$W_{ip} = -\frac{1}{2} \sum_{k=1}^{n_a} \eta_{ip}^k V(t) q_k(t) + \frac{1}{2} \frac{\epsilon_{33}^{E,T} V_{PZT}}{h_a^2} V(t)^2 + \frac{1}{2} \frac{P_3^E}{h_a} N_T^p(t) V(t)$$

where

$$\begin{aligned}K_{ki} &= \int_0^L E_b I X^{(k)''} X^{(i)''} dx + \int_{x_{1a}}^{x_{2a}} c_{11}^{E,T} I_p X^{(k)''} X^{(i)''} dx \\ &\quad + C_E E_b I X^{(k)''}(x_c) X^{(i)''}(x_c) \\ R_T^k(t) &= \frac{1}{2} \int_0^L M_{T_z}(x, t) X^{(k)''} dx + \frac{1}{2} \lambda_1^E \int_{x_{1a}}^{x_{2a}} M_T^p(x, t) X^{(k)''} dx \\ &\quad + \frac{1}{2} C_E M_{T_z}(x_c, t) X^{(k)''}(x_c) \\ M_{ki} &= \int_0^L (\rho A)(x) X^{(k)} X^{(i)} dx \\ \eta_{ip}^k &= \int_{x_{1a}}^{x_{2a}} J_p X^{(k)''} dx\end{aligned}\quad (5.90)$$

The two Lagrange equations for the two coordinates of $q_j(t)$ and $V(t)$, the temperature-induced voltage, are expressed as

$$\frac{d}{dt} \left(\frac{\partial T_{\text{total}}}{\partial \dot{q}_j} \right) - \frac{\partial T_{\text{total}}}{\partial q_j} + \frac{\partial \pi_{\text{total}}}{\partial q_j} - \frac{\partial W_{ip}}{\partial q_j} = 0 \quad (5.91)$$

$$\frac{d}{dt} \left(\frac{\partial T_{\text{total}}}{\partial \dot{V}} \right) - \frac{\partial T_{\text{total}}}{\partial V} + \frac{\partial \pi_{\text{total}}}{\partial V} - \frac{\partial W_{ip}}{\partial V} = \frac{\partial W_{nc}}{\partial V} \quad (5.92)$$

where W_{nc} is the non-conservative work due to the charge output of the PZT layers, $Q(t)$, and is formulated as

$$W_{nc} = Q(t)V(t) \quad (5.93)$$

It is important to note that if the function of temperature variations inside the beam was not known a third Lagrange equation would have been necessary for the temperature as the third coordinate. However, in our problem the theory of thermal stresses is applied which assumes that the coupling of displacement and temperature in entropy formulations is negligible. Therefore, it is assumed here that temperature variations inside the beam are known. Moreover, the equation given in Eq. (5.92) is useful when the PZT patch is used as a sensor in an open circuit setup or for the energy harvesting applications

where the temperature-induced current in the PZT passes through a load resistor with known resistance. When using the PZT patch as an actuator, however, the amount of input voltage to the PZT electrodes are fixed at the desired voltage. In other words, the electric field of Eq. (5.76) may be formulated as

$$V(t) = V_g(t) + v_T(t) \quad (5.94)$$

where $v_T(t)$ is the temperature-induced voltage and $V_g(t)$ is the applied voltage by the function generator to the PZT. Therefore due to the PZT pyroelectric effect, if the PZT patch is used as an actuator (which is the case in the problem presented here) variations in temperature will result in variations of the voltage generated by the function generator. This effect had been verified experimentally by others and interpreted as the change in the actuator capacitance due to the change in temperature [87].

The non-zero terms of the first Lagrange equation, Eq. (5.91), are

$$\begin{aligned} \frac{\partial T_{\text{total}}}{\partial \dot{q}_j} &= \frac{1}{2} \sum_{k=1}^{n_a} (M_{jk} + M_{kj}) \dot{q}_k(t) \\ \frac{\partial \pi_{\text{total}}}{\partial q_j} &= \frac{1}{2} \sum_{k=1}^{n_a} (K_{jk} + K_{kj}) q_k(t) + R_T^j(t) + \frac{1}{2} \eta_{ip}^j V(t) \\ \frac{\partial W_{ip}}{\partial q_j} &= -\frac{1}{2} \eta_{ip}^j V(t) \end{aligned} \quad (5.95)$$

Knowing that the matrices of \mathbf{K} and \mathbf{M} are symmetric and substituting terms of Eqs. (5.95) into the Lagrange equation of Eq. (5.91) yields

$$\sum_{k=1}^{n_a} M_{jk} \ddot{q}_k(t) + \sum_{k=1}^{n_a} K_{jk} q_k(t) + \eta_{ip}^j V(t) + R_T^j(t) = 0 \quad (5.96)$$

Eq. (5.96) may be rewritten in matrix form as

$$[\mathbf{M}]\ddot{\mathbf{q}}(t) + [\mathbf{K}]\mathbf{q}(t) = -\boldsymbol{\eta}_{ip} V(t) - \mathbf{R}_T(t) \quad (5.97)$$

with

$$\begin{aligned}
\mathbf{q}(t) &= \{q_1(t) \quad q_2(t) \quad \cdots \quad q_{n_a}(t)\}^T \\
\ddot{\mathbf{q}}(t) &= \left\{ \frac{d^2 q_1(t)}{dt^2} \quad \frac{d^2 q_2(t)}{dt^2} \quad \cdots \quad \frac{d^2 q_{n_a}(t)}{dt^2} \right\}^T \\
\boldsymbol{\eta}_{ip} &= \{\eta_{ip}^1 \quad \eta_{ip}^2 \quad \cdots \quad \eta_{ip}^{n_a}\}^T \\
\mathbf{R}_T(t) &= \{R_T^1(t) \quad R_T^2(t) \quad \cdots \quad R_T^{n_a}(t)\}^T
\end{aligned} \tag{5.98}$$

A practical example of the beam under the study is to consider the piezoceramic patch to be a self-sensing actuator. This patch is used as a sensor for measuring the vibratory behavior of the structure and as an actuator for control applications and mainly for the suppression of thermally-induced beam vibrations. Therefore, when the beam structure undergoes temperature variations and thermal loading, the two Lagrange equations for the two coordinates of $q_j(t)$ and $v_s(t)$, the sensor voltage, are expressed as

$$\frac{d}{dt} \left(\frac{\partial T_{\text{total}}}{\partial \dot{q}_j} \right) - \frac{\partial T_{\text{total}}}{\partial q_j} + \frac{\partial \pi_{\text{total}}}{\partial q_j} - \frac{\partial W_{ip}}{\partial q_j} = 0 \tag{5.99}$$

$$\frac{d}{dt} \left(\frac{\partial T_{\text{total}}}{\partial \dot{v}_s} \right) - \frac{\partial T_{\text{total}}}{\partial v_s} + \frac{\partial \pi_{\text{total}}}{\partial v_s} - \frac{\partial W_{ip}}{\partial v_s} = \frac{\partial W_{nc}}{\partial v_s} \tag{5.100}$$

where W_{nc} is the non-conservative work due to the charge output of the PZT sensor, $Q(t)$, and is formulated as

$$W_{nc} = Q(t)v_s(t) \tag{5.101}$$

Based on Eq. (5.96) and knowing that the voltage across the PZT is $V(t) = v_s(t)$, the first Lagrange equation is formulated as

$$\sum_{k=1}^{n_a} M_{jk} \ddot{q}_k(t) + \sum_{k=1}^{n_a} K_{jk} q_k(t) + \eta_{ip}^j v_s(t) + R_T^j(t) = 0 \tag{5.102}$$

Eq. (5.96) may be rewritten in matrix form as

$$[\mathbf{M}]\ddot{\mathbf{q}}(t) + [\mathbf{K}]\mathbf{q}(t) + \boldsymbol{\eta}_{ip} v_s(t) = -\mathbf{R}_T(t) \tag{5.103}$$

with $[\mathbf{M}]$, $[\mathbf{K}]$, $\ddot{\mathbf{q}}(t)$, $\mathbf{q}(t)$, $\boldsymbol{\eta}_{ip}$ and $\mathbf{R}_T(t)$ given in Eqs. (5.90) and (5.98).

Similarly, the second Lagrange equation of Eq. (5.100) is simplified as

$$\sum_{k=1}^{n_a} \eta_{ip}^k \dot{q}_k(t) - \frac{\epsilon_{33}^T V_{PZT}}{h_a^2} \dot{v}_s(t) - \frac{1}{2} \frac{P_3^\xi}{h_a} \dot{N}_T^p(t) = \frac{v_s(t)}{R} \quad (5.104)$$

where $\dot{Q}(t)$ is equal to the current across the PZT sensing circuit and has been replaced by the amount of voltage across the two plates of the PZT over the resistance of the sensing circuit (R). Eq. (5.104) may be rewritten in matrix form as

$$C_a \dot{v}_s(t) + \frac{1}{R} v_s(t) + \frac{1}{2} \frac{P_3^\xi}{h_a} \dot{N}_T^p(t) - \boldsymbol{\eta}_{ip}^T \dot{\mathbf{q}}(t) = 0 \quad (5.105)$$

where C_a is the capacitance of the PZT and given as

$$C_a = \epsilon_{33}^T \frac{V_{PZT}}{h_a^2} \quad (5.106)$$

Therefore, the coupled set of temporal equations is given in Eqs. (5.103) and (5.105) and rewritten here for better understanding of the effect of different parameters

$$[\mathbf{M}]\ddot{\mathbf{q}}(t) + [\mathbf{K}]\mathbf{q}(t) + \boldsymbol{\eta}_{ip} v_s(t) = -\mathbf{R}_T(t) \quad (5.107)$$

$$C_a \dot{v}_s(t) + \frac{1}{R} v_s(t) + \frac{1}{2} \frac{P_3^\xi}{h_a} \dot{N}_T^p(t) - \boldsymbol{\eta}_{ip}^T \dot{\mathbf{q}}(t) = 0 \quad (5.108)$$

where $\boldsymbol{\eta}_{ip}$ is the coupling vector, given in Eq. (5.98). With the PZT acting as a sensor, the only forcing vector is the thermal loading represented by $\mathbf{R}_T(t)$.

5.2.4.a. The forcing vector, $\mathbf{R}_T(t)$, for different temperature variations scenarios

The effect of temperature through generation of thermal moments is seen in the formulations by variations it causes on the forcing vector of $\mathbf{R}_T(t)$ as given in Eq. (5.90). In this section, different general temperature variations scenarios are presented along with their resultant forcing vector. It is assumed here that the temperature distribution inside the beam is independent of the coordinate along width of the beam (the z -axis), i.e. temperature distribution has the general form of $T(x, y, t)$.

As mentioned earlier, the temperature distribution inside the beam is assumed to be a function of x , y and time. A simplifying assumption is made here by applying the separation of variables to the temperature formulation as

$$T(x, y, t) = T_x(x)T_y(y)T_t(t) \quad (5.109)$$

Substituting this temperature function into Eq. (5.53) gives the general formulation of the thermal moment as

$$\begin{aligned} M_{T_z}(x, t) &= B_T T_x(x)T_t(t) \\ B_T &= \alpha_t E_b b \int_{-h_b/2}^{h_b/2} T_y(y) y dy \end{aligned} \quad (5.110)$$

It is very important to note that if temperature distribution inside the beam is independent of the y coordinate, the thermal moment vanishes according to the integration given in Eq. (5.110).

Substituting the thermal moment of Eq. (5.110) into the forcing vector formulation of Eq. (5.90) and applying the integration by parts and the compatibility conditions at the place of the crack yields

$$\begin{aligned} R_T^k(t) &= \frac{1}{2} \left[M_{T_z}(L, t) X^{(k)'}(L) - M_{T_z}(0, t) X^{(k)'}(0) \right] \\ &+ \frac{1}{2} \left[M_{T_z}'(L, t) X^{(k)}(0) - M_{T_z}'(0, t) X^{(k)}(L) \right] \\ &+ \frac{1}{2} \int_0^L M_{T_z}''(x, t) X^{(k)} dx \\ &+ \frac{1}{2} \lambda_1^E \int_{x_{1a}}^{x_{2a}} M_T^p(x, t) X^{(k)''} dx \end{aligned} \quad (5.111)$$

where

$$\begin{aligned} M_T^p(x, t) &= B_T^p T_x(x)T_t(t) \\ B_T^p &= \frac{h_a(h_a+h_b)}{2} b T_y\left(\frac{h_b}{2}\right) \end{aligned} \quad (5.112)$$

The first two terms of the forcing vector result from the boundary conditions of the beam and the effect thermal moment has at these points. For a beam fixed at both ends, these all vanish and the forcing vector simplifies to

$$R_T^k(t) = \frac{1}{2} \int_0^L M_{T_z}''(x, t) X^{(k)} dx + \frac{1}{2} \lambda_1^E \int_{x_{1a}}^{x_{2a}} M_T^p(x, t) X^{(k)''} dx \quad (5.113)$$

and, therefore, the forcing vector would only have a noticeable effect if the second derivative of thermal moment with respect to x , $M_{T_z}''(x, t)$, is non-zero. For a beam simply supported on both ends, the forcing vector simplifies to

$$R_T^k(t) = \frac{1}{2} \left[M_{T_z}(L, t) X^{(k)'}(L) - M_{T_z}(0, t) X^{(k)'}(0) \right] + \frac{1}{2} \int_0^L M_{T_z}''(x, t) X^{(k)} dx + \frac{1}{2} \lambda_1^E \int_{x_{1a}}^{x_{2a}} M_T^p(x, t) X^{(k)''} dx \quad (5.114)$$

If the second derivative of thermal moment with respect to x , $M_{T_z}''(x, t)$, is equal to zero, then the forcing vector may be much more simplified for the simply supported and clamped-clamped beams. A special example of this condition would be considering temperature distribution that is independent of the x coordinate, $T(y, t)$. In this case, the thermal moment will also be independent of the x coordinate. The forcing vector will, therefore, be simplified for the clamped-clamped and simply supported beams, respectively, as

$$\begin{aligned} \text{CC: } R_T^k(t) &= \frac{1}{2} \lambda_1^E M_T^p(t) \int_{x_{1a}}^{x_{2a}} X^{(k)''} dx \\ \text{SS: } R_T^k(t) &= \frac{1}{2} M_{T_z}(t) \left[X^{(k)'}(L) - X^{(k)'}(0) \right] + \frac{1}{2} \lambda_1^E M_T^p(t) \int_{x_{1a}}^{x_{2a}} X^{(k)''} dx \end{aligned} \quad (5.115)$$

Temperature distribution may have any format with respect to the coordinates and time. A special example to be studied is to consider harmonic temperature distribution with respect to time, in other words, a temperature distribution of

$$T(x, y, t) = T_x(x) T_y(y) e^{i\Omega_T t} \quad (5.116)$$

Applying this temperature distribution into the thermal moment formulations and Eq. (5.114) results in the following simplified forcing vector

$$R_T^k(t) = f_T^k B_T e^{i\Omega_T t} \quad (5.117)$$

where for clamped-clamped and simply supported beams

$$\begin{aligned} \text{CC: } f_T^k &= \frac{1}{2} \lambda_1^E \frac{B_T^p}{B_T} \int_{x_{1a}}^{x_{2a}} T_x(x) X^{(k)''} dx \\ \text{SS: } f_T^k &= \frac{1}{2} \left[T_x(L) X^{(k)'}(L) - T_x(0) X^{(k)'}(0) \right] \\ &+ \frac{1}{2} \int_0^L T_x''(x) X^{(k)} dx + \frac{1}{2} \lambda_1^E \frac{B_T^p}{B_T} \int_{x_{1a}}^{x_{2a}} T_x(x) X^{(k)''} dx \end{aligned} \quad (5.118)$$

If the temperature distribution is independent of the x coordinate, $T_x(x) = 1$, then f_T^k could be further simplified for clamped-clamped and simply supported beams as

$$\begin{aligned}
\mathbf{CC}: f_T^k &= \frac{1}{2} \lambda_1^E \frac{B_T^p}{B_T} \int_{x_{1a}}^{x_{2a}} X^{(k)''} dx \\
\mathbf{SS}: f_T^k &= \frac{1}{2} \left[X^{(k)'}(L) - X^{(k)'}(0) \right] + \frac{1}{2} \lambda_1^E \frac{B_T^p}{B_T} \int_{x_{1a}}^{x_{2a}} X^{(k)''} dx
\end{aligned} \tag{5.119}$$

Considering the harmonic forcing, the generalized coordinate and the sensing voltage will also be harmonic with the frequency of Ω_T as

$$\begin{aligned}
q^k(t) &= Q^k e^{i\Omega_T t} \\
v_s(t) &= V_s e^{i\Omega_T t}
\end{aligned} \tag{5.120}$$

Substituting these formulations into Eqs. (5.107) and (5.108) yields

$$-\Omega_T^2 [\mathbf{M}] \mathbf{Q} + [\mathbf{K}] \mathbf{Q} + \boldsymbol{\eta}_{ip} V_s = -\mathbf{f}_T B_T \tag{5.121}$$

$$i\Omega_T C_a V_s + \frac{1}{R} V_s + i\Omega_T \frac{P_3^\xi}{2h_a} N_T^p - i\Omega_T \boldsymbol{\eta}_{ip}^T \mathbf{Q} = 0 \tag{5.122}$$

where

$$N_T^p = b \int_{x_{1a}}^{x_{2a}} T_x(x) dx \int_{h_b/2}^{h_b/2+h_a} T_y(y) dy \tag{5.123}$$

Solving Eq. (5.122) for V_s yields

$$V_s = \frac{\frac{P_3^\xi}{2h_a} N_T^p - \boldsymbol{\eta}_{ip}^T \mathbf{Q}}{\frac{i}{R\Omega_T} - C_a} = \frac{\frac{P_3^\xi}{2h_a} i\Omega_T N_T^p}{\frac{1}{R} + iC_a \Omega_T} - i\Omega_T \left(\frac{1}{R} + iC_a \Omega_T \right)^{-1} \boldsymbol{\eta}_{ip}^T \mathbf{Q} \tag{5.124}$$

Substituting this value into Eq. (5.121) results in the formulation of \mathbf{Q} as

$$\mathbf{Q} = \left[[\mathbf{K}] - \Omega_T^2 [\mathbf{M}] + \frac{i\Omega_T}{\frac{1}{R} + i\Omega_T C_a} \boldsymbol{\eta}_{ip} \boldsymbol{\eta}_{ip}^T \right]^{-1} \left(\boldsymbol{\eta}_{ip} \frac{\frac{P_3^\xi}{2h_a} i\Omega_T N_T^p}{\frac{1}{R} + i\Omega_T C_a} - \mathbf{f}_T B_T \right) \tag{5.125}$$

The generalized coordinate is then given as

$$\mathbf{q}(t) = \left[[\mathbf{K}] - \Omega_T^2 [\mathbf{M}] + \frac{i\Omega_T}{\frac{1}{R} + i\Omega_T C_a} \boldsymbol{\eta}_{ip} \boldsymbol{\eta}_{ip}^T \right]^{-1} \left(\boldsymbol{\eta}_{ip} \frac{\frac{P_3^\xi}{2h_a} i\Omega_T N_T^p}{\frac{1}{R} + i\Omega_T C_a} - \mathbf{f}_T B_T \right) e^{i\Omega_T t} \tag{5.126}$$

5.3. Numerical Results

In the first part of the numerical analysis presented here, the change in the mode shapes of an Euler-Bernoulli beam with a single fatigue crack growing at different locations along the length of the beam is shown numerically for the crack modeling as the reduction in the local stiffness and as given in section 5.2.1. This is done for a beam with two different support conditions and the change in the mode shapes and the slope of the beam are depicted. The accuracy of the proposed approximation for the mode shapes of the cracked beam as given in section 5.2.1.a.II is then examined. This is done through comparing the resonant frequencies of an Euler-Bernoulli beam with specific dimensions and two boundary conditions for the two modeling approaches of: a) section 5.2.1.a.I with the mode shapes given in Eq. (5.18) , and b) the proposed approximation of section 5.2.1.a.II using Rayleigh-Ritz method and the matrices of Eq. (5.42).

In the second part of the numerical analysis, the effect of temperature variations on the vibratory characteristics of a cracked Euler-Bernoulli beam is investigated for different temperature variation scenarios. This is done by numerically studying the analytical modeling given in section 5.2.3 and considering the effect of crack and the effect of temperature. A PZT sensing patch is then assumed to be bonded to the surface of the cracked beam exposed to temperature variations. This will be the complete modeling as it includes all the modeling parameters of crack growth, temperature variations, electromechanical coupling between the PZT layer and the beam and the pyroelectric effect of the PZT material. The effect of temperature variations and the crack growth will be numerically investigated in the last part of this section by looking at the displacement of the vibrating beam for different modeling parameters. The variations in the output voltage of the PZT sensor are also studied for different temperature distributions and crack specifications.

The beam considered in the numerical analysis is assumed to be made of aluminum with the dimensions of length of 30.48 cm (12"), width of 2.54 cm (1") and thickness of 0.32 cm (1/8") as shown in Figure 5.5.

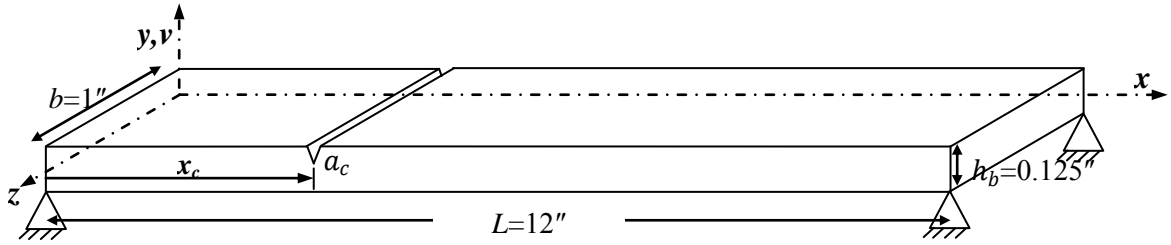


Figure 5.5. Schematic and dimensions of the cracked beam used in the numerical studies

Mass density and modulus of elasticity of the beam are assumed to be measured at 20°C (unless otherwise stated) and equal to 2770 kg/m³ (0.10 lb/in³) and 69.43 GPa (10.07 Mpsi), respectively according to Table 4.1 [98]. Two boundary conditions of simply supported and fixed-fixed are considered in the numerical studies at different sections of the numerical analysis.

5.3.1. Numerical studies on the effect of presence of a growing crack and verification of the proposed Rayleigh-Ritz approximation of the mode shapes of the cracked Euler-Bernoulli beam

Presence of a single fatigue crack was earlier considered as a reduction in the stiffness of the beam at the place of the crack and modeled as a massless rotational spring. The compliance of the resultant spring was shown to be a function of the crack depth ratio. The presence of the crack would then cause a discontinuity of the slope of the beam at the place of the crack where the amount of change in the slope was shown to be proportional to the compliance of the crack-resultant spring and the moment applied at the place of the crack. This form of modeling of the crack and the effect it has on the mode shapes and slope of an Euler-Bernoulli beam is shown in Figure 5.6 to Figure 5.15 for different modes of vibrations of the beam of Figure 5.5 for the first four modes and some special crack locations. Two different support conditions of simply supported on both ends and clamped-clamped are considered for the beam.

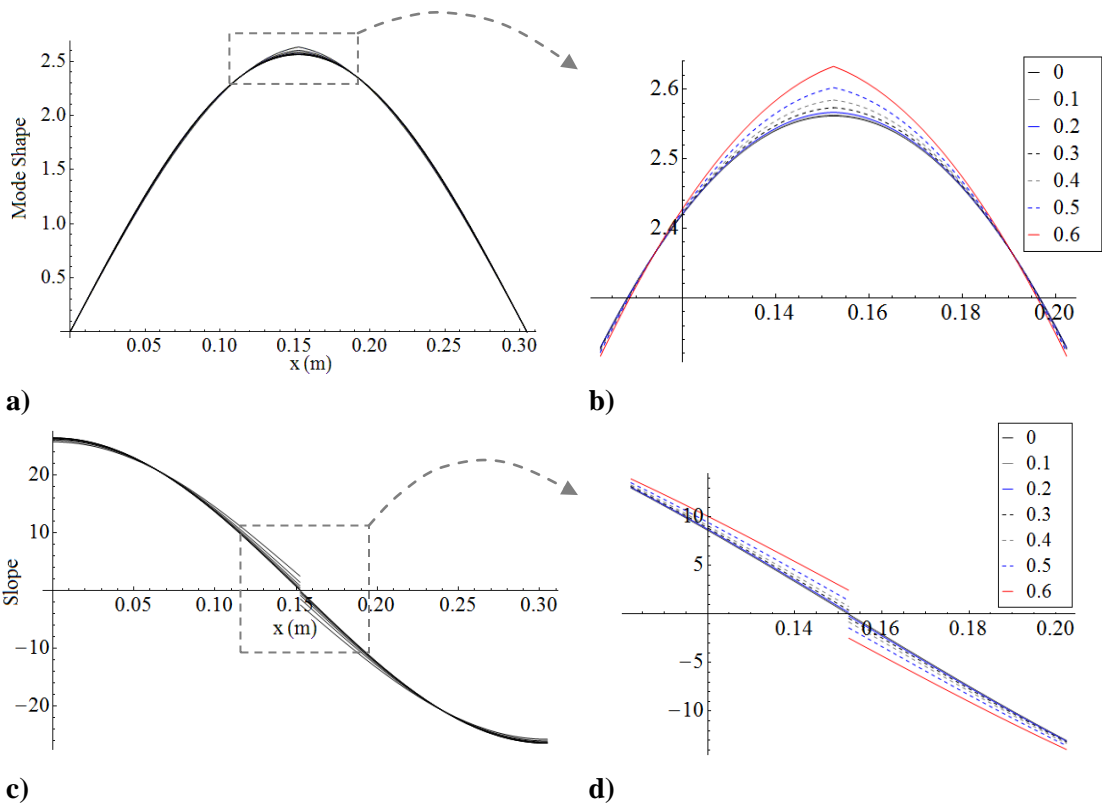


Figure 5.6. a), b) Mode shapes, c), d) slope, of a simply supported beam on both edges for the first mode of vibrations with a growing crack at mid-span

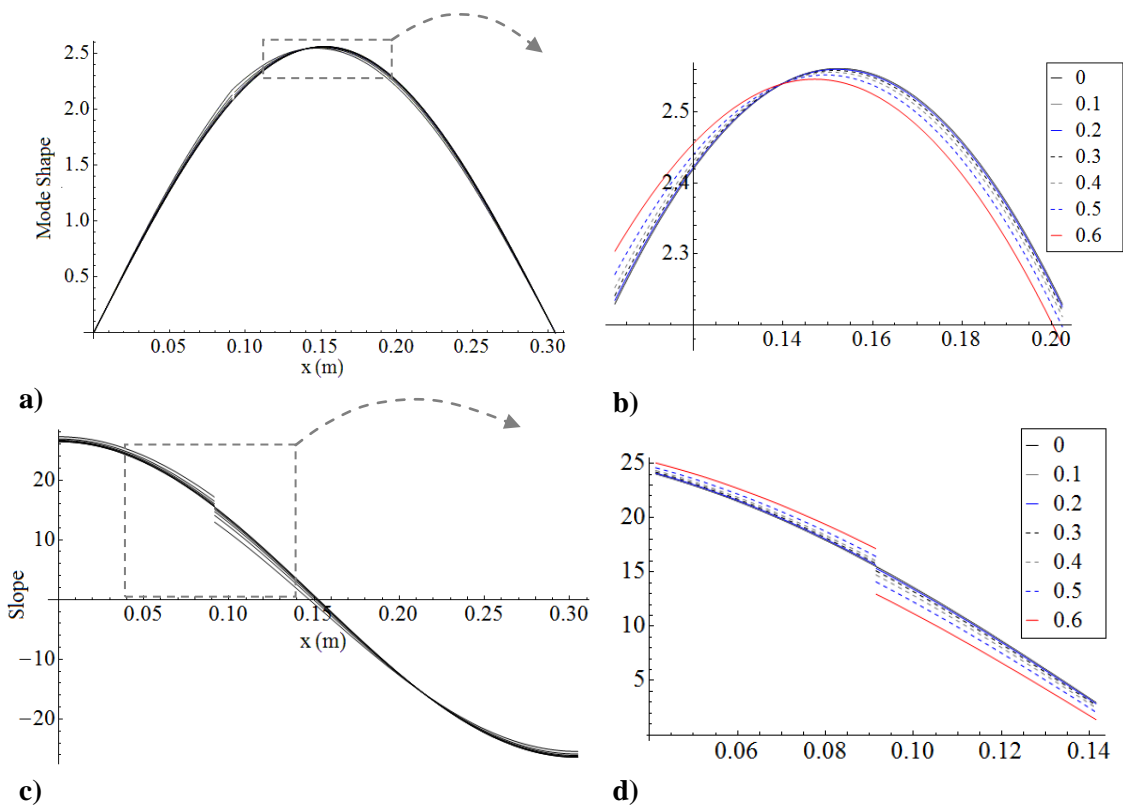


Figure 5.7. a), b) Mode shapes, c), d) slope, of a simply supported beam on both edges for the first mode of vibrations with a growing crack at $0.3L$

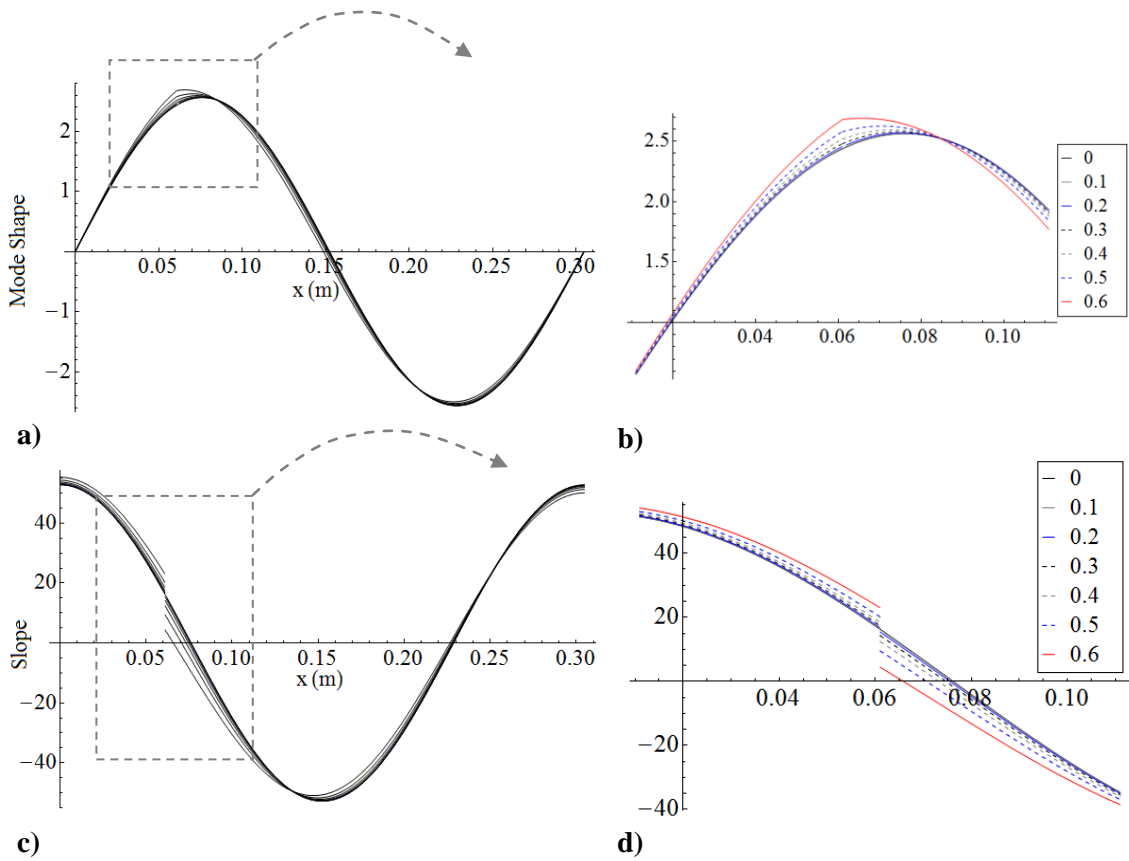


Figure 5.8. a), b) Mode shapes, c), d) slope, of a simply supported beam on both edges for the second mode of vibrations with a growing crack at $0.3L$

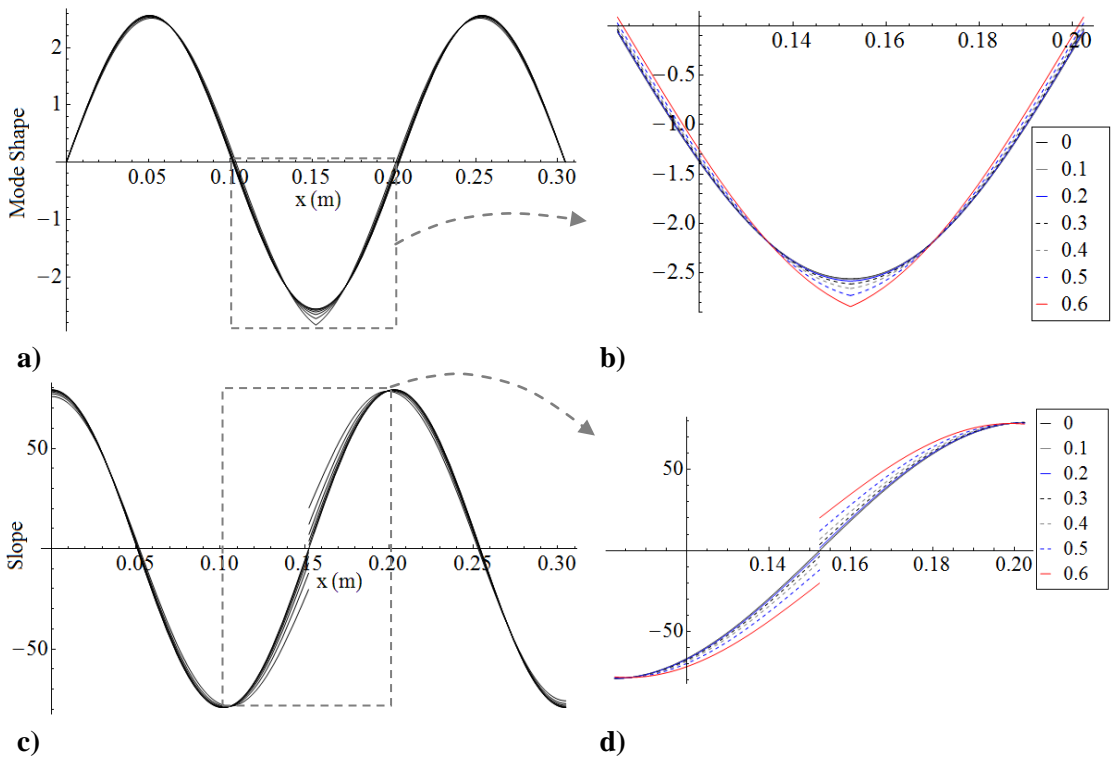


Figure 5.9. a), b) Mode shapes, c), d) slope, of a simply supported beam on both edges for the third mode of vibrations with a growing crack at mid-span

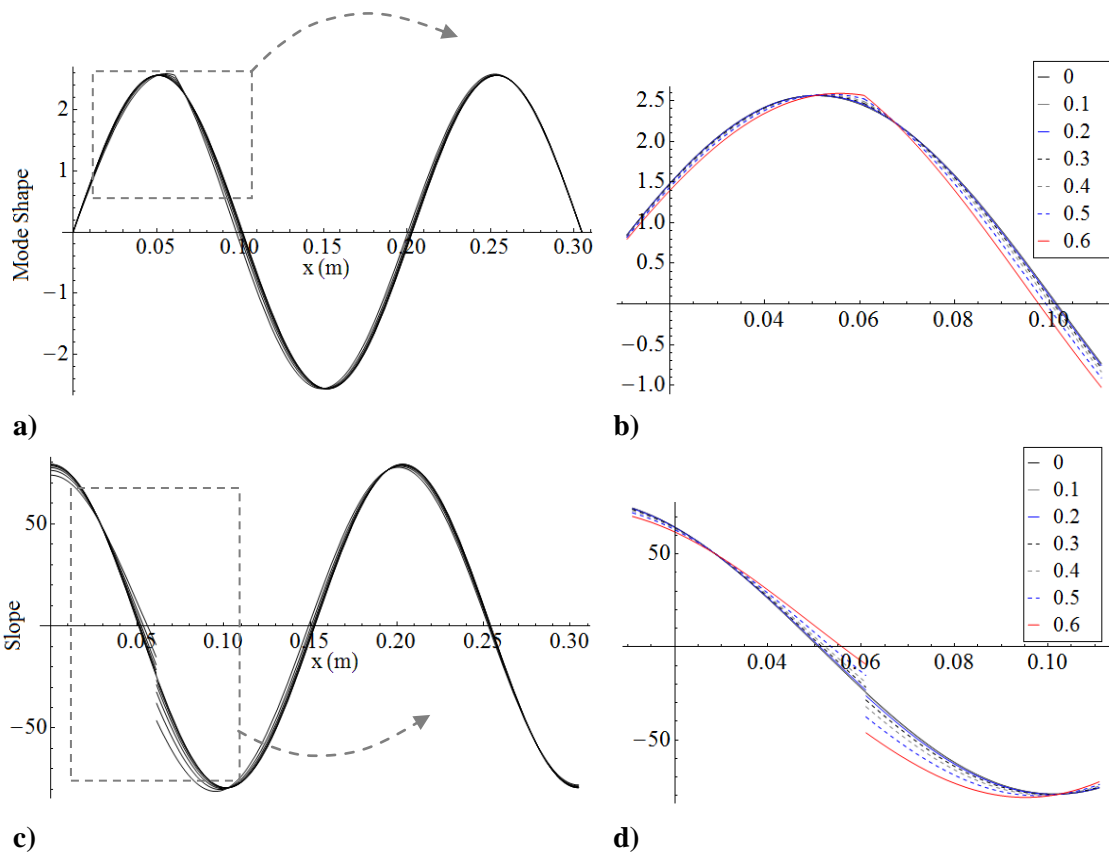


Figure 5.10. a), b) Mode shapes, c), d) slope, of a simply supported beam on both edges for the third mode of vibrations with a growing crack at $0.2L$

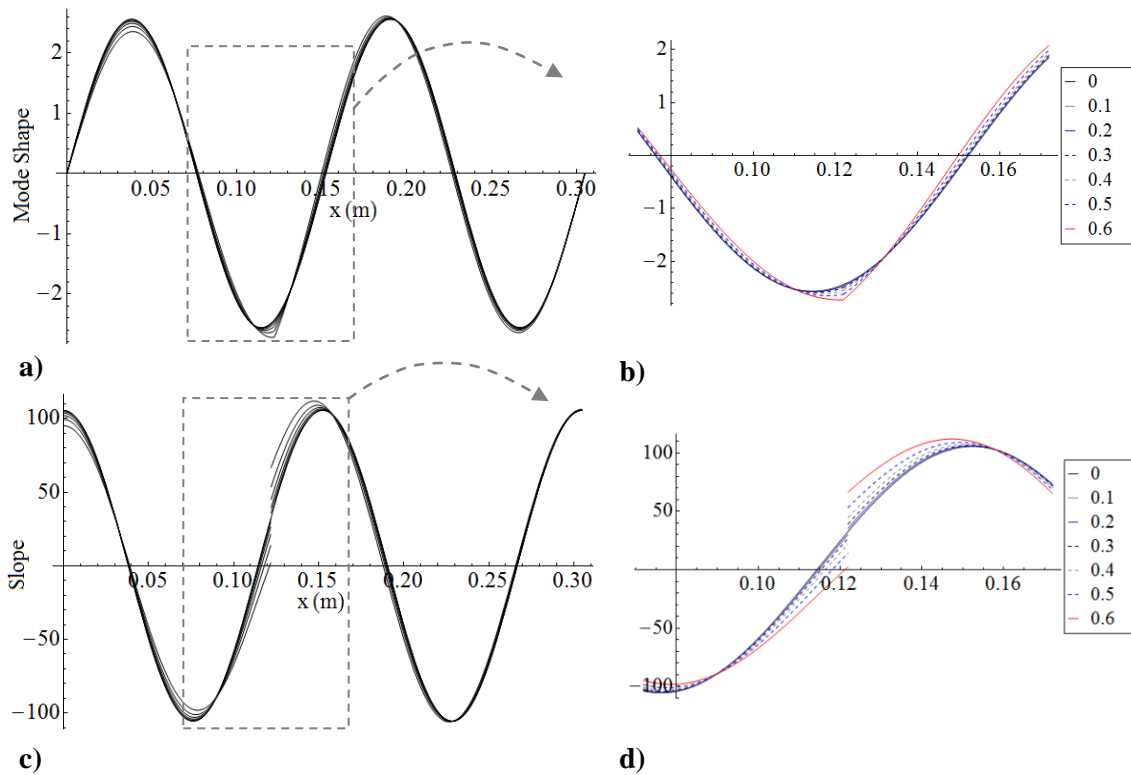


Figure 5.11. a), b) Mode shapes, c), d) slope, of a simply supported beam on both edges for the fourth mode of vibrations with a growing crack at $0.4L$

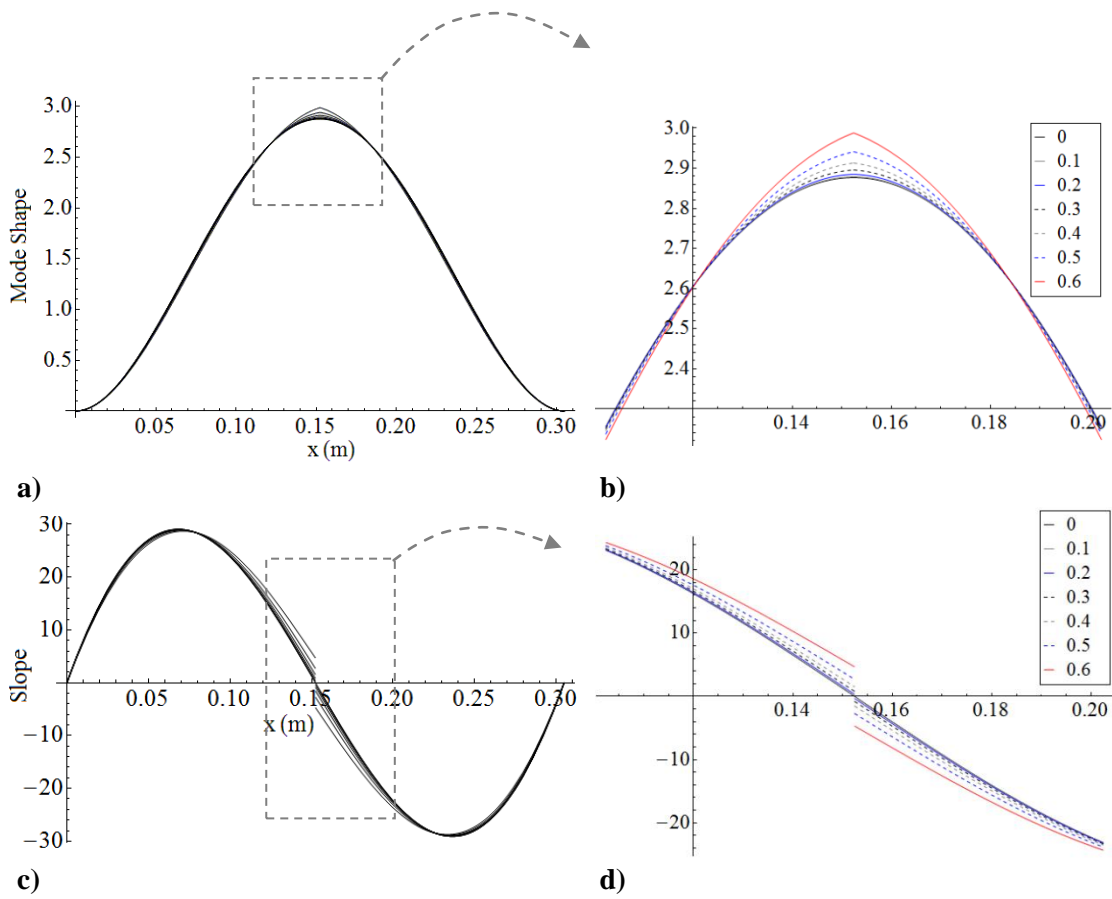


Figure 5.12. a), b) Mode shapes, c), d) slope, of a clamped beam on both edges for the first mode of vibrations with a growing crack at mid-span

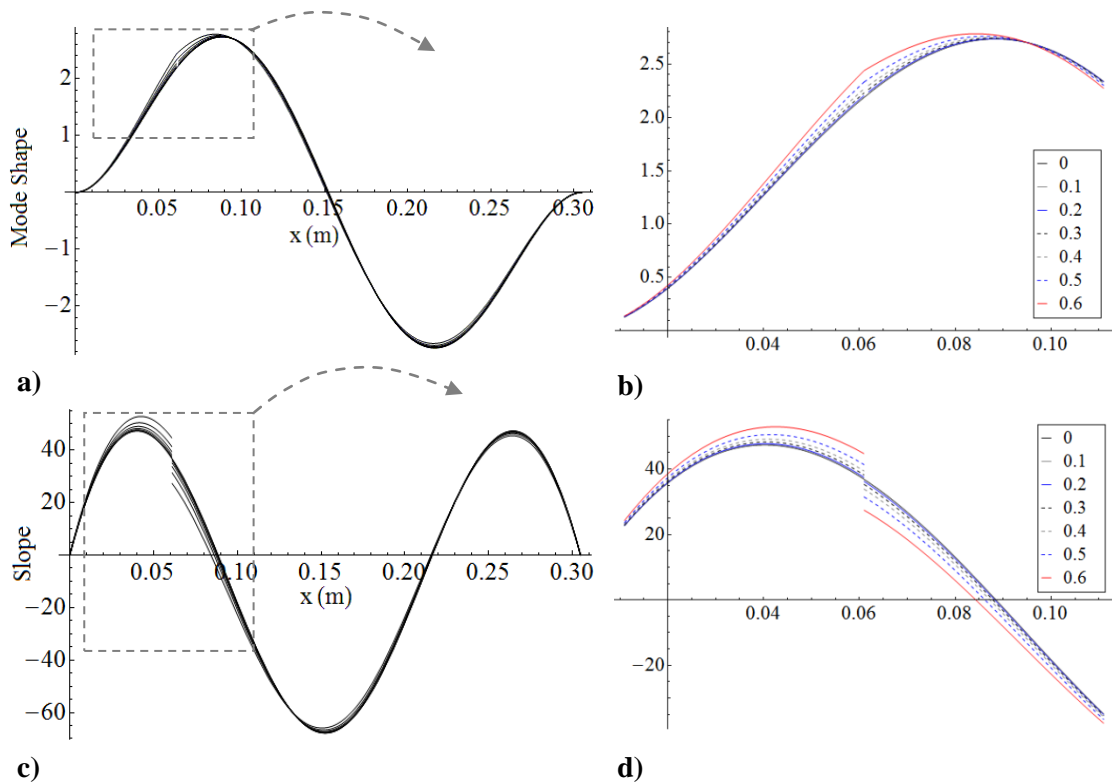


Figure 5.13. a), b) Mode shapes, c), d) slope, of a clamped beam on both edges for the second mode of vibrations with a growing crack at $0.2L$

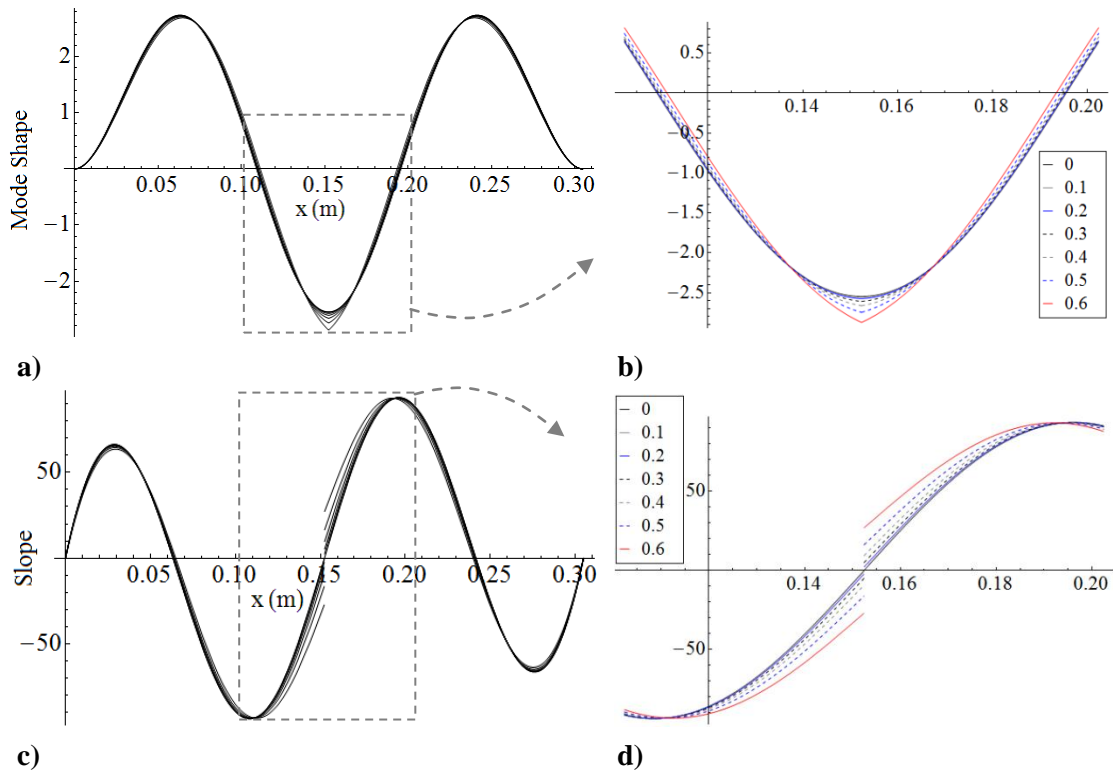


Figure 5.14. a), b) Mode shapes, c), d) slope, of a clamped beam on both edges for the third mode of vibrations with a growing crack at mid-span

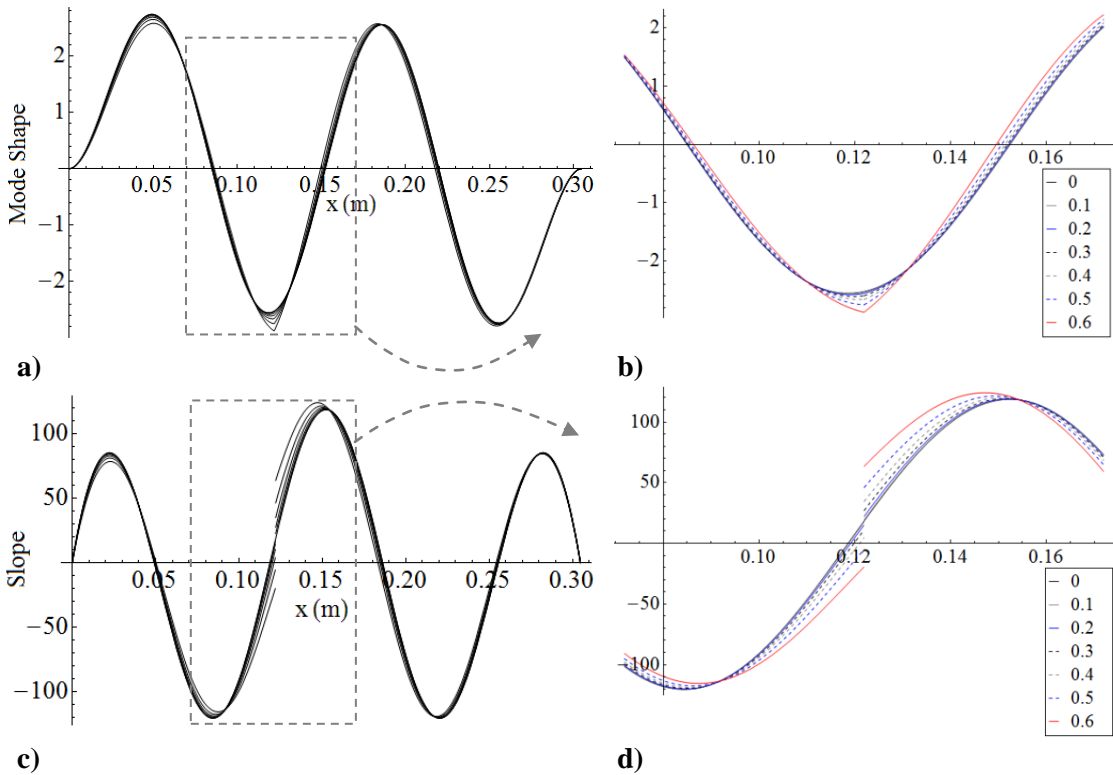
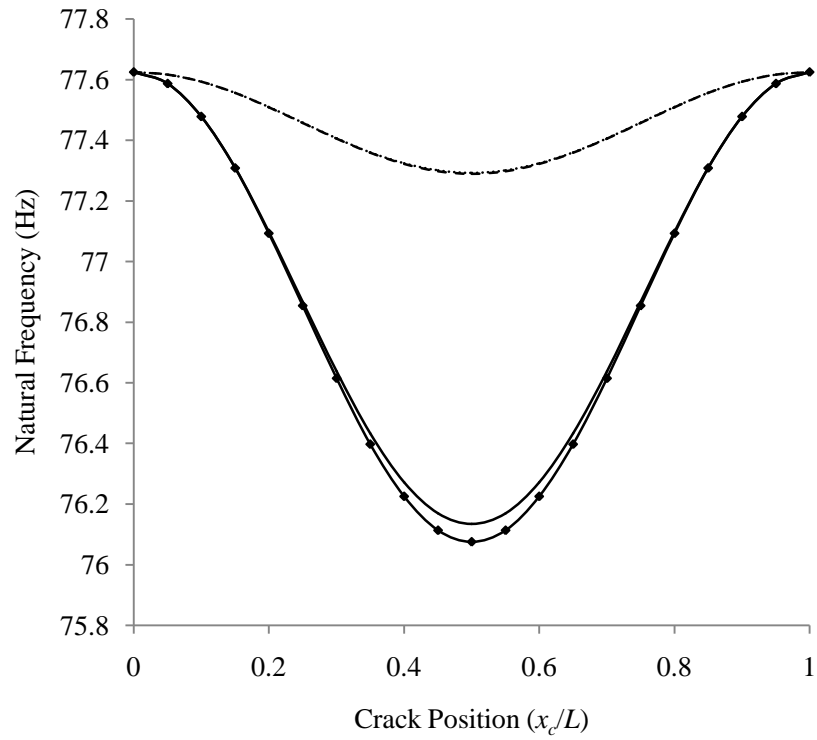
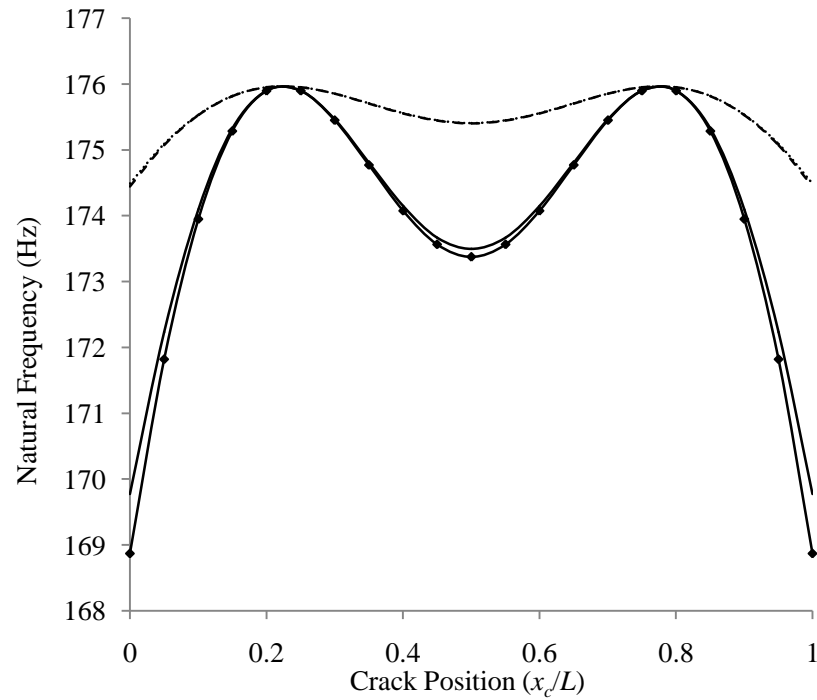


Figure 5.15. a), b) Mode shapes, c), d) slope, of a clamped beam on both edges for the fourth mode of vibrations with a growing crack at $0.4L$

The characteristic equation of free vibrations of the cracked, simply supported or fixed at both ends beam of Figure 5.5 may be analytically formulated following the reference modeling approach (approach a). Substituting the material properties and beam dimensions into the characteristic equation, the wavelength and resonant frequencies of the free vibrations of the beam may be numerically calculated for different crack lengths and positions along the beam. For each depth and position of the crack, the modeling approach proposed in the present paper is used for approximating the resonant frequencies of the free vibrations of the beam. These frequencies of the first three modes of vibrations versus the crack position along the beam are plotted in Figure 5.16-Figure 5.18 and compared for the two modeling approaches. In order to have a better picture of the results, graphs for only two crack depth ratios of $a_c/h_b = 0.2$ and $a_c/h_b = 0.4$ are shown in these figures. In these graphs: a) *round dots* line represents frequencies of the reference modeling approach for crack depth ratio of $a_c/h_b = 0.2$, b) *dash* line represents frequencies of the proposed modeling approach for crack depth ratio of $a_c/h_b = 0.2$, c) *solid* line represents frequencies of the reference modeling approach for crack depth ratio of $a_c/h_b = 0.4$ and d) *solid-square* line represents frequencies of the proposed modeling approach for crack depth ratio of $a_c/h_b = 0.4$.

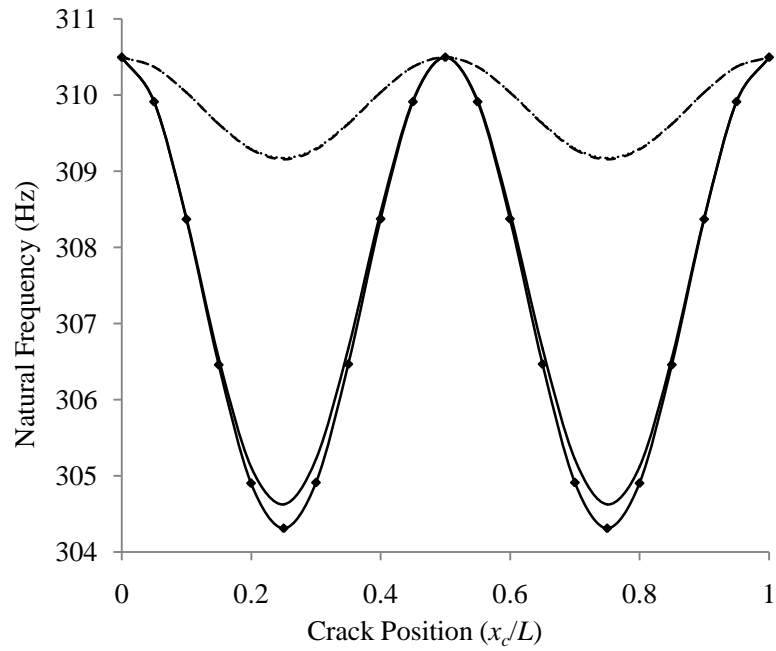


(a)

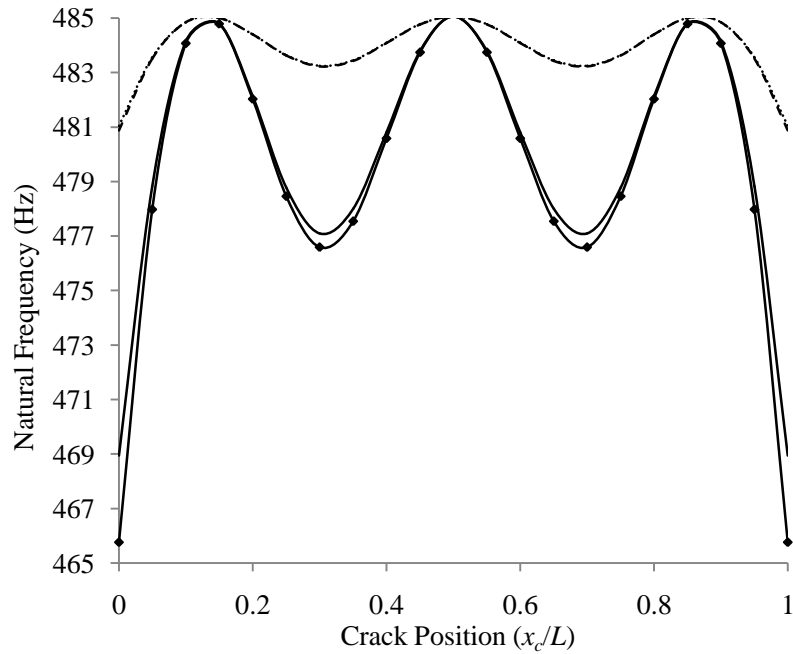


(b)

Figure 5.16. Resonant frequency of the 1st mode of the beam vs crack position along the beam for a) simply supported and b) fixed-fixed boundary conditions. *Round dots* line and *dash* line represent reference and proposed modeling for $a_c/h_b = 0.2$, respectively. *Solid* line and *solid-square* line represent reference and proposed modeling for $a_c/h_b = 0.4$, respectively

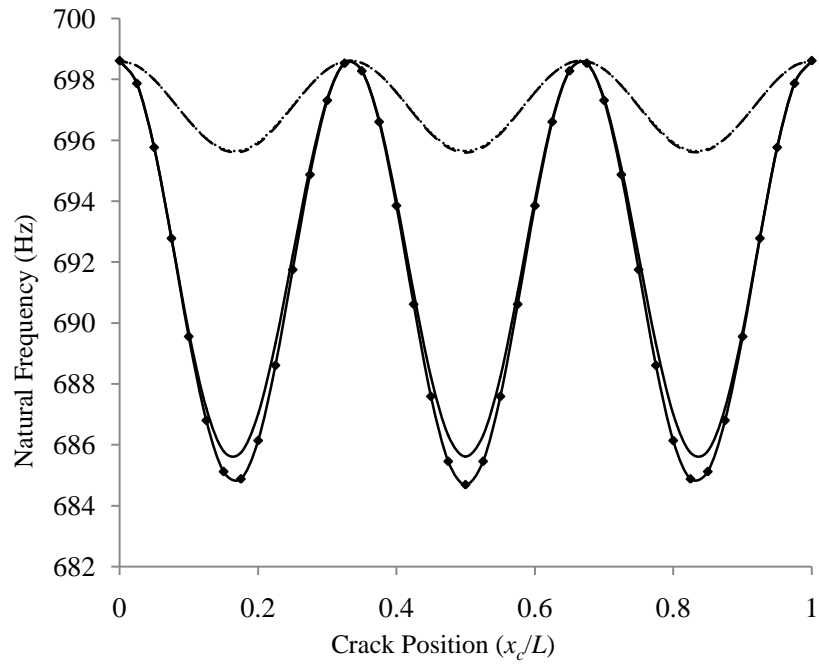


(a)

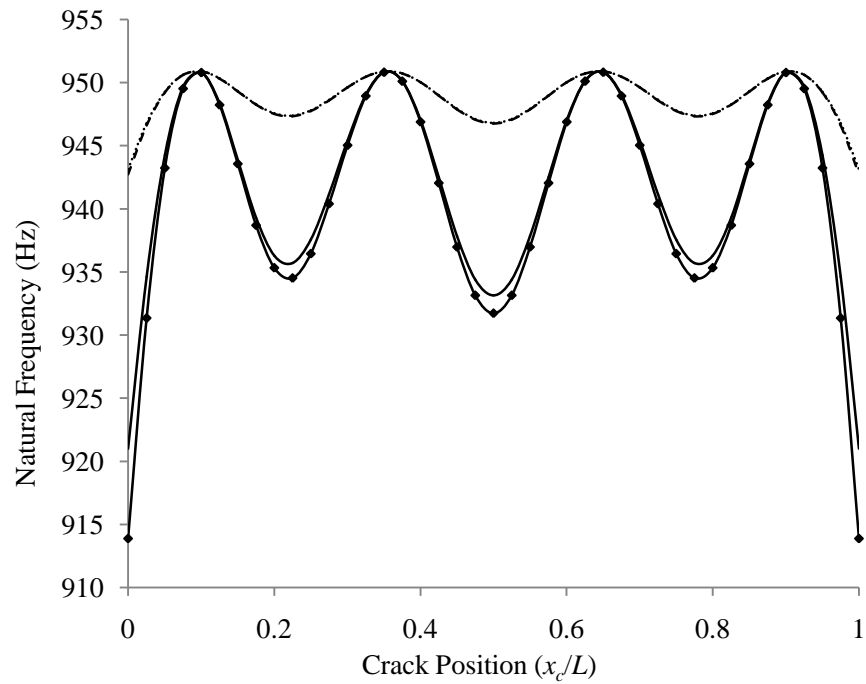


(b)

Figure 5.17. Resonant frequency of the 2nd mode of the beam vs crack position along the beam for a) simply supported and b) fixed-fixed boundary conditions. *Round dots* line and *dash* line represent reference and proposed modeling for $a_c/h_b = 0.2$, respectively. *Solid* line and *solid-square* line represent reference and proposed modeling for $a_c/h_b = 0.4$, respectively



(a)



(b)

Figure 5.18. Resonant frequency of the 3rd mode of the beam vs crack position along the beam for a) simply supported and b) fixed-fixed boundary conditions. *Round dots* line and *dash* line represent reference and proposed modeling for $a_c/h_b = 0.2$, respectively. *Solid* line and *solid-square* line represent reference and proposed modeling for $a_c/h_b = 0.4$, respectively

The values of approximated resonance frequencies of the beam, using the proposed modeling approach, are compared to the ones calculated using the reference model and the amount of error percentage is given in Table 5.3. These values are the maximum error percentages for all crack positions along the length of the beam which happen at the extrema of graphs of Figure 5.16-Figure 5.18. These extrema are the extrema of the bending moment of the mode shapes of the un-cracked beam. Hence, if a crack is located at these positions, with extrema in the second derivative of the un-cracked beam, the effect of crack on the resonance frequencies of the beam is the maximum, according to both modeling attempts (Eqs.(5.18) and (5.42)).

Table 5.3. Error percentage of the resonance frequencies of the beam applying the proposed modeling compared to those of the reference modeling for the first three modes, different crack depth ratios and for simply supported (S) and fixed-fixed (F) support conditions

Mode Number	1			2			3					
End Support	S	F	F	S	F	F	S	S	F	F	F	
x_c/L	0.5	Ends	0.5	0.25 (0.75)	Ends	0.308 (0.692)	0.5	0.167 (0.833)	Ends	0.22 (0.78)	0.5	
Crack depth ratio (a_c/h_b)	0.2	0.00	0.03	0.00	0.00	0.04	0.00	0.01	0.01	0.04	0.01	0.01
	0.4	0.08	0.53	0.07	0.10	0.67	0.10	0.14	0.10	0.77	0.13	0.15
	0.6	0.90	5.58	0.76	1.17	6.06	1.15	1.49	1.15	5.74	1.30	1.62

Table 5.3 gives the error percentage for three crack depth ratios of 0.2, 0.4 and 0.6. The modeling of a crack as a rotational spring with the resultant compliance of the crack as formulated in Eq. (5.10) is applicable to crack depth ratios of $a_c/b \leq 0.6$, with a 0.2% accuracy [103]. Crack depth ratio of 0.6 is, therefore, chosen to find the maximum possible error between the two modeling approaches. The error for the two crack depth ratios of 0.2 and 0.4 are also presented for discussing the accuracy of the proposed approximation as the crack grows.

It is shown in Table 5.3 that for the crack depth ratio of 0.2, the two modeling approaches match well with a very small error percentage of less than 0.06% for all crack locations and support conditions for the first three vibration modes. The error percentage

increases as the crack grows in depth, yet for the crack depth ratio of 0.4 remains less than 0.15% for all crack locations, except for the ends of a fixed beam. The percentage of the error for the crack located at the ends of a fixed beam is the highest for all modes and crack depth ratios, as shown in Table 5.3. The effect of presence of the crack on the resonance frequency of a fixed beam is also the highest when the crack is located at the ends of the beam. This is due to the fact that if a crack is located at the ends of a fixed-fixed beam, as the crack grows, the presence of the crack changes the boundary conditions of the beam. In other words, as the crack grows at one of the ends of a fixed-fixed beam, support conditions of the beam alter more towards the fixed-free conditions. This shift in the support conditions drastically changes the mode shapes of the un-cracked beam. Therefore, the initial choice of mode shapes of a fixed-fixed beam for the Rayleigh-Ritz approximation results in higher errors when the crack is located at the ends of the beam. The effect of presence of the crack at the ends of a fixed beam is higher because this effect is proportional to the bending moment of the beam at the location of the crack. At the location of a fixed support, this bending moment is non-zero. As the crack grows, however, the support conditions at the cracked end become more similar to a free end with zero bending moments. Therefore, the amount of the second derivative of the mode shapes changes at the place of the crack if the growing crack is located near one of the ends of a fixed-fixed beam. This is not the case for a simply supported beam due to the fact that a pinned and a free end of the beam both imply a zero bending moment at the support. Therefore, a change in the support condition from pinned to free does not have an effect on the second derivative of the beam mode shapes and hence on the resonant frequency of the cracked beam.

For the third mode of vibrations, other than the crack located at the ends of the fixed beam, the approximation error is small for all crack locations and beam supports and is much less than 2%. Therefore, except for the crack located at the ends of a fixed-fixed beam, the proposed modeling approach is numerically shown to result in a very small error percentage for crack depth ratios of less than 0.6 and the first three vibration modes. For higher modes of vibration, numerical analysis shows that the error percentage of the natural frequencies of the first five modes for the simply supported and fixed-fixed beams is similar to that of the first three modes given in Table 5.3. It is also seen that

there is a good correlation between the calculated frequencies of both modeling approaches for a simply supported beam at mode numbers higher than five. For a fixed-fixed beam, however, the accuracy of the proposed modeling decreases as the error percentage becomes large for mode numbers higher than five.

5.3.2. The Effect of Temperature-dependent Material Properties on the Resonant Frequencies of the Beam

As mentioned earlier in section 5.2.2, one of the motivations of considering the effect of temperature variations is to investigate and to quantify how temperature variations affect the health monitoring results. In most of the health monitoring applications, continuous measurements of the resonant characteristics of the system are not required and only a limited number of scheduled measurements would suffice. Therefore, temperature variations may be considered as steady-state. This may be simplified as a uniform, time-independent temperature distribution inside the beam. If this temperature distribution is independent of the coordinate along the depth of the structure (non-varying along the depth) the sole effect of temperature variations on the vibration characteristics of the system will be seen through the change in the material properties. Considering the Euler-Bernoulli beam of Figure 5.19 under thermal loadings and assuming a uniformly distributed temperature inside the beam (independent of the coordinates), the effect of temperature on the resonant frequencies of the cracked beam is studied and the results are given in the following.

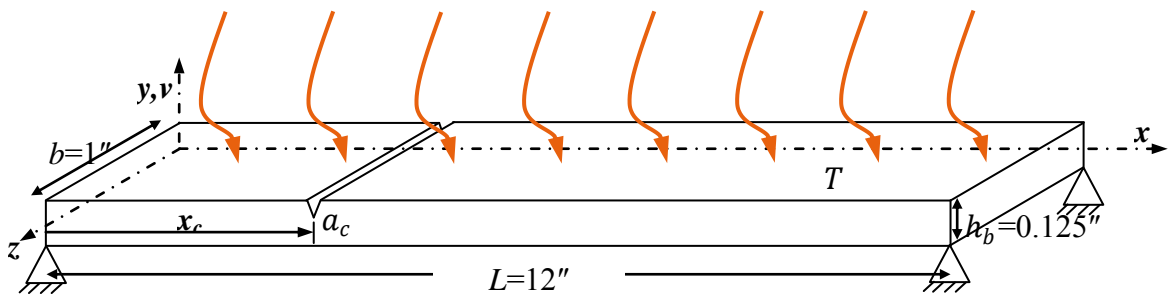


Figure 5.19. Schematic of the cracked beam under steady-state temperature distributions

The variations of the first two resonant frequencies are shown for a simply supported beam with different crack depth ratios at temperature set point of 20°C, as the

reference (grey lines in Figure 5.20 and Figure 5.21). The variations of these frequencies are also shown for two other temperature set points of 40°C and 60°C and for the intact beam and the beam with a crack of 0.4 depth ratio.

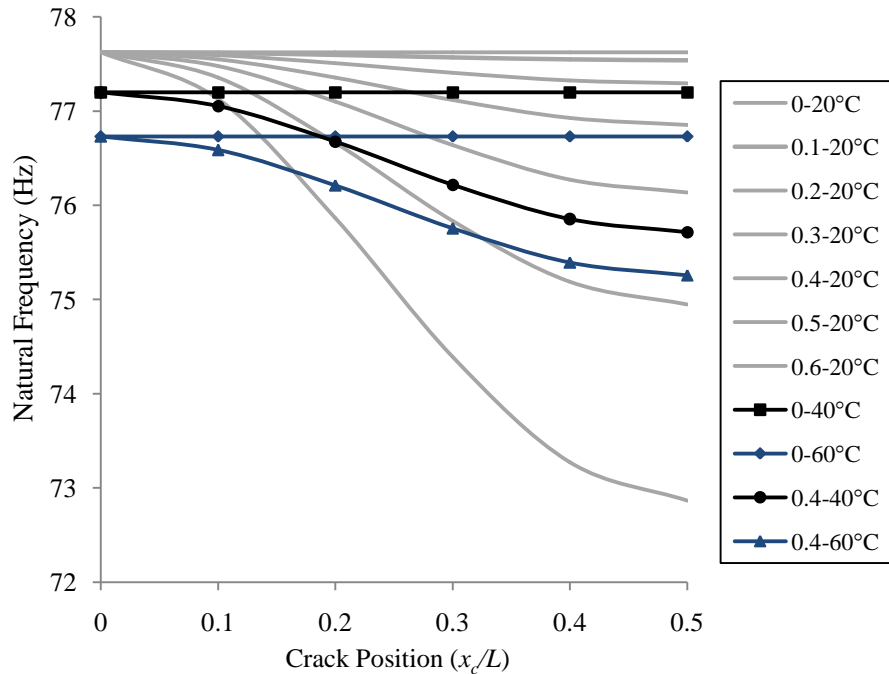


Figure 5.20. Change in the resonant frequency of the first mode of vibrations of a simply supported beam for different crack depth ratios and positions and for different temperature set points

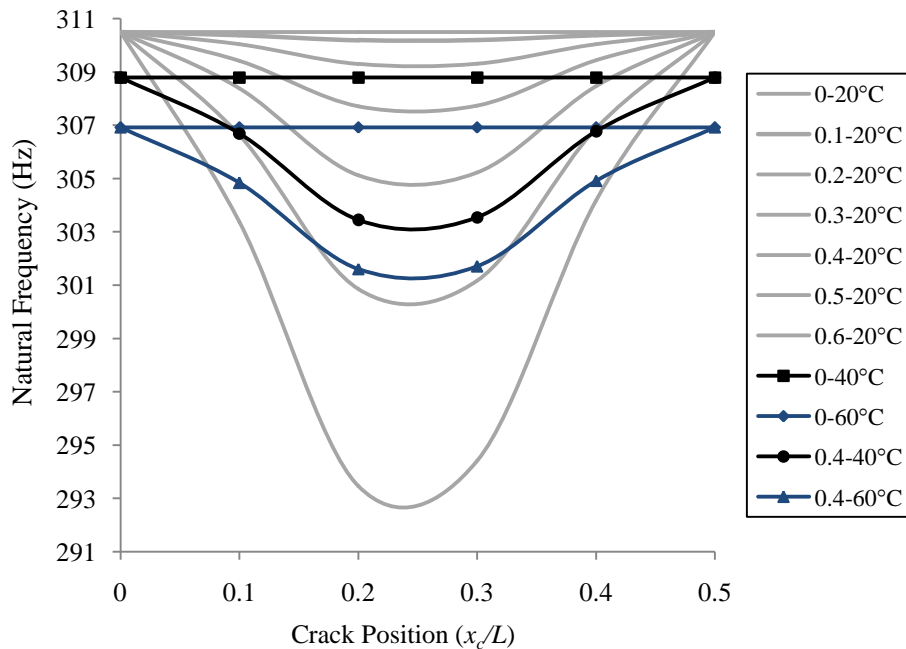


Figure 5.21. Change in the resonant frequency of the second mode of vibrations of a simply supported beam for different crack depth ratios and positions and for different temperature set points

Similarly, the variations of these frequencies are given for a clamped-clamped beam as shown in Figure 5.22 and Figure 5.23.

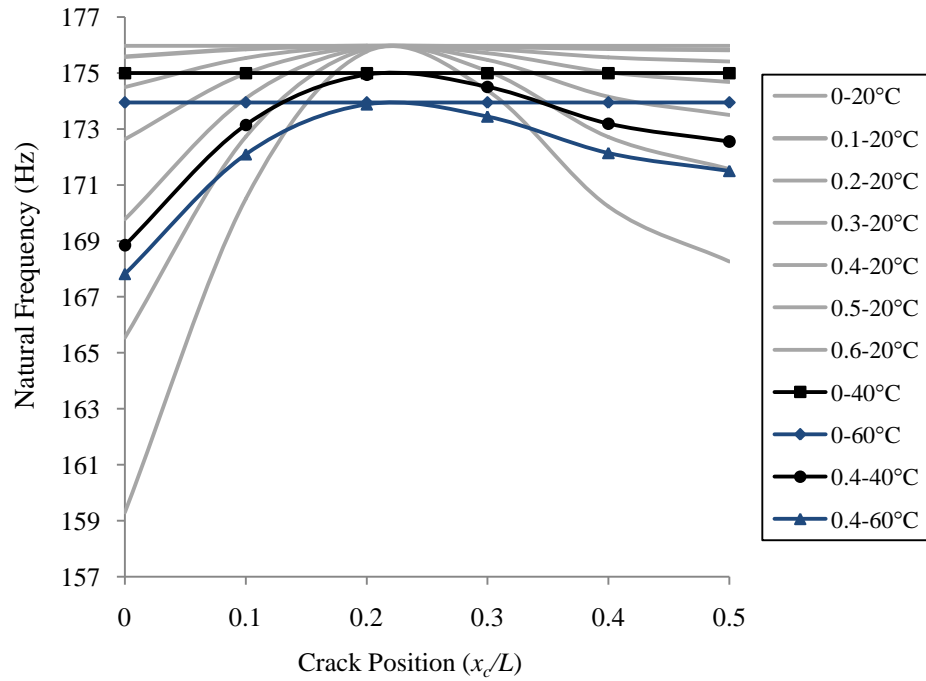


Figure 5.22. Change in the resonant frequency of the first mode of vibrations of a clamped-clamped beam for different crack depth ratios and positions and for different temperature set points

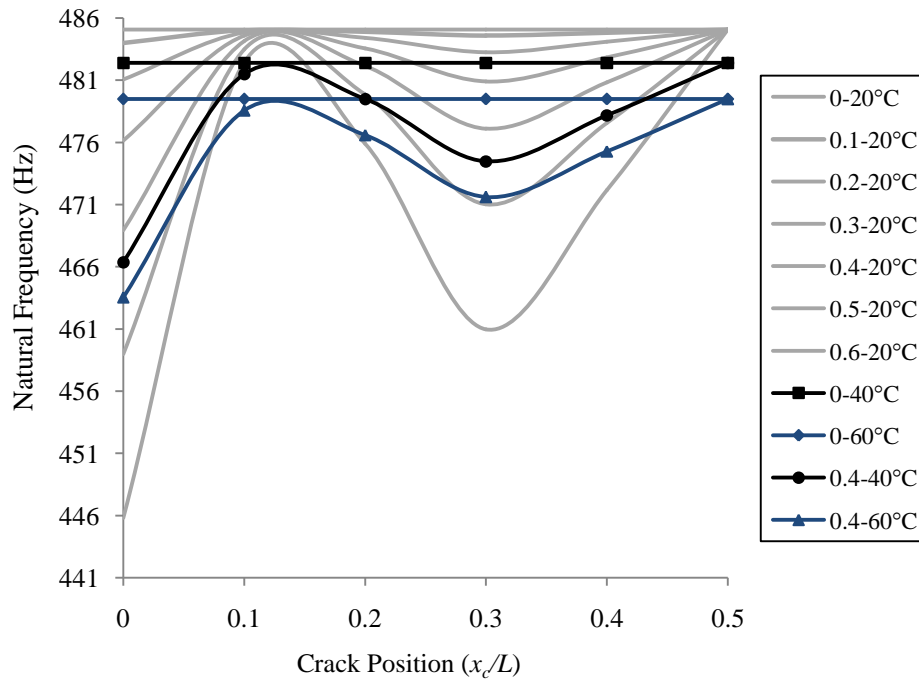


Figure 5.23. Change in the resonant frequency of the second mode of vibrations of a clamped-clamped beam for different crack depth ratios and positions and for different temperature set points

The only temperature-dependent material property considered here, as mentioned before, is the modulus of elasticity of the beam as given in Table 4.1. The resonant frequencies of the cracked beam were shown, earlier in this chapter, to be related to the frequency parameter of γ_i as $\omega_i = \gamma_i^2 \sqrt{\frac{E_b I}{\rho_b A}}$. The frequency parameter is independent of the material properties and only depends upon the crack properties and dimensions and support conditions of the beam. Therefore, the resonant frequencies of the cracked beam are proportional to the square root of the modulus of elasticity of the beam, as long as the beam dimensions and crack properties are kept unchanged.

Assuming the reference temperature (for calculations of the frequency drop) is 20°C and the frequency measurements are done at a higher temperature set point, the amount of resonant frequency drop will be larger than that measured at the reference temperature for different crack specifications. The temperature-resultant frequency drop is listed in Table 5.4-Table 5.7 for two different temperature set points of 40°C and 60°C and for the first two modes of a simply supported Euler-Bernoulli beam as well as the beam clamped at both ends.

It is observed from these tables that the effect of variations in the temperature-dependent material properties is more dominant for a beam that is fixed at both ends compared to a simply supported beam. Moreover, assuming that the smallest detectable crack is considered to be one that shifts the natural frequency by at least half of a hertz [7] (i.e. the health monitoring setup considers half a Hz of frequency drop as presence of a damage), less than 20°C of increase in temperature would be seen as presence of a damage in the structure, while there exist no damage, when monitoring the change in the first resonant frequency.

Table 5.4. The amount of frequency drop for a the first mode of a cracked beam at 40°C compared to the reference point of 20°C and for two support conditions

Frequency Difference		Simply Supported						Clamped-Clamped					
		Crack Position (x_c/L)						Crack Position (x_c/L)					
		0	0.1	0.2	0.3	0.4	0.5	0	0.1	0.2	0.3	0.4	0.5
Crack Depth Ratio (a_c/b)	0	0.4	0.4	0.4	0.4	0.4	0.4	1.0	1.0	1.0	1.0	1.0	1.0
	0.1	0.4	0.4	0.5	0.5	0.5	0.5	1.3	1.1	1.0	1.0	1.1	1.1
	0.2	0.4	0.5	0.5	0.6	0.7	0.8	2.4	1.4	1.0	1.1	1.4	1.5
	0.3	0.4	0.5	0.7	0.9	1.1	1.2	4.3	1.9	1.0	1.2	1.9	2.2
	0.4	0.4	0.6	0.9	1.4	1.8	1.9	7.1	2.8	1.0	1.5	2.8	3.4
	0.5	0.4	0.7	1.4	2.2	2.8	3.1	11.3	4.2	1.1	1.9	4.2	5.3
	0.6	0.4	0.9	2.2	3.6	4.8	5.2	17.5	6.4	1.2	2.6	6.7	8.6

Table 5.5. The amount of frequency drop for a the first mode of a cracked beam at 60°C compared to the reference point of 20°C and for two support conditions

Frequency Difference		Simply Supported						Clamped-Clamped					
		Crack Position (x_c/L)						Crack Position (x_c/L)					
		0	0.1	0.2	0.3	0.4	0.5	0	0.1	0.2	0.3	0.4	0.5
Crack Depth Ratio (a_c/b)	0	0.9	0.9	0.9	0.9	0.9	0.9	2.0	2.0	2.0	2.0	2.0	2.0
	0.1	0.9	0.9	0.9	0.9	1.0	1.0	2.4	2.1	2.0	2.1	2.1	2.2
	0.2	0.9	0.9	1.0	1.1	1.2	1.2	3.5	2.5	2.0	2.1	2.4	2.6
	0.3	0.9	1.0	1.2	1.4	1.6	1.7	5.3	3.0	2.1	2.3	3.0	3.3
	0.4	0.9	1.0	1.4	1.9	2.2	2.4	8.1	3.9	2.1	2.5	3.8	4.5
	0.5	0.9	1.2	1.8	2.7	3.3	3.5	12.3	5.2	2.1	2.9	5.2	6.4
	0.6	0.9	1.4	2.6	4.1	5.2	5.6	18.5	7.4	2.2	3.6	7.7	9.6

Table 5.6. The amount of frequency drop for a the second mode of a cracked beam at 40°C compared to the reference point of 20°C and for two support conditions

Frequency Difference		Simply Supported						Clamped-Clamped					
		Crack Position (x_c/L)						Crack Position (x_c/L)					
		0	0.1	0.2	0.3	0.4	0.5	0	0.1	0.2	0.3	0.4	0.5
Crack Depth Ratio (a_c/b)	0	1.7	1.7	1.7	1.7	1.7	1.7	2.7	2.7	2.7	2.7	2.7	2.7
	0.1	1.7	1.8	2.0	2.0	1.8	1.7	3.7	2.7	2.8	3.1	2.9	2.7
	0.2	1.7	2.2	2.9	2.9	2.2	1.7	6.7	2.9	3.3	4.5	3.6	2.7
	0.3	1.7	2.8	4.5	4.4	2.8	1.7	11.5	3.1	4.2	6.8	4.9	2.7
	0.4	1.7	3.8	7.1	7.0	3.7	1.7	18.7	3.6	5.6	10.6	6.9	2.7
	0.5	1.7	5.6	11.3	11.0	5.3	1.7	28.6	4.2	7.9	16.6	10.1	2.7
	0.6	1.7	8.8	18.7	17.7	8.0	1.7	41.7	5.3	11.8	26.6	15.5	2.7

Table 5.7. The amount of frequency drop for a the second mode of a cracked beam at 60°C compared to the reference point of 20°C and for two support conditions

Frequency Difference		Simply Supported						Clamped-Clamped					
		Crack Position (x_c/L)						Crack Position (x_c/L)					
		0	0.1	0.2	0.3	0.4	0.5	0	0.1	0.2	0.3	0.4	0.5
Crack Depth Ratio (a_c/b)	0	3.6	3.6	3.6	3.6	3.6	3.6	5.6	5.6	5.6	5.6	5.6	5.6
	0.1	3.6	3.7	3.9	3.9	3.7	3.6	6.6	5.6	5.8	6.0	5.8	5.6
	0.2	3.6	4.0	4.8	4.8	4.0	3.6	9.6	5.8	6.2	7.4	6.5	5.6
	0.3	3.6	4.6	6.3	6.3	4.6	3.6	14.4	6.1	7.1	9.7	7.8	5.6
	0.4	3.6	5.7	8.9	8.8	5.6	3.6	21.5	6.5	8.5	13.5	9.8	5.6
	0.5	3.6	7.4	13.1	12.8	7.2	3.6	31.3	7.1	10.7	19.5	13.0	5.6
	0.6	3.6	10.6	20.4	19.5	9.8	3.6	44.4	8.2	14.7	29.4	18.4	5.6

The amount of resonant frequency drop gets much larger for higher modes of vibrations of the beam as shown in Table 5.6 and Table 5.7.

5.3.3. The Effect of a Transient Temperature Distribution on the Vibratory Response of a Cracked Beam

The vibration response of a cracked beam under transient temperature variations was studied in section 5.2.4. Different temperature variations scenarios were considered and the time response of the cracked beam was formulated. In most of the structural health monitoring applications with a transient temperature, like spacecraft and aircraft, temperature variations happen only through the depth of the structure and will be

homogeneous along the length, i.e. $T(y, t)$. In these cases, the temperature effect on the vibratory response of the system will be caused through alterations in the material properties as well as thermal stress generation inside the structure. In this section, the effect of a temperature variation that is harmonic with respect to time and independent of the coordinate along the length and the width of the beam is studied on the time response of an Euler-Bernoulli beam with a surface-bonded PZT, as shown in Figure 5.24. The self-sensing PZT actuator is specifically useful in controlling the thermally induced vibrations of the beam structure. In this section, however, the controller output voltage of the PZT actuator is not studied and the PZT patch is considered to be used merely as the sensor. The variations in the output voltage of the PZT sensor, as studied here, will be applicable to the controller design for future applications.

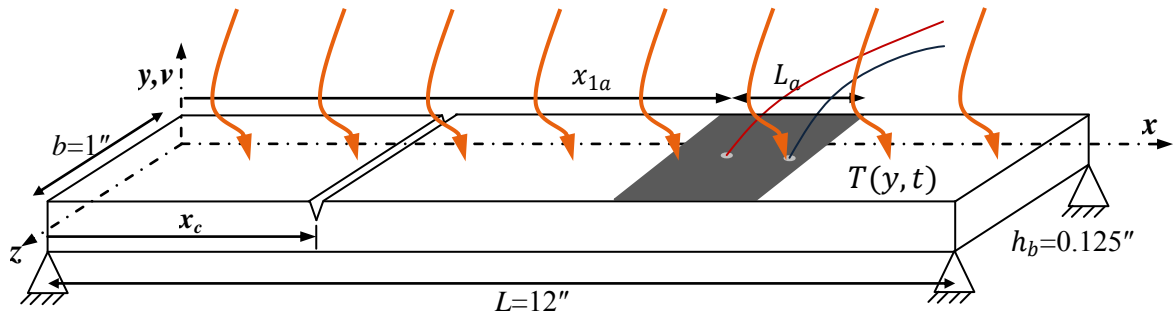


Figure 5.24. Schematic of the cracked beam with the surface-bonded PZT layer

The PZT sensing patch considered in the following numerical studies is assumed to be PSI-5A4E [2] and to be as wide as the beam, located at $0.75L$ (9") and be $0.05L$ (0.6") long. The thickness and material properties of this PZT patch is listed in Table 5.8.

Table 5.8. Material properties of the PSI-5A4E PZT [2]

Properties	
Modulus of elasticity $c_{11}^{E,T}$ (Pa)	6.6×10^{10}
Density ρ_a (kg/m ³)	7800
Piezoelectric strain constant d_{31} (m/Volt)	-190×10^{-12}
Capacitance (F)	315×10^{-9}
Pyroelectric constant P_3^e [26]	4.078×10^{-4}
Thermal expansion coefficient α_t^p (m/m °C)	4×10^{-6}
Thickness h_a (m)	0.267 (0.0105")

Temperature distribution is assumed to be as given in Eq. (5.116) with $T_x(x) = 1$, $T_y(y) = 10y$ and the frequency of $\Omega_T = \pi/2$ Hz. Considering the first ten vibration modes of the beam, the error is numerically calculated for the displacement of the vibrating beam at $x = 0.55L$ (6.6") if the correction term in the thermal loading due to the presence and growth of the crack is ignored in the formulations. This error is calculated for different crack positions and depth ratios and is shown in Figure 5.25 and Figure 5.26 for the simply supported beam of Figure 5.24. The error is calculated for the displacement at $x = 0.55L$ instead of the mid-span due to the fact that the crack is located at different locations from very close to zero (start of the beam) to the mid-span of the beam and the point for measuring the displacement was chosen to be different from the location for the crack.

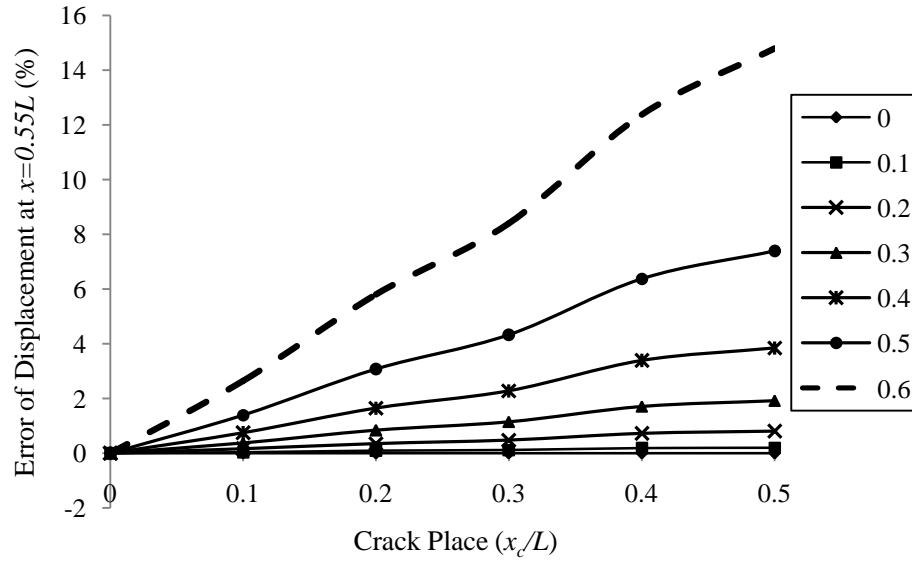


Figure 5.25. The error percentage for a growing crack at different locations along the beam

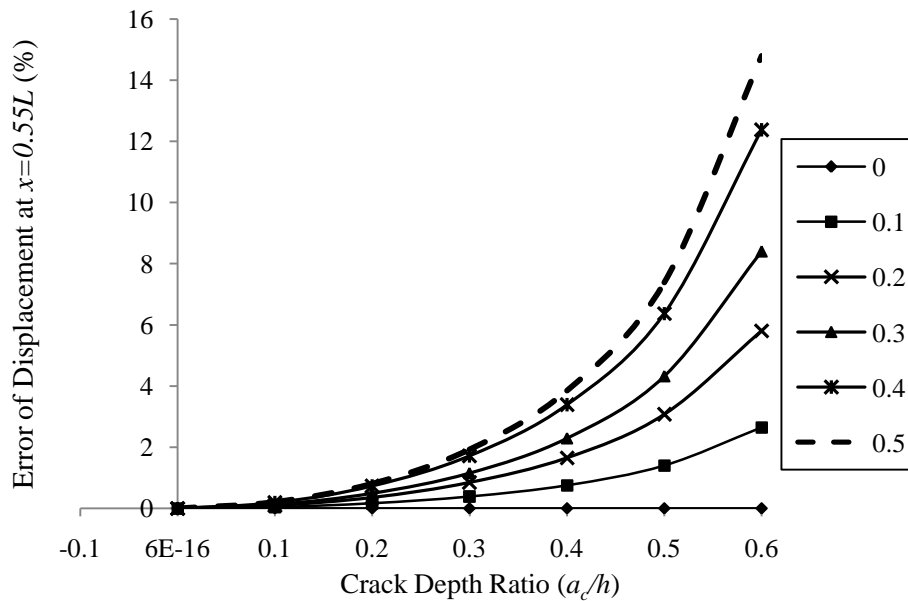


Figure 5.26. The error percentage for a growing crack at different locations along the beam

The displacement ratio of the cracked beam under thermal loading at $x = 0.55L$ over the applied thermal moment is shown in Figure 5.27 as a function of time for a growing crack located at the mid-span of the beam. It is seen from this plot that amplitude of the vibrations of the beam reduces as the crack grows through the depth of the beam. The percentage of reduction in this amplitude is as shown by the thick-dashed line in Figure 5.26.

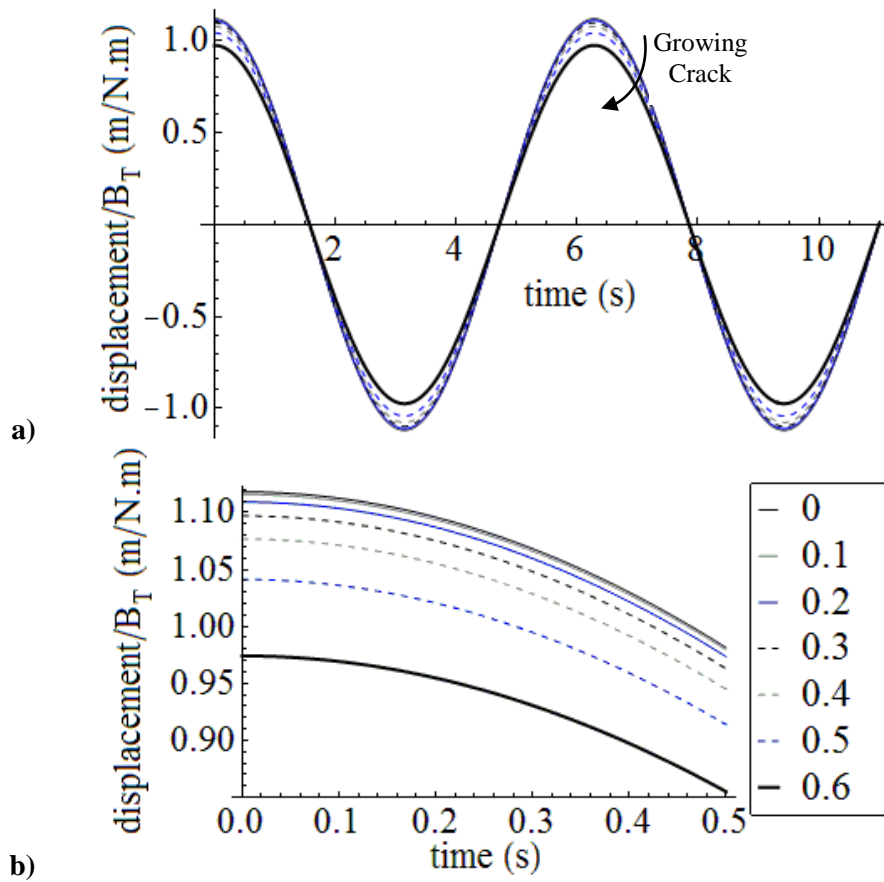


Figure 5.27. Displacement to thermal moment ratio of the simply supported beam of Figure 5.5 with the growing crack at the mid-span, for different crack depth ratios

The displacement ratio of the cracked beam under thermal loading at $x = 0.55L$ over the applied thermal moment is shown in Figure 5.28 as a function of time for a crack with the depth ratio of 0.6 located at three different locations along the beam. It is seen from this plot that as the crack gets closer to the mid-span of the beam, the effect of temperature and crack presence gets more noticeable and the displacement of the beam gets smaller in the amplitude. The percentage of reduction in this amplitude is as shown by the thick-dashed line in Figure 5.25.

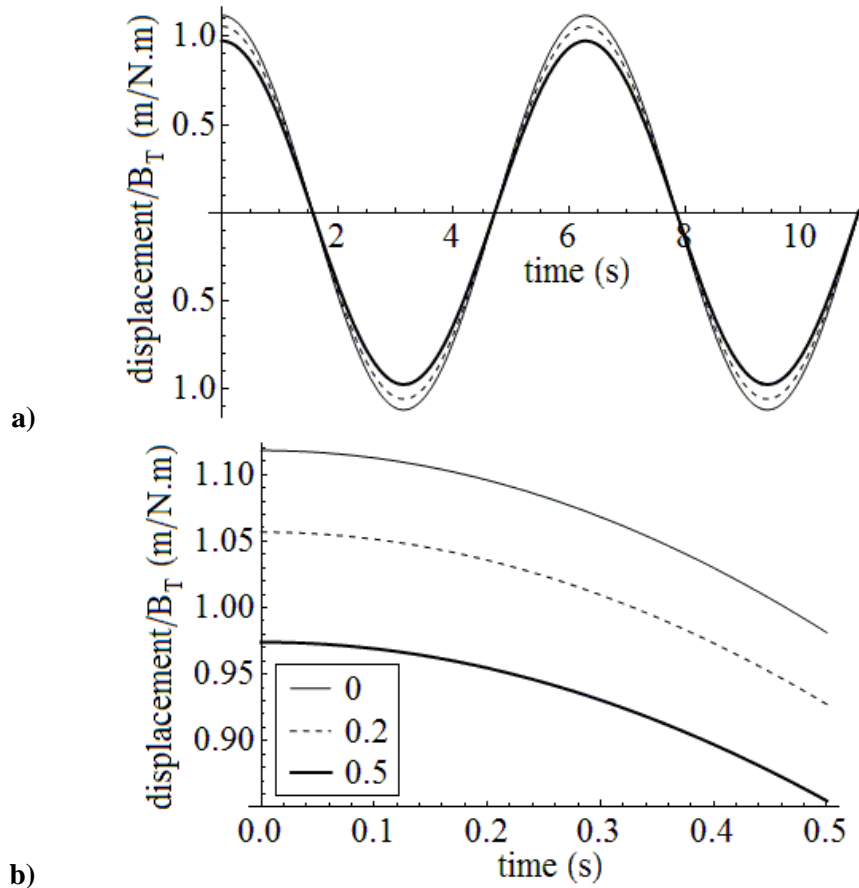


Figure 5.28. Displacement to thermal moment ratio of the simply supported beam with a crack with 0.6 depth ratio at different locations along the length of the beam

The cracked beam studied in the present numerical analysis is assumed to have a PZT sensing layer bonded to the top surface. The amount of output voltage of this sensor and the variations in this voltage for different crack parameters and temperature variations is also an important indicator to be studied. It is also important to note that the amount of output voltage is proportional to the amount of slope at the two ends of the PZT patch as well as the PZT material parameters. For the PZT location given in Figure 5.24 and for a growing crack located at the mid-span of the beam, the output voltage of the PZT sensor varies as shown in Figure 5.29.

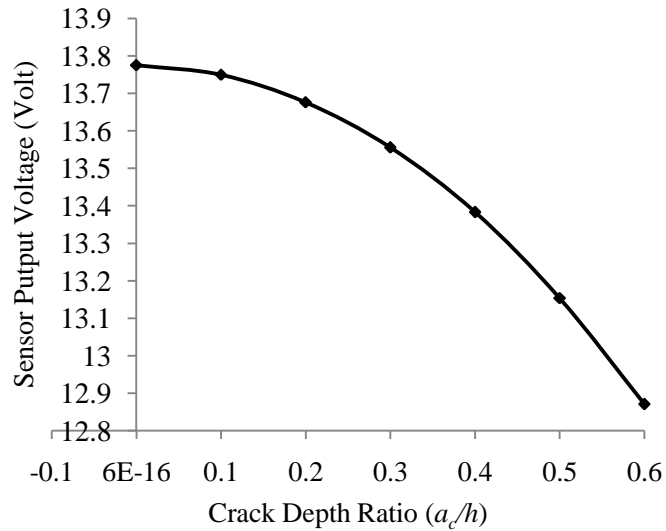


Figure 5.29. Voltage output of the PZT sensor for the simply supported beam under thermal loading with a growing crack at mid-span

The amount of pyroelectric voltage output of the PZT sensor is proportional to the material properties and dimensions of the PZT as well as the amount of temperature variations. For the temperature variations studied here, the PZT pyroelectric effect accounts for almost 18% (≈ 2.5 Volts) of the output voltage in the absence of the crack.

It is important to note that the total amount of output voltage of the PZT sensor is the total of voltage generated in the PZT due to the displacements of the beam and the voltage generated in the PZT due to the PZT pyroelectric effect. In the controller design applications used for vibration suppressions of the beam, however, only the displacement-related output voltage should be used in the feedback design.

The above-mentioned numerical results are derived assuming that the temperature-dependent material properties of the beam, here the modulus of elasticity, do not change. In other words, the amount of temperature variations is assumed to be small. Considering the time-dependent material properties of the beam in the formulations of the stiffness and mass matrices of the beam would make the analysis of the time-response of the structure a rather complex problem. It was earlier shown in section 5.3.2 of the numerical analysis that the variations in the temperature-dependent modulus of elasticity of the beam cause a change in the resonant frequency of the beam. In order to include the effect of both thermal stresses and temperature-dependent material properties of the beam in the study of the effect of temperature on the dynamic response of a cracked beam, it is

assumed that the temperature is raised from the reference point of 20°C to the current temperature of 100°C. This temperature set point is assumed to be the steady-state amount of temperature. The temperature is then fluctuated around this steady-state temperature for the amount considered earlier in this section. The displacement ratio of the cracked beam under this thermal loading at $x = 0.55L$ over the applied thermal moment is given for the beam without any damage as well as the beam with a crack of 0.6 depth ratio and shown in Figure 5.30.

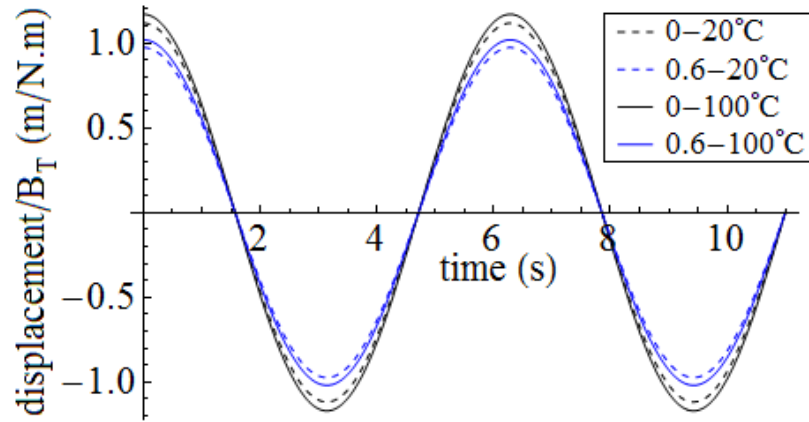


Figure 5.30. Displacement to thermal moment ratio of the simply supported beam with a crack at mid-span of the beam and for two different temperature set points and crack depth ratios

It may be observed from these results that considering the material properties variations as a function of temperature causes a change in the amplitude of vibrations of the beam as well as the resonant frequency of the beam's vibrations. This effect, however, is more dominantly observed through a change in the resonant frequencies of the vibrating beam rather than the change in the amplitude of.

5.4. Chapter Summary

The vibratory response of an Euler-Bernoulli beam with two different support conditions of simply supported and clamped-clamped was studied in this chapter. The beam was assumed to have a single, non-breathing crack on one side and was assumed to be under thermal loading. In the first part of the modeling, free vibrations of the cracked beam without considering the effect of temperature fluctuations was studied and the

mode shapes of the cracked beam were formulated using two different approaches. Rayleigh-Ritz approximation was applied in the proposed approach for modeling the mode shapes of the cracked beam. In this approach, the total strain energy of the uncracked beam was modified by subtracting the amount of energy released at the place of the growing crack due to the crack-resultant additional rotation. This approximate modeling approach was shown to match well with the results of the cracked-beam modeling available in literature for different crack parameters and beam support conditions.

The effect of temperature variations on the vibratory response of the cracked beam was then studied considering the two effects of variations in the temperature-dependent material properties and the induced thermal stresses inside the beam. Increasing the temperature inside the beam and, as a result, decreasing the modulus of elasticity of the beam was shown to cause a drop in the natural frequency of the cracked beam as well as a reduction in the amplitude of the beam time-response to transient temperature fluctuations. The amount of these changes was shown to be dependent upon the temperature distribution function and crack-related parameters (such as depth and position along the beam). As an example, an Euler-Bernoulli beam made of aluminum and with dimensions of 12"×1"×1/8" was considered with a uniformly distributed temperature inside the beam (independent of the coordinates). It was shown that for this special temperature distribution, which applies to a wide range of applications in the area of SHM, the sole effect of temperature variations on the vibration characteristics of the beam would be seen through the change in the material properties. It was also observed from the numerical analysis that the effect of variations in the temperature-dependent material properties is more dominant for a beam that is fixed at both ends compared to a simply supported beam. For the above-mentioned beam, the amount of drop in the natural frequency of the first mode of vibrations of the simply supported beam was 0.02 Hz/°C, in the absence of a damage, while this amount of frequency drop was increased to 0.05 Hz/°C for a similar beam fixed at both ends. Therefore, assuming that the smallest detectable crack is considered to be one that shifts the natural frequency by at least half of a hertz, it was shown that less than 20°C of increase in temperature would be seen as presence of a damage in a clamped-clamped beam, while there exist none, when

monitoring the change in the first resonant frequency. The amount of resonant frequency drop due to temperature variations was shown to get doubled for higher modes of vibrations of the beam (both simply supported and clamped-clamped).

The effect of thermal stress formation was included here by modifying the axial stress inside the beam. This was done by applying the theory of thermal stresses, Euler-Bernoulli beam assumptions and the linear strain-displacement relation to the formulation of the stress and elastic and kinetic energies of the beam. The presence of an active piezoceramic (PZT) sensing layer was also included through modifications of the structural matrices and by considering the electro-mechanical coupling between the PZT and the beam. Lagrange equations were then applied to formulate the coupled set of temporal equations for the time-response of the cracked beam and the sensing output of the PZT layer. It was shown that growth of a single fatigue crack inside a beam that undergoes temperature fluctuations and thermal loadings alters the dynamic response of the vibrating beam, in particular the displacement of the beam at the $0.55L$ point. The amount of this change was shown to depend upon the position of the crack along the length of the beam as well as the crack depth and could be as high as 14%. The sensing (output) voltage of the PZT layer was also shown to be affected by the presence and growth of a single crack inside the beam. Change in the output voltage due to the presence of a growing crack and temperature fluctuations was shown to vary depending on the specifications of the crack. Growth of a single fatigue crack at the mid-span of a simply-supported beam was shown to cause a 7% drop in the sensing voltage of the PZT if the temperature profile was kept non-varying.

CONCLUSIONS AND FUTURE WORK

Structural Health Monitoring (SHM) is the implementation of damage detection and characterization algorithms using *in vitro* sensing and actuation for rapidly determining faults in structural systems before the damage leads to catastrophic failure. SHM systems provide near real time information on the state of the integrity of civil, mechanical and aerospace structures. A roadblock in implementing SHM systems in practice is the possibility of false positives introduced by environmental changes, such as temperature variations, often misinterpreted as damage. The effect of temperature on SHM is not currently understood from first principles, and the present study will provide the fundamental mechanics modeling of temperature effects on SHM methodologies that search for cracks in the structural systems found in civil infrastructure, mechanical and aerospace systems in order to remove this roadblock to implementation.

6.1. Research Summary

The principle objective of the present study was to understand and model how thermal loadings and changes in ambient temperature influence the electrical impedance- and vibration-based SHM procedures used for detecting cracks in structures. To achieve these end goals, the effect of presence and growth of damage (in the form of a single fatigue crack) was initially studied for these SHM methods.

In the first part of the work presented in this dissertation, experimental studies of different mechanical structures of aluminum beams, lug samples and railroad switch bolts were done. The experimental study of the aluminum lug samples and beams was done to propose and examine methods and models for *in situ* interrogation and detection of

damage (in the form of a fatigue crack) in these specimen and to quantify the smallest detectable crack size in aluminum structures. This was done by applying the electrical impedance-based SHM method and using piezoceramic sensors and actuators. In order to better extract the fatigue crack damage features from the measured electrical impedance, the ARX non-linear feature extraction was employed. It was shown that applying this method of feature extraction resulted in observing a trend in the variation of damage index as the number of fatigue cycles increased. From the experimental results provided for the aluminum beam studied here, the damage index calculated using the non-linear feature extraction was shown to remain unchanged up to the 100k fatigue cycles and have a sudden change for the 110k fatigue cycles. The damage index was shown to grow monotonically for the fatigue cycles larger than 110k. This was interpreted as the initiation of a micro-crack inside the beam that has not yet reached a visible state. Such trend in the variation of damage index was not seen when the linear feature extraction was applied. Therefore, the non-linear feature extraction was shown to be helpful in improving the early detection of fatigue cracks in structures compared to the linear method. Using three different input voltages of 0.2, 0.6 and 1.0V of the HP 4194A impedance analyzer, the measured impedances were compared to examine the validity of considering fatigue cracks with non-linear structural behavior. It was shown that as the difference between the two input voltages increase, the correlation between the outputs gets less. This verified the presence of non-linearity in a beam's structure having fatigue cracks. It was later shown that repeating the same set of experiment for a growing saw-cut (which is intuitively assumed to have a linear structural behavior) resulted in close correlation between the outputs for different levels of input voltage.

The electrical impedance-based SHM technique was also applied in monitoring the damage in the form of the loosening of bolted joints in a full-scale railroad switch and the sensitivity of this technique to different levels of loosening of the bolts was investigated. It was experimentally verified that applying the impedance-based SHM technique and using the piezoceramic self-sensing actuators contribute to the detection of loosening of these bolts at an early stage of 25 ft-lbs which corresponds to merely 1/10th of a bolt turn.

The second part of the work presented here was focused on the analytical study and better understanding of the effect of temperature on the vibration-based SHM. This was done by analytical modeling of the vibratory response of an Euler-Bernoulli beam with two different support conditions of simply supported and clamped-clamped and with a single, non-breathing fatigue crack at different locations along the length of the beam. The effect of temperature variations on the vibratory response of the beam structure was modeled by considering the two effects of temperature-dependent material properties and thermal stress formations inside the structure. The inclusion of thermal effects from both of these points of view (i.e. material properties variations and generation of thermal stresses) as independent factors was investigated and justified by studying the formulations of Helmholtz free energy and stresses inside a body. It was shown that to formulate the stresses inside a body for small temperature variations (where temperature variations are much smaller than the initial temperature and the change in the material properties are negligible), the Helmholtz free energy may be approximated around the initial state (of zero strain and initial temperature set point) of the body using the second order Taylor series expansion. The elastic moduli of the body were assumed to be non-varying for this case. For large temperature changes, however, the free energy could be approximated by applying Taylor series expansion around the initial state of zero strain only. Due to the variations in temperature, the elastic constants of the body would no longer be equal to these values at the initial state of the body and were shown to be functions of the temperature inside the body. The effect of temperature on different material properties of aluminum was described as a special example. It was shown that the modulus of elasticity of aluminum varies more dominantly with respect to temperature (1.1% of variations in 20°C) as compared to the Poisson's ratio (0.05% variations in 20°C). It was also noted that the modulus of elasticity varies linearly with respect to time.

The effect of temperature variations on the vibratory response of the cracked beam was then studied considering the two effects of variations in the temperature-dependent material properties and the induced thermal stresses inside the beam. Increasing the temperature inside the beam and, as a result, decreasing the modulus of elasticity of the beam was shown to cause a drop in the natural frequency of the cracked

beam as well as a reduction in the amplitude of the beam time-response to transient temperature fluctuations. The amount of these changes was shown to be dependent upon the temperature distribution function and crack-related parameters (such as depth and position along the beam). As an example, an Euler-Bernoulli beam made of aluminum and with dimensions of 12"×1"×1/8" was considered with a uniformly distributed temperature inside the beam (independent of the coordinates). It was shown that for this special temperature distribution, which applies to a wide range of applications in the area of SHM, the sole effect of temperature variations on the vibration characteristics of the beam would be seen through the change in the material properties. It was also observed from the numerical analysis that the effect of variations in the temperature-dependent material properties is more dominant for a beam that is fixed at both ends compared to a simply supported beam. For the above-mentioned beam, the amount of drop in the natural frequency of the first mode of vibrations of the simply supported beam was 0.02 Hz/°C, in the absence of a damage, while this amount of frequency drop was increased to 0.05 Hz/°C for a similar beam fixed at both ends. Therefore, assuming that the smallest detectable crack is considered to be one that shifts the natural frequency by at least half of a hertz, it was shown that less than 20°C of increase in temperature would be seen as presence of a damage in a clamped-clamped beam, while there exist none, when monitoring the change in the first resonant frequency. The amount of resonant frequency drop due to temperature variations was shown to get doubled for higher modes of vibrations of the beam (both simply supported and clamped-clamped).

The effect of thermal stress formation was included here by modifying the axial stress inside the beam. This was done by applying the theory of thermal stresses, Euler-Bernoulli beam assumptions and the linear strain-displacement relation to the formulation of the stress and elastic and kinetic energies of the beam. The presence of an active piezoceramic (PZT) sensing layer was also included through modifications of the structural matrices and by considering the electro-mechanical coupling between the PZT and the beam. Lagrange equations were then applied to formulate the coupled set of temporal equations for the time-response of the cracked beam and the sensing output of the PZT layer. It was shown that growth of a single fatigue crack inside a beam that undergoes temperature fluctuations and thermal loadings alters the dynamic response of

the vibrating beam. The amount of change in the displacement of the beam at the $0.55L$ point was shown to depend upon the position of the crack along the length of the beam as well as the crack depth and could be as high as 14% for a crack with the depth ratio of 0.6 and located at the mid-span of the beam. The sensing (output) voltage of the PZT layer was also shown to be affected by the presence and growth of a single crack inside the beam. Change in the output voltage due to the presence of a growing crack and temperature fluctuations was shown to vary depending on the specifications of the crack. Growth of a single fatigue crack at the mid-span of a simply-supported beam was shown to cause a 7% drop in the sensing voltage of the PZT if the temperature profile was kept non-varying.

6.2. Contributions of the Research

- The ARX non-linear feature extraction was employed and contributed to the improvement of the early detection of fatigue cracks in the micro-level size in the beam structures and lug samples.
- The two effects of change in the temperature-dependent material properties of a body as well as the formation of internal thermal stresses were shown to be independent factor in affecting the dynamic behavior of a structure. This was investigated and justified by studying the formulations of Helmholtz free energy and stresses inside a body.
- A new modeling approach was proposed for modeling the presence of a single fatigue crack in an Euler-Bernoulli beam. Rayleigh-Ritz approximation was applied in the proposed approach and was shown to match well with the results of the cracked-beam modeling available in literature for different crack parameters and beam support conditions.
- An analytical model was formulated for the combination of the two effects of damage growth and temperature variations on the vibratory response of an Euler-Bernoulli beam in the presence of a surface-bonded piezoceramic sensing layer. The effect of these modeling parameters were numerically investigated on the mode shape and

natural frequency variations of the vibrating beam as well as the change in the output voltage of the surface-bonded sensor and the time-response of the beam.

- Through the analytical and numerical analysis, it was shown that the effect of temperature-dependent variations in the material properties of the structure will be seen through change in the natural frequency of the structure as well variations in the amplitude of its dynamic response. The formation of thermal stresses inside the structure, however, would only cause variations in the amplitude of the vibrations of the structure.

6.3. Recommendations and Future Work

The analytical model formulated and presented in this work is a start in the fundamental study of the effect of temperature on different SHM-based methodologies. The formulations provided here were focused on the beam structures. In a similar fashion, the analytical study of the effect of temperature and damage growth can be studied for plate structures and other basic mechanical structures.

Having the analytical and numerical analysis of the effect of temperature of provided, the most important future work is to experimentally investigate and verify these results and modify the modeling accordingly.

BIBLIOGRAPHY

- [1] SHM MURI, "<http://murishm.engineering.asu.edu/>" Retrieved March, 2012.
- [2] Piezo Systems, Incorporated, "<http://www.piezo.com/prodsheet1sq5A.html>" Retrieved March, 2012.
- [3] Smart Material, Corporation, "<http://www.smart-material.com/MFC-product-main.html>" Retrieved March, 2012.
- [4] Adams, D., (2002), "Frequency domain ARX model and multi-harmonic FRF estimators for non-linear dynamic systems," *Journal of Sound and Vibration*, **250**(5): 935-950.
- [5] Adams, R., Cawley, P., Pye, C. and Stone, B., (1978), "A vibration technique for non-destructively assessing the integrity of structures," *Journal of Mechanical Engineering Science*, **20**(2): 93-100.
- [6] Adams, R., Cawley, P., Pye, C. and Stone, B., (1978), "A vibration technique for non destructively assessing the integrity of structures," *ARCHIVE: Journal of Mechanical Engineering Science 1959-1982 (vols 1-23)*, **20**(2): 93-100.
- [7] Afshari, M., Butrym, B. and Inman, D., (2009), "On Quantifying Detectable Fatigue Crack Size in Aluminum Beams Using Vibration and Impedance-Based Methods," *ASME 2009 Conference on Smart Materials, Adaptive Structures and Intelligent Systems (SMASIS2009)* Oxnard, California, USA, ASME.
- [8] Afshari, M., Park, S. and Inman, D., (2009), "The Early Stage Crack Detection using Non-Linear Feature Extraction of the Self-Sensing Piezoelectric Impedance Measurements," *Proceedings of the 7th International Workshop on Structural Health Monitoring (IWSHM09)*, Stanford, CA, USA.
- [9] Anton, S.R. and Inman, D.J., (2011), "Electromechanical Modeling of a Multifunctional Energy Harvesting Wing Spar," *Proceedings of the 52nd AIAA/ASME/ASCE/AHS/ASC Structures, Structural Dynamics and Materials Conference*, Denver, CO, USA.
- [10] Aydin, K., (2008), "Vibratory characteristics of Euler-Bernoulli beams with an arbitrary number of cracks subjected to axial load," *Journal of Vibration and Control*, **14**(4): 485.
- [11] Ayres, J., Lalande, F., Chaudhry, Z. and Rogers, C., (1996), "Qualitative health monitoring of a steel bridge joint via piezoelectric actuator/sensor patches," *Proceedings, SPIE Nondestructive Evaluation Techniques for Aging Infrastructure & Manufacturing*, Scottsdale, AZ.
- [12] Balmes, E., Basseville, M., Bourquin, F., Mevel, L., Nasser, H. and Treysse, F., (2008), "Merging sensor data from multiple temperature scenarios for vibration monitoring of civil structures," *Structural Health Monitoring*, **7**(2): 129-142.
- [13] Bardell, N., (1991), "Free vibration analysis of a flat plate using the hierarchical finite element method," *Journal of Sound and Vibration*, **151**(2): 263-289.

- [14] Barrette, M., Berry, A. and Beslin, O., (2000), "Vibration of stiffened plates using hierarchical trigonometric functions," *Journal of Sound and Vibration*, **235**(5): 727-747.
- [15] Batra, R.C., (2006), *Elements of continuum mechanics*, Aiaa.
- [16] Beer, F. and Johnston, E., (2005), *Mechanics of materials*, McGraw-Hill.
- [17] Beslin, O. and Nicolas, J., (1997), "A hierarchical functions set for predicting very high order plate bending modes with any boundary conditions," *Journal of Sound and Vibration*, **202**(5): 633-655.
- [18] Bhalla, S., Naidu, A. and Soh, C., (2003), "Influence of structure-actuator interactions and temperature on piezoelectric mechatronic signatures for NDE," *Proceedings of ISSS-SPIE 2002 International Conference on Smart Materials Structures and Systems*, Bangalore, India
- [19] Bindal, V., (1999), *Transducers for Ultrasonic Flaw Detection*, Narosa Pub House.
- [20] Boley, B. and Weiner, J., (1960), *Theory of thermal stresses*, Hohn Wiley & Sons, Inc.
- [21] Boller, C., (2001), "Ways and options for aircraft structural health management," *Smart Materials and Structures*, **10**: 432.
- [22] Bueckner, H., (1997), "The propagation of cracks and the energy of elastic deformation," *Transactions of the ASME*, **80**: 1225-1229.
- [23] Cawley, P. and Adams, R., (1979), "The location of defects in structures from measurements of natural frequencies," *The Journal of Strain Analysis for Engineering Design*, **14**(2): 49.
- [24] Chang, F.K., (1997), *Proceedings of the 1st International Workshop on Structural Health Monitoring*, Stanford University, Stanford, CA.
- [25] Chang, F.K., (1999), *Proceedings of the 2nd International Workshop on Structural Health Monitoring*, Stanford University, Stanford, CA.
- [26] Chang, H.H.S. and Huang, Z., (2009), "Pyroelectric effect enhancement through product property under open circuit condition," *Journal of Applied Physics*, **106**(1): 014101.
- [27] Chang, W. and Wan, S., (1986), "Thermomechanically coupled non-linear vibration of plates," *International Journal of Non-Linear Mechanics*, **21**(5): 375-389.
- [28] Chatterjee, A., (2010), "Structural damage assessment in a cantilever beam with a breathing crack using higher order frequency response functions," *Journal of Sound and Vibration*, **329**(16): 3325-3334.
- [29] Chondros, T. and Dimarogonas, A., (1998), "Vibration of a cracked cantilever beam," *Journal of vibration and acoustics*, **120**: 742.
- [30] Chondros, T., Dimarogonas, A. and Yao, J., (1998), "A continuous cracked beam vibration theory," *Journal of Sound and Vibration*, **215**(1): 17-34.
- [31] Christides, S. and Barr, A., (1984), "One-dimensional theory of cracked Bernoulli-Euler beams," *International Journal of Mechanical Sciences*, **26**(11-12): 639-648.
- [32] Cordes, R.D. and Joseph, P.F., (1994), "Surface and internal cracks in a residually stressed plate," *International journal of fracture*, **68**(4): 287-314.
- [33] Dang, T.D., Kapania, R.K. and Patil, M.J., (2010), "Analytical modeling of cracked thin-walled beams under torsion," *AIAA journal*, **48**(3): 664-675.

- [34] Dang, T.D., Kapania, R.K. and Patil, M.J., (2011), "Ritz analysis of discontinuous beams using local trigonometric functions," *Computational Mechanics*, **47**(3): 235-250.
- [35] De Vera, C. and Guemes, J., (1998), "Embedded self-sensing piezoelectric for damage detection," *Structural Health Monitoring: Current Status and Perspectives*: 445.
- [36] Delale, F. and Erdogan, F., (1981), "Line-spring model for surface cracks in a Reissner plate," *International Journal of Engineering Science*, **19**(10): 1331-1340.
- [37] Dilena, M. and Morassi, A., (2004), "The use of antiresonances for crack detection in beams," *Journal of Sound and Vibration*, **276**(1-2): 195-214.
- [38] Dimarogonas, A., (1970), "Dynamic response of cracked rotors," *General Electric Co., Internal Report, Schenectady, New York*.
- [39] Dimarogonas, A., (1971), "Dynamics of cracked shafts," *General Electric Co., Internal Report, Schenectady, New York*.
- [40] Dimarogonas, A., (1996), "Vibration of cracked structures: a state of the art review," *Engineering Fracture Mechanics*, **55**(5): 831-857.
- [41] Doebling, S., Farrar, C. and Prime, M., (1998), "A summary review of vibration-based damage identification methods," *Shock and Vibration Digest*, **30**(2): 91-105.
- [42] Entwistle, R. and Stone, B., (1990), "A Survey of the Use of Vibration Methods in the Assessment of Component Geometry," *Australian Vibration and Noise Conference 1990: Vibration and Noise-measurement Prediction and Control*.
- [43] Farrar, C., Cornwell, P., Doebling, S. and Prime, M., (2000), Structural health monitoring studies of the Alamosa Canyon and I-40 Bridges, LA-13635-MS, Los Alamos National Lab., NM (US).
- [44] Faverjon, B. and Sinou, J.J., (2009), "Identification of an open crack in a beam using an a posteriori error estimator of the frequency response functions with noisy measurements," *European Journal of Mechanics-A/Solids*, **28**(1): 75-85.
- [45] Fernandez-Saez, J. and Navarro, C., (2002), "Fundamental frequency of cracked beams in bending vibrations: an analytical approach," *Journal of Sound and Vibration*, **256**(1): 17-31.
- [46] Fernandez-Saez, J., Rubio, L. and Navarro, C., (1999), "Approximate calculation of the fundamental frequency for bending vibrations of cracked beams," *Journal of Sound and Vibration*, **225**(2): 345-352.
- [47] Fink, M., (1997), "Time reversed acoustics," *Physics Today*, **50**: 34.
- [48] Freund, L. and Herrmann, G., (1976), "Dynamic fracture of a beam or plate in plane bending," *Journal of Applied Mechanics*, **43**: 112.
- [49] Giurgiutiu, V. and Cuc, A., (2005), "Embedded non-destructive evaluation for structural health monitoring, damage detection, and failure prevention," *Shock and Vibration Digest*, **37**(2): 83.
- [50] Giurgiutiu, V. and Rogers, C., (1998), "Recent advancements in the electro-mechanical (E/M) impedance method for structural health monitoring and NDE," *Proceedings, SPIE Conference on Smart Structures and Integrated Systems*.
- [51] Hasan, W.M., (1995), "Crack detection from the variation of the eigenfrequencies of a beam on elastic foundation," *Engineering Fracture Mechanics*, **52**(3): 409-421.

- [52] Ihn, J.B. and Chang, F.K., (2004), "Detection and monitoring of hidden fatigue crack growth using a built-in piezoelectric sensor/actuator network: I. Diagnostics," *Smart Materials and Structures*, **13**: 609.
- [53] Ihn, J.B. and Chang, F.K., (2008), "Pitch-catch active sensing methods in structural health monitoring for aircraft structures," *Structural Health Monitoring*, **7**(1): 5-19.
- [54] Inan, E., (1972), "Coupled theory of thermoelastic plates," *Acta Mechanica*, **14**(1): 1-29.
- [55] Irwin, G.R., (1957), "Analysis of stresses and strains near the end of a crack traversing a plate," *Journal of Applied Mechanics*, **24**: 361-364.
- [56] Jones, J., (1966), "Thermoelastic vibrations of a beam," *The Journal of the Acoustical Society of America*, **39**: 542.
- [57] Khadem, S. and Rezaee, M., (2000), "An analytical approach for obtaining the location and depth of an all-over part-through crack on externally in-plane loaded rectangular plate using vibration analysis," *Journal of Sound and Vibration*, **230**(2): 291-308.
- [58] Khadem, S. and Rezaee, M., (2000), "Introduction of modified comparison functions for vibration analysis of a rectangular cracked plate," *Journal of Sound and Vibration*, **236**(2): 245-258.
- [59] Khiem, N. and Lien, T., (2001), "A simplified method for natural frequency analysis of a multiple cracked beam," *Journal of Sound and Vibration*, **245**(4): 737-751.
- [60] Koo, K.Y., Park, S., Lee, J.J. and Yun, C.B., (2009), "Automated impedance-based structural health monitoring incorporating effective frequency shift for compensating temperature effects," *Journal of Intelligent Material Systems and Structures*, **20**(4): 367-377.
- [61] Kumar, Y. and Paik, J.K., (2004), "Buckling analysis of cracked plates using hierarchical trigonometric functions," *Thin-walled structures*, **42**(5): 687-700.
- [62] Lalande, F., Rogers, C., Childs, B. and Chaudhry, Z., (1996), "High-frequency impedance analysis for NDE of complex precision parts," *Proceedings, SPIE Conference on Smart Structures and Materials*, San Diego, CA.
- [63] Lalande, F. and Rogers, C.A., (1996), "Solid-state active sensing for in-situ health monitoring," *Proceedings, Society for Machinery Failure Prevention Technology Showcase*, Mobile, AL.
- [64] Lee, B., Manson, G. and Staszewski, W., (2003), "Environmental effects on Lamb wave responses from piezoceramic sensors," *Materials Science Forum*, **440-441**: 195-202.
- [65] Lee, B. and Staszewski, W., (2003), "Modelling of Lamb waves for damage detection in metallic structures: Part II. Wave interactions with damage," *Smart Materials and Structures*, **12**: 815.
- [66] Lee, U. and Shin, J., (2002), "A structural damage identification method for plate structures," *Engineering Structures*, **24**(9): 1177-1188.
- [67] Leo, D.J., (2007), *Engineering analysis of smart material systems*, Wiley Online Library.
- [68] Li, Q., (2003), "Vibratory characteristics of Timoshenko beams with arbitrary number of cracks," *Journal of engineering mechanics*, **129**(11): 1355-1359.
- [69] Liang, C., Sun, F. and Rogers, C., (1994), "Coupled electro-mechanical analysis of adaptive material systems—determination of the actuator power consumption and system energy transfer," *Journal of Intelligent Material Systems and Structures*, **5**(1): 12-20.

- [70] Liu, Y., Liang, L., Hong, Q. and Antes, H., (1999), "Non-linear surface crack analysis by three dimensional boundary element with mixed boundary conditions," *Engineering Fracture Mechanics*, **63**(4): 413-424.
- [71] Lu, Y. and Michaels, J., (2005), "A methodology for structural health monitoring with diffuse ultrasonic waves in the presence of temperature variations," *Ultrasonics*, **43**(9): 717-731.
- [72] Manoach, E. and Ribeiro, P., (2004), "Coupled, thermoelastic, large amplitude vibrations of Timoshenko beams," *International Journal of Mechanical Sciences*, **46**(11): 1589-1606.
- [73] Maruyama, K. and Ichinomiya, O., (1989), "Experimental study of free vibration of clamped rectangular plates with straight narrow slits," *JSME international journal. Ser. 3, Vibration, control engineering, engineering for industry*, **32**(2): 187-193.
- [74] Meirovitch, L., (1967), "Analytical methods in vibration," *Macmillan Company London*.
- [75] Morassi, A., (1993), "Crack-Induced Changes in Eigenparameters of Beam Structures," *Journal of Engineering Mechanics*, **119**: 1798-1803.
- [76] Narkis, Y., (1994), "Identification of crack location in vibrating simply supported beams," *Journal of Sound and Vibration*, **172**(4): 549-558.
- [77] Nowacki, W., (1986), *Thermoelasticity*, Pergamon Press Ltd.
- [78] Ostachowicz, W. and Krawczuk, M., (1991), "Analysis of the effect of cracks on the natural frequencies of a cantilever beam," *Journal of Sound and Vibration*, **150**(2): 191-201.
- [79] Park, G., Cudney, H. and Inman, D., (2000), "Impedance-based health monitoring of civil structural components," *Journal of infrastructure systems*, **6**(4): 153-160.
- [80] Park, G., Farrar, C.R., Rutherford, A.C. and Robertson, A.N., (2006), "Piezoelectric active sensor self-diagnostics using electrical admittance measurements," *Journal of vibration and acoustics*, **128**: 469.
- [81] Park, G., Kabeya, K., Cudney, H.H. and Inman, D.J., (1999), "Impedance-based structural health monitoring for temperature varying applications," *JSME international journal. Series A, Solid mechanics and material engineering*, **42**(2): 249-258.
- [82] Park, G., Sohn, H., Farrar, C. and Inman, D., (2003), "Overview of piezoelectric impedance-based health monitoring and path forward," *Shock and Vibration Digest*, **35**(6): 451-464.
- [83] Peairs, D., Park, G. and Inman, D., (2004), "Improving accessibility of the impedance-based structural health monitoring method," *Journal of Intelligent Material Systems and Structures*, **15**(2): 129.
- [84] Peeters, B. and De Roeck, G., (2001), "One-year monitoring of the Z24-Bridge: environmental effects versus damage events," *Earthquake Engineering & Structural Dynamics*, **30**(2): 149-171.
- [85] Prasad, R., Roy, S. and Tyagi, K., (2010), "Effect of Crack Position along Vibrating Cantilever Beam on Crack Growth Rate," *work*, **2**(5): 837-839.
- [86] Raghavan, A. and Cesnik, C.E.S., (2007), "Review of guided-wave structural health monitoring," *Shock and Vibration Digest*, **39**(2): 91-116.
- [87] Raghavan, A. and Cesnik, C.E.S., (2008), "Effects of elevated temperature on guided-wave structural health monitoring," *Journal of Intelligent Material Systems and Structures*, **19**(12): 1383-1398.

- [88] RAIB, (2008), "Derailment at Grayrigg, Cumbria 23 February 2007," *Report 20/2008, Department of Transport, UK.*
- [89] Raju, V., (1997), Implementing impedance-based health monitoring.
- [90] Rao, S., (2007), *Vibration of continuous systems*, John Wiley & Sons Inc.
- [91] Rezaee, M. and Hassannejad, R., (2011), "A new approach to free vibration analysis of a beam with a breathing crack based on mechanical energy balance method," *Acta Mechanica Solida Sinica*, **24**(2): 185-194.
- [92] Rice, J. and Levy, N., (1972), "The part-through surface crack in an elastic plate," *Journal of Applied Mechanics*, **39**: 185.
- [93] Rogers, C. and Lalande, F., (1996), Solid-state active sensing for in-situ health monitoring, Proceedings, Society for Machinery Failure Prevention Technology Showcase, Mobile, AL.
- [94] Rubio, L. and Fernández-Sáez, J., (2010), "A Note on the Use of Approximate Solutions for the Bending Vibrations of Simply Supported Cracked Beams," *Journal of vibration and acoustics*, **132**: 024504.
- [95] Salawu, O., (1997), "Detection of structural damage through changes in frequency: a review," *Engineering Structures*, **19**(9): 718-723.
- [96] Schmerling, J. and Hammon, J., (1976), "Investigation of the Tennessee Valley Authority Gallatin Unit No. 2 Turbine Rotor Burst," *American Power Conference*, Chicago.
- [97] Schulz, M.J., Sundaresan, M.J., McMichael, J., Clayton, D., Sadler, R. and Nagel, B., (2003), "Piezoelectric materials at elevated temperature," *Journal of Intelligent Material Systems and Structures*, **14**(11): 693-705.
- [98] Shigley, J., Mischke, C., Budynas, R., Liu, X. and Gao, Z., (2004), *Mechanical engineering design*, McGraw-Hill New York.
- [99] Sohn, H., Dzwonczyk, M., Straser, E., Kiremidjian, A., Law, K. and Meng, T., (1999), "An experimental study of temperature effect on modal parameters of the Alamosa Canyon Bridge," *Earthquake Engineering & Structural Dynamics*, **28**(8): 879-897.
- [100] Stahl, B. and Keer, L., (1972), "Vibration and stability of cracked rectangular plates," *International Journal of Solids and Structures*, **8**(1): 69-91.
- [101] Sun, F., Chaudhry, Z., Liang, C. and Rogers, C., (1995), "Truss structure integrity identification using PZT sensor-actuator," *Journal of Intelligent Material Systems and Structures*, **6**(1): 134-139.
- [102] Sutton, P., (1953), "The variation of the elastic constants of crystalline aluminum with temperature between 63 k and 773 k," *Physical Review*, **91**(4): 816-821.
- [103] Tada, H., Paris, P. and Irwin, G., (2000), *The stress analysis of cracks handbook*, ASME Press: Professional Engineering Pub.: ASM International.
- [104] Tseng, K. and Naidu, A., (2002), "Non-parametric damage detection and characterization using smart piezoceramic material," *Smart Materials and Structures*, **11**: 317.
- [105] Turner, R., Fuierer, P., Newnham, R. and Shrout, T., (1994), "Materials for high temperature acoustic and vibration sensors: A review," *Applied acoustics*, **41**(4): 299-324.

- [106] Tzou, H. and Howard, R., (1994), "A piezothermoelastic thin shell theory applied to active structures," *Transactions of the ASME Journal of Vibration and Acoustics*, **116**: 295-295.
- [107] Tzou, H. and Ye, R., (1994), "Piezothermoelasticity and precision control of piezoelectric systems: theory and finite element analysis," *Journal of vibration and acoustics*, **116**: 489.
- [108] Wang, C.H., Rose, J.T. and Chang, F.K., (2004), "A synthetic time-reversal imaging method for structural health monitoring," *Smart Materials and Structures*, **13**: 415.
- [109] Wauer, J., (1990), "Cracked rotor dynamics: a state of the art survey," *Applied Mechanics Reviews*, **43**(1): 13-17.
- [110] Wen, Y.S. and Jin, Z., (1987), "On the equivalent relation of the line spring model: A suggested modification," *Engineering Fracture Mechanics*, **26**(1): 75-82.
- [111] Woon, C. and Mitchell, L., (1996), "Temperature-induced variations in structural dynamic characteristics part I: experimental," *SPIE*.
- [112] Woon, C. and Mitchell, L., (1996), "Temperature-induced variations in structural dynamic characteristics part II: analytical."
- [113] Yin, S.S. and Ruffin, P., (2002), *Fiber optic sensors*, Wiley Online Library.
- [114] Yuan, J. and Dickinson, S., (1992), "The flexural vibration of rectangular plate systems approached by using artificial springs in the Rayleigh-Ritz method," *Journal of Sound and Vibration*, **159**(1): 39-55.
- [115] Zeng, Z.J., Dai, S.H. and Yang, Y.M., (1993), "Analysis of surface cracks using the line-spring boundary element method and the virtual crack extension technique," *International journal of fracture*, **60**(2): 157-167.

APPENDIX A

DESIGN DETAILS OF THE FULL SCALE PROTOTYPE OF A SWITCH TRACK

The full scale prototype is composed of two switch blades, a lock rod and two switch rods. Dimensions and description of these parts and the assembly components are as follows:

- 2 Structural angles 5"× 3"× ½", 5' long
- 4 Structural angles 6"× 4"× 1", 7" long
- 2 Angle bars 1' 3"× 4"× 1", 3" long
- 3 Rectangular bars 2 ½"× 1 ¼", 2' long
- 1 Rectangular bars 2 ½"× 1 ¼", 3' long
- 2 Rectangular bars 2 ½"× 1", 1' 10 ¾" long
- 6 Rectangular bars 2 ½"× ½", 9 ½" long
- 2 Sheets 7"× 2"× 1/8"

Bolts:

- 5/8-11×3 Structural Bolts A325
- 5/8-11×4 1/2 Structural Bolts A325
- 7/8-9×2 Structural Bolts A325
- 1-8×4 Structural Bolts A325

Nuts:

- 5/8-11 2H Heavy Hex Nuts A194
- 7/8-9 Thread2H Heavy Hex Nuts A194
- 1-8 2H Heavy Hex Nuts A194

Washers:

- ¾ Med L/W Plain Domestic R36 Washers
- 1 Med L/W Plain Domestic R36 Washers

The two parts of the switch rods were insulated using the fiberglass Insulation Paper, 1/8" thick, 16" width and 10' length.